International Journal of Antennas and Propagation

Advanced Antenna Technologies in the Beyond IMT-Advanced Systems

Guest Editors: Mugen Peng, Cheng-Xiang Wang, Feifei Gao, and Wei Xiang

Advanced Antenna Technologies in the Beyond IMT-Advanced Systems

International Journal of Antennas and Propagation

Advanced Antenna Technologies in the Beyond IMT-Advanced Systems

Guest Editors: Mugen Peng, Cheng-Xiang Wang, Feifei Gao, and Wei Xiang

Editorial Board

Contents

Hindawi Publishing Corporation
International Journal of Antennas and Propagation
Volume 2013, Article ID 156831, 2 pages
http://dx.doi.org/10.1155/2013/156831

Editorial

Advanced Antenna Technologies in the Beyond IMT-Advanced Systems

Mugen Peng,[1] Cheng-Xiang Wang,[2] Feifei Gao,[3] and Wei Xiang[4]

[1] *The Key Laboratory of Universal Wireless Communications for the Ministry of Education, Beijing University of Posts and Telecommunications, Beijing 100876, China*
[2] *School of Engineering & Physical Sciences, Heriot-Watt University, Edinburgh EH14 4AS, UK*
[3] *Department of Automation, Tsinghua University, Beijing 100084, China*
[4] *School of Mechanical and Electrical Engineering, University of Southern Queensland (USQ), Toowoomba, QLD 4350, Australia*

Correspondence should be addressed to Mugen Peng; pmg@bupt.edu.cn

Received 2 October 2013; Accepted 2 October 2013

Both the fourth generation (4G) and fifth generation (5G) mobile systems will use multiple-input multiple-output (MIMO) technologies with multiantenna capabilities at both the base station and user equipment. To improve the capacity, extend the coverage, and decrease the antenna deployment complexity, many advanced antenna technologies have been proposed recently, such as the large-scale array antenna and the small-scale smart antenna. The large-scale array antenna system, also known as massive MIMO or massive three-dimension (3D) antenna, is a new research field in antenna systems, electronics, communication theory, and embedded software. It is often utilized in the frequency division duplex- (FDD-) based 4G & 5G systems, and its performance gain over the classical array antenna, which uses a relatively small number of antennas fed via coaxial cables from a high-power amplifier, is thus significant. However, one of the disadvantages of massive MIMO systems is that the antenna size is too large, resulting in a large frontal area. Meanwhile, the miniaturization of smart antenna (also known as the small-scale smart antenna) is often designed for the time division duplex (TDD) 4G & 5G systems and can effectively decrease the antenna size, while ensuring the capacity and coverage performances.

To fully realize the potential of advanced antenna technologies and to solve the problems of antenna application, this special issue aims to attract the attention of the research community for developing advanced and innovative antenna-related methodologies and techniques. We have received a total of 18 original submissions, out of which 8 papers were accepted for publication after peer reviewing. We regret that we had to reject many good papers due to the limited number of papers that can be published within this special issue. The accepted papers cover a broad area of advanced antenna topics.

Propagation and antenna models are indispensable for investigating advanced antenna techniques. A paper entitled "*Full-wave analysis of microstrip antennas in a three-layered spherical media*" by C. Yin et al. proposes an antenna model and the dyadic Green's function in spherical microstrip antennas. Furthermore, the asymptotic extraction approach is presented to accelerate the Green's functions convergence speed when source and field points locate in the same layer and different layers.

In a paper entitled "*Dynamic beamforming for three dimensional MIMO technique in LTE-advanced networks*" by Y. Li et al. the authors present a dynamic beamforming algorithm where vertical domain of antenna is fully considered and beamforming vector can be obtained according to UEs' horizontal and vertical directions. At most 34% gain for cell center UE and 92% gain for cell edge UE over the conventional 2D beamforming algorithm are achieved by the proposed algorithm. Another paper entitled "*Limited feedback precoding for massive MIMO*" by X. Su et al. proposes an avenue of codebook design based on a Kronecker-type approximation of the array correlation structure for the uniform rectangular antenna array. Simulation results

demonstrate that the proposed codebook outperforms the exisiting codebooks remarkably.

A paper entitled "*The study of indoor and field trials on 2 × 8 MIMO architecture in TD-LTE network*" by X. Zhang et al. analyzes measurement methods of four MIMO transmission modes (TMs) in time division-LTE (TD-LTE), where indoor and field tests are presented to investigate how real-world propagation affects the capacity and the error performance of MIMO transmission scheme. In the fifth paper entitled "*Energy efficiency maximization through cooperative transmit and receive antenna selection for multi-cell MU-MIMO system*" by Y. Dong et al., an antenna selection scheme which can maximize the energy efficiency of BS cluster is proposed, and a cost function varying with the number of antennas is presented. Also, the effect of the antenna selection scheme on the energy efficiency of both the serving BS and the neighbor BS is investigated.

For the advanced relevant wireless communication techniques, a paper entitled "*Interference coordination in multiple antenna based LTE-advanced heterogeneous systems*" by Y. Li et al. presents two interference coordination (IC) schemes based on whether the receiver coding matrix is full rank or not, named as full coding (IC-FC) and part coding (IC-PC), respectively. A paper entitled "*Power scaling for spatial modulation with limited feedback*" by Y. Xiao proposes the power scaling spatial modulation (PS-SM) scheme. The main idea is based on the introduction of a scaling factor (SF) for weighting the modulated symbols on each transmit antenna of SM, so as to enlarge the minimum Euclidean distance of modulated constellations and improve the system performance. In another paper entitled "*Secrecy balancing over two-user MISO interference channels with rician fading*" by J. Ni considers a 2-user multiple-input single-output (MISO) interference channel with confidential messages (IFC-CM) in which a quadratic relationship between the real-valued parameters of two users are derived for the Rician channel to reach the ergodic secrecy rate balancing point.

Acknowledgment

Before the end of this editorial, the authors would like to thank the anonymous reviewers for their great efforts in reviewing the submitted papers, without which this special issue would not have been published as scheduled.

Mugen Peng
Cheng-Xiang Wang
Feifei Gao
Wei Xiang

Hindawi Publishing Corporation
International Journal of Antennas and Propagation
Volume 2013, Article ID 416352, 9 pages
http://dx.doi.org/10.1155/2013/416352

Research Article

Limited Feedback Precoding for Massive MIMO

Xin Su, Jie Zeng, Jingyu Li, Liping Rong, Lili Liu, Xibin Xu, and Jing Wang

Tsinghua National Laboratory for Information Science and Technology, Tsinghua University, Beijing 100084, China

Correspondence should be addressed to Jie Zeng; zengjie@tsinghua.edu.cn

Received 11 January 2013; Revised 18 July 2013; Accepted 7 August 2013

Academic Editor: Wei Xiang

The large-scale array antenna system with numerous low-power antennas deployed at the base station, also known as massive multiple-input multiple-output (MIMO), can provide a plethora of advantages over the classical array antenna system. Precoding is important to exploit massive MIMO performance, and codebook design is crucial due to the limited feedback channel. In this paper, we propose a new avenue of codebook design based on a Kronecker-type approximation of the array correlation structure for the uniform rectangular antenna array, which is preferable for the antenna deployment of massive MIMO. Although the feedback overhead is quite limited, the codebook design can provide an effective solution to support multiple users in different scenarios. Simulation results demonstrate that our proposed codebook outperforms the previously known codebooks remarkably.

1. Introduction

High-rate data demand increases faster and faster with the new generation of devices (smart phones, tablets, netbooks, etc.). However, the huge increase in demand can be hardly met by current wireless systems. As is known to us, MIMO channels, created by deploying antenna arrays at the transmitter and receiver, promise high-capacity and high-quality wireless communication links by spatial multiplexing and diversity. Basically, the more antennas the transmitter or the receiver equipped with, the more degrees of freedom that the propagation channel can provide, and the higher data rate the system can offer. Therefore, there is significant effort within the community to research and develop massive MIMO technology, which is a hot topic nowadays [1].

For multiuser MIMO systems, we can utilize precoding to explore massive MIMO potentials. The essence of precoding techniques is to mitigate the interuser interference and to improve the effective received SNR. Herein, channel state information at the transmitter (CSIT) is an essential component when trying to maximize massive MIMO performance via precoding. In time division duplexing (TDD) system, channel reciprocity can be utilized for pilot training in the uplink to acquire the complete CSIT, but the pilot contamination and imperfect channel estimation based on uplink pilots would lead to inaccuracy of the CSIT. In frequency division duplexing (FDD) system, the CSIT shall be acquired via the feedback channel, which is usually limited in practice. Hence, a finite set of precoding matrices, named codebook, known to both the receiver and the transmitter should be predesigned. The receiver selects the optimal precoding matrix from the codebook according to the channel state information (CSI) and reports the precoding matrix indicator (PMI) to the transmitter via the limited feedback channel [2]. With this mechanism, the system can obtain performance improvement by employing a well-designed codebook.

For traditional MIMO systems, several codebooks have been proposed, such as Kerdock codebook [3], codebooks based on vector quantization [4], Grassmannian packing [5], discrete Fourier transform (DFT) [6], and quadrature amplitude modulation [7]. Codebooks based on vector quantization have taken the channel distribution into account but have to be redesigned when the channel distribution changes. For uncorrelated channels, the Grassmannian is nearly the optimal codebook, but its construction requires numerical iterations, and with high storage requirement. The Kerdock codebook has simple systematic construction, significantly low storage, and selection computational requirements due to finite quaternary alphabet. However, the Grassmannian codebook and the Kerdock codebook are not optimized for

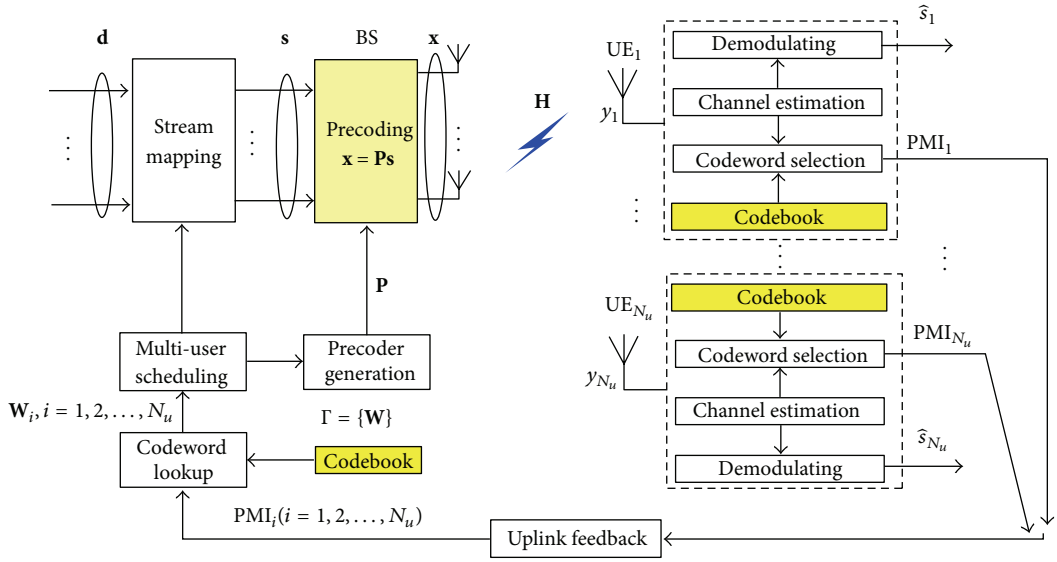

Figure 1: The feedback precoding model of the multiuser MIMO system.

correlated channels when closely spaced ($\lambda/2$) antenna arrays are employed. This case with the substantial correlation can be better reflected by DFT codebooks.

Traditionally, the uniform linear array (ULA) setup is adopted in a MIMO system. But for the consideration of constrained array aperture and aesthetic factor, the ULA setup is not suitable for massive MIMO. Besides, the linear array with antenna elements of identical gain patterns (e.g., isotropic elements) brings the problem of front-back ambiguity and is also unable to resolve signal paths in both azimuth and elevation [8]. For these reasons, the massive MIMO might employ two-dimensional array structures, such as the uniform rectangular array (URA). However, the current proposals of DFT codebooks fail to work well on the new antenna layout, since the codebook construction is aimed at the linear arrays, such as ULA. Thus, we need a new scheme to construct the codebook to better reflect the channel properties.

The rest of the paper is outlined as follows. In Section 2, we introduce the system model. In Section 3, we present the codebook designs including the novel codebook design for URA purpose. Then, we analyze the channel capacity and evaluate the performance of different codebooks in Section 4. Finally, we give some conclusions in Section 5.

2. System Model

In this paper, we focus on the downlink transmission of a massive MIMO system, that is, the base station (BS) with massive antennas as the transmitter and the user equipment (UE) as the receiver, and we adopt the multiuser MIMO transmission architecture with feedback precoding mechanism, as shown in Figure 1. The BS is equipped with N_t transmit antennas, and N_u UEs with N_r receive antennas, each is served by the BS in the cell; and the maximum number of spatial multiplexing UEs is K. In this paper, we assume that $N_r = 1$, $N_t \gg K$, and $K \geq 1$.

In order to report the CSI from the receiver to the transmitter via a limited feedback channel, we need to predesign a codebook. Given the codebook containing a list of codewords $\mathbf{W}_i$ at both the transmitter side and the receiver side, each of which reflects one state of the channel at a certain time, the receiver can only report an index within the codebook, called PMI, to the transmitter; then the transmitter obtains the PMI and queries the codebook to accomplish the precoding process.

For the codeword selection at the receiver, we can adopt the capacity selection criterion [5] which is to maximize the channel gain given the channel matrix $\widehat{\mathbf{H}}$ by traversing the whole codebook Γ:

$$\mathbf{W}_k^{\mathrm{opt}} = \mathbf{W}^{\Gamma}\left(\widehat{\mathbf{H}}_k\right) = \max_{\mathbf{W}\in\Gamma} \left\|\mathbf{W}\widehat{\mathbf{H}}_k\right\|_2^2. \tag{1}$$

For a multiuser MIMO system, we need to select K UEs to serve simultaneously from a larger number of UEs. Thus, a scheduling module is necessary to select proper UEs. All UEs shall report their own requested codewords $\mathbf{W}_i$; and then we can find out the UE set to schedule according to certain scheduling criteria. After determining the scheduled UEs, the transmitter starts the following data transmission procedure: firstly, multiplexing streams denoted by the vector $\mathbf{s}$ are selected from the user data stream $\mathbf{d}$ inputting in the system according to the multiuser scheduling module; secondly, the data is preprocessed by a precoder $\mathbf{P}$ which is formed by combining the UEs' requested codewords column by column, and we get the transmit signal $\mathbf{x}$:

$$\mathbf{x} = \mathbf{P}\mathbf{s}, \tag{2}$$

where $\mathbf{s} = [s_1, s_2, \ldots, s_K]$, $\mathbf{P} = [\mathbf{W}_{s(1)}, \mathbf{W}_{s(2)}, \ldots, \mathbf{W}_{s(K)}]$, and $\mathbf{W}_{s(i)}$ denotes the codeword for scheduled UE $s(i)$. For the sake of clarity without misunderstanding, we use $\mathbf{W}_i$ instead of $\mathbf{W}_{s(i)}$ in the following expressions.

After $\mathbf{x}$ passing the channel and being added the noise, we will get the received signal $\mathbf{y}$:

$$\mathbf{y} = \mathbf{H}\mathbf{x} + \mathbf{z} = \mathbf{H}\mathbf{P}\mathbf{s} + \mathbf{z}, \tag{3}$$

where $\mathbf{H}$ denotes the channel matrix of size $(K \times N_t)$ with its entry H_{ij} denoting the complex channel response from the jth transmit antenna to the ith UE's receive antenna, and $\mathbf{z}$ is the additive white complex Gaussian noise (AWGN) vector with covariance matrix $\sigma^2\mathbf{I}_K$. For UE k, the received signal y_k is

$$\begin{aligned} y_k &= \mathbf{H}_k\mathbf{x}_k + \sum_{i \neq k} \mathbf{H}_k\mathbf{x}_i + z_k, \\ &= \mathbf{H}_k\mathbf{W}_k s_k + \sum_{i \neq k} \mathbf{H}_k\mathbf{W}_i s_i + z_k. \end{aligned} \tag{4}$$

After UE k obtains the estimated channel matrix $\widehat{\mathbf{H}}_k$ through the channel estimation, it demodulates the received signal y_k:

$$\widehat{s}_k = d_k y_k. \tag{5}$$

If the interference is unaware to the receiver, which means that it is treated as part of the noise, the matched filter (MF) is usually adopted:

$$d_k = \left(\widehat{\mathbf{H}}_k\mathbf{W}_k\right)^*. \tag{6}$$

3. Codebook Design

The codebook design is a quantization problem, in which we should balance the accuracy and the overhead of bits. The Grassmannian codebook would offer the optimal solution for fully uncorrelated channels [5], but it is not practical for massive MIMO systems due to its difficulty of construction for higher-dimensional space. Kerdock can be easily extended to massive transmit antennas due to its systematic construction and low codeword selection complexity. However, like the Grassmannian codebook, the Kerdock codebook is only suitable for uncorrelated channels. For high-correlated channels, a DFT codebook able to respond the channel correlation provides a good fit. Since the channels are likely to be highly correlated due to the closely spaced arrays probably utilized by massive MIMO, we focus on the DFT codebook and its extension for massive MIMO with the URA deployment.

3.1. The Traditional DFT Codebook. Closely spaced arrays, including both crosspolarized and copolarized ones, imply certain spatial correlation structures which may be utilized to compress the channel into an effective channel of lower dimensionality. With such setup, the channel is spatially correlated, and the spatial covariance matrix can be approximated using its eigenvectors with the closely spaced $(\lambda/2)$ array. The linear DFT codebook design targets at the linear closely spaced array, which has two separate parts representing long-term and short-term channel states, respectively [6, 9]. The first codeword $\mathbf{W}^1$ in the long-term feedback part consists of multiple beams such that the beams cover the full signal space over the wideband with closely-spaced arrays, hence capturing the correlation properties of the channel. The second codeword $\mathbf{W}^2$ in the short-term feedback part combines the beams to capture short-term variations. The final precoder $\mathbf{W}$ is given by

$$\mathbf{W} = \mathbf{W}^1\mathbf{W}^2. \tag{7}$$

This is the DFT codebook design for the ULA [10]. It is noted that the design essentially comes from the concept of the adaptive codebook [11]. Under the assumption that the channel correlation is both known by the transmitter with multiple antennas and the receiver with single antenna, the precoder can be computed by

$$\mathbf{W} = \mathbf{R}^{1/2}\mathbf{V}, \tag{8}$$

where $\mathbf{R}$ is the spatial covariance matrix of the channel $\mathbf{H}$, that is, $\mathbf{R} = E[\mathbf{H}^H\mathbf{H}]$, and $\mathbf{V}$ is a $N_t \times 1$ codeword of a uniform codebook. Adaptive codebook is well known to provide good performance in correlated channels, especially for multiuser MIMO. In practical application, a double codebook is utilized to minimize the feedback overhead. The transmitter and the receiver could share the knowledge of the matrix $\mathbf{R}$ through the feedback of first codeword $\mathbf{W}^1$. This feedback overhead is low even though the information of $\mathbf{R}$ is vast, since the feedback interval could be very long due to the stable channel correlation. Besides, the second codeword $\mathbf{W}^2 = \mathbf{V}$ is reported more frequently to represent the short-term variations. The precoder $\mathbf{W} = \mathbf{W}^1\mathbf{W}^2$ can adapt to the angular spread of the channel by covering the instantaneous subspace over the entire band.

For the copolarized arrays of closely spaced $(\lambda/2)$ antenna elements, the codeword $\mathbf{W}^1$ in the long-term feedback codebook is expressed as

$$\mathbf{W}^1(g) = \mathbf{D}(g), \tag{9}$$

where $\mathbf{D}(g)$ $(g = 0, 1, \ldots, G-1)$ are DFT rotation matrices with the size $N \times M$, G is the total number of DFT matrices, and each element can be expressed as

$$[\mathbf{D}(g)]_{n,m} = \frac{1}{\sqrt{N}} \exp\left(j\frac{2\pi}{M}n\left(m + \frac{g}{G}\right)\right), \tag{10}$$

where $n = 0, 1, \ldots, N-1$ and $m = 0, 1, \ldots, M-1$. Here, we have $N = N_t$ and $G = 2^B/M$, where B is the codebook size, that is, the feedback overhead (in bits).

While the first codeword $\mathbf{W}^1$ describes the correlation property of the channel, the second codeword $\mathbf{W}^2$ consists of beam selection vectors. Since the size and the energy of the UEs are usually limited, frequently only one antenna is employed in practical. As a result, rank-1 channels are essential for current multiuser MIMO. For the rank-1 channel, it has the form

$$\mathbf{W}^2(i_2) = \boldsymbol{\nu}_{i_2}, \tag{11}$$

where $\boldsymbol{\nu}_k$ is a $M \times 1$ selection vector that has 1 on the kth row and 0 elsewhere and i_2 indicates the index of $\mathbf{W}^2$ in the second part of the codebook.

Above are the constructions for the linear closely spaced antenna elements. Under such scenarios with the substantially correlated channels, the DFT-based codebook is able to respond the correlation. However, for two-dimensional antenna arrays, the long-term statistical properties of the channel cannot be directly reflected by DFT vectors, since every DFT vector can only represent the beams emitted by the linear closely spaced antenna elements. Hence, we need to extend the DFT codebook to adapt to two-dimensional array structures, like the URA.

3.2. The Proposed Codebook

3.2.1. Kronecker-Type Approximation of Correlation. In this paper, we consider a URA lying on the XY plane with x-axis parallel to one edge of the URA and y-axis parallel to the other vertical edge, as shown in Figure 2 taking 64 copolarized antennas as an example.

We assume that the correlation between the antenna elements along x does not depend on the antenna elements along y and its correlation matrix is described as matrix $\mathbf{R}_x$; the correlation along y does not depend on the antenna elements along x and its correlation matrix is described as matrix $\mathbf{R}_y$. Thus, we have the following Kronecker-type approximation for the URA correlation matrix [12]:

$$\mathbf{R} = \mathbf{R}_x \otimes \mathbf{R}_y, \tag{12}$$

where $\otimes$ denotes the Kronecker product.

Formula (12) indicates that the URA correlation matrix $\mathbf{R}$ is the Kronecker product of two ULA correlation matrices $\mathbf{R}_x$ and $\mathbf{R}_y$. This approximation model is reasonably accurate, allowing the well-developed theory of Toeplitz matrices for the analysis of multidimensional antenna arrays. In the following, we take the Kronecker-type approximation model as the theoretical basis of the first codeword construction.

3.2.2. Codebook Construction

Theorem 1. *If* $\mathbf{X}$ *and* $\mathbf{Y}$ *are diagonalizable square matrices, then*

$$(\mathbf{X} \otimes \mathbf{Y})^{1/2} = \mathbf{X}^{1/2} \otimes \mathbf{Y}^{1/2}. \tag{13}$$

Proof. Firstly, we prove that $(\mathbf{D}_x \otimes \mathbf{D}_y)^{1/2} = \mathbf{D}_x^{1/2} \otimes \mathbf{D}_y^{1/2}$ for diagonal matrices $\mathbf{D}_x$ and $\mathbf{D}_y$.

Suppose that $\mathbf{D}_x = \operatorname{diag}(\lambda_1, \lambda_2, \ldots, \lambda_n)$, $\mathbf{D}_y = \operatorname{diag}(\mu_1, \mu_2, \ldots, \mu_n)$, then

$$\begin{aligned}
&\mathbf{D}_x^{1/2} \otimes \mathbf{D}_y^{1/2} \\
&\quad = \operatorname{diag}\left(\lambda_1^{1/2}, \lambda_2^{1/2}, \ldots, \lambda_n^{1/2}\right) \\
&\qquad \otimes \operatorname{diag}\left(\mu_1^{1/2}, \mu_2^{1/2}, \ldots, \mu_n^{1/2}\right) \\
&\quad = \operatorname{diag}\Big(\left(\lambda_1\mu_1\right)^{1/2}, \left(\lambda_2\mu_1\right)^{1/2}, \ldots, \left(\lambda_n\mu_1\right)^{1/2}, \\
&\qquad \left(\lambda_1\mu_2\right)^{1/2}, \ldots, \left(\lambda_n\mu_2\right)^{1/2}, \ldots, \left(\lambda_n\mu_n\right)^{1/2}\Big) \\
&\quad = \big(\operatorname{diag}\left(\lambda_1\mu_1, \lambda_2\mu_1, \ldots, \lambda_n\mu_1, \lambda_1\mu_2,\right. \\
&\qquad \left.\lambda_2\mu_2, \ldots, \lambda_n\mu_2, \ldots, \lambda_n\mu_n\right)\big)^{1/2} \\
&\quad = \left(\mathbf{D}_x \otimes \mathbf{D}_y\right)^{1/2}.
\end{aligned} \tag{14}$$

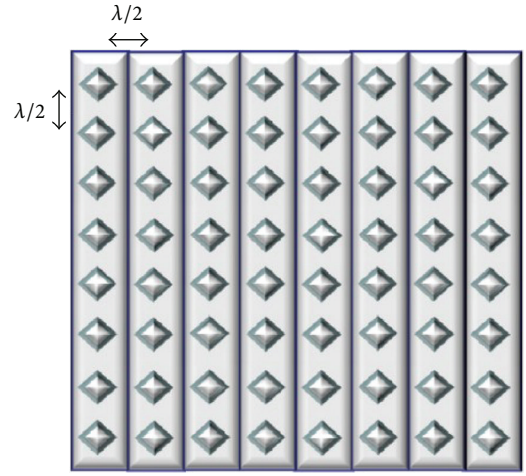

Figure 2: An example of the URA deployment for 64 antennas.

An $n \times n$ matrix $\mathbf{A}$ is diagonalizable if there is a matrix $\mathbf{V}$ and a diagonal matrix $\mathbf{D}$ such that $\mathbf{A} = \mathbf{V}\mathbf{D}\mathbf{V}^{-1}$. In this case, the square root of $\mathbf{A}$ is $\mathbf{R} = \mathbf{V}\mathbf{D}^{1/2}\mathbf{V}^{-1}$. With this rule, we can prove the equation for any diagonalizable square matrices $\mathbf{X}$ and $\mathbf{Y}$.

Suppose $\mathbf{X} = \mathbf{V}_x\mathbf{D}_x\mathbf{V}_x^{-1}$ and $\mathbf{Y} = \mathbf{V}_y\mathbf{D}_y\mathbf{V}_y^{-1}$, then

$$\begin{aligned}
\mathbf{X}^{1/2} \otimes \mathbf{Y}^{1/2} &= \left(\mathbf{V}_x\mathbf{D}_x^{1/2}\mathbf{V}_x^{-1}\right) \otimes \left(\mathbf{V}_y\mathbf{D}_y^{1/2}\mathbf{V}_y^{-1}\right) \\
&= \left(\mathbf{V}_x \otimes \mathbf{V}_y\right)\left(\mathbf{D}_x^{1/2} \otimes \mathbf{D}_y^{1/2}\right)\left(\mathbf{V}_x^{-1} \otimes \mathbf{V}_y^{-1}\right) \\
&= \left(\mathbf{V}_x \otimes \mathbf{V}_y\right)\left(\mathbf{D}_x^{1/2} \otimes \mathbf{D}_y^{1/2}\right)\left(\mathbf{V}_x \otimes \mathbf{V}_y\right)^{-1},
\end{aligned} \tag{15}$$

$$\begin{aligned}
\mathbf{X} \otimes \mathbf{Y} &= \left(\mathbf{V}_x\mathbf{D}_x\mathbf{V}_x^{-1}\right) \otimes \left(\mathbf{V}_y\mathbf{D}_y\mathbf{V}_y^{-1}\right) \\
&= \left(\mathbf{V}_x \otimes \mathbf{V}_y\right)\left(\mathbf{D}_x \otimes \mathbf{D}_y\right)\left(\mathbf{V}_x^{-1} \otimes \mathbf{V}_y^{-1}\right) \\
&= \left(\mathbf{V}_x \otimes \mathbf{V}_y\right)\left(\mathbf{D}_x \otimes \mathbf{D}_y\right)\left(\mathbf{V}_x \otimes \mathbf{V}_y\right)^{-1},
\end{aligned} \tag{16}$$

$$\begin{aligned}
(\mathbf{X} \otimes \mathbf{Y})^{1/2} &= \left(\mathbf{V}_x \otimes \mathbf{V}_y\right)\left(\mathbf{D}_x \otimes \mathbf{D}_y\right)^{1/2}\left(\mathbf{V}_x \otimes \mathbf{V}_y\right)^{-1} \\
&= \left(\mathbf{V}_x \otimes \mathbf{V}_y\right)\left(\mathbf{D}_x^{1/2} \otimes \mathbf{D}_y^{1/2}\right)\left(\mathbf{V}_x \otimes \mathbf{V}_y\right)^{-1}.
\end{aligned} \tag{17}$$

The formulae (15) and (16) utilize the Kronecker product properties including mixed-product property and the inverse property [13].

Thus, $(\mathbf{X} \otimes \mathbf{Y})^{1/2} = \mathbf{X}^{1/2} \otimes \mathbf{Y}^{1/2}$. □

Since first codeword $\mathbf{W}^1$ reflects the channel correlation, we shall design it to satisfy

$$\mathbf{W}^1 = \mathbf{R}^{1/2}. \tag{18}$$

With formula (12) and Theorem 1, we have

$$\mathbf{W}^1 = \mathbf{R}^{1/2} = \left(\mathbf{R}_x \otimes \mathbf{R}_y\right)^{1/2} = \mathbf{R}_x^{1/2} \otimes \mathbf{R}_y^{1/2}. \quad (19)$$

Hence, assuming $\mathbf{D}_x(g_x)$ and $\mathbf{D}_y(g_y)$ are two DFT rotation matrices designed for two orthogonal ULAs, we can construct $\mathbf{W}^1$ for the URA with the Kronecker product of the two matrices:

$$\begin{aligned} \mathbf{W}^1(i_1) &= \mathbf{D}_x(g_x) \otimes \mathbf{D}_y(g_y), \\ \left[\mathbf{D}_x(g_x)\right]_{n,m} &= \frac{1}{\sqrt{N_x}} \exp\left(j\frac{2\pi}{M_x} n\left(m + \frac{g_x}{G_x}\right)\right), \\ \left[\mathbf{D}_y(g_y)\right]_{n,m} &= \frac{1}{\sqrt{N_y}} \exp\left(j\frac{2\pi}{M_y} n\left(m + \frac{g_y}{G_y}\right)\right), \end{aligned} \quad (20)$$

where i_1 indicates the index of $\mathbf{W}^1$ in the long-term feedback codebook, and g_x and g_y denote the indexes of the rotation DFT matrices for two directions, respectively. We have the following:

$$\begin{aligned} i_1 = G_y g_x + g_y, \quad & g_x = 0, 1, \ldots, G_x - 1, \\ & g_y = 0, 1, \ldots, G_y - 1. \end{aligned} \quad (21)$$

Take the URA-64 in Figure 2 as an example: we have $N_x = 8$, $N_y = 8$, and $\mathbf{W}^1$ with the size of $64 \times M_x M_y$.

The construction of the $M_x M_y \times 1\mathbf{W}^2$ is the same as the one for the ULA purpose (see formula (11)).

4. Evaluation

4.1. Channel Coverage. In this paper, for the rank-1 codebook which means that the number of spatial streams for a user is 1, we define the channel coverage as the gain using the codebook relative to the gain obtained by MF precoding with perfect CSIT:

$$C = E_{\mathbf{H}}\left[\frac{\left|\mathbf{H}\mathbf{W}^{\Gamma}(\mathbf{H})\right|^2}{\left|\mathbf{H}\mathbf{W}^{\text{opt}}(\mathbf{H})\right|^2}\right], \quad (22)$$

where $\mathbf{W}^{\Gamma}(\mathbf{H})$ indicates the codeword selected from the codebook Γ and $\mathbf{W}^{\text{opt}}(\mathbf{H}) = \mathbf{H}^*/\|\mathbf{H}\|_2$ is the optimal precoding matrix with perfect CSIT. The channel coverage can be used as a metric for the quality of a quantized codebook.

4.2. Sum Rate. In order to evaluate the precoding performance in a multiuser MIMO system, we can use the sum rate metric. For the downlink of the system, the optimal sum rate can be achieved by the interference presubtraction coding technique called dirty-paper coding (DPC), as long as the transmitter has perfect side information about the additive interference at the receiver [14]. The optimal DPC sum rate for the multiuser case is given as follows [15]:

$$R_{\text{DPC}} = E_{\mathbf{H}}\left[\max_{\mathbf{\Lambda}}\left(\log_2 \det\left(\mathbf{I}_{N_t} + \gamma \mathbf{H}^H \mathbf{\Lambda} \mathbf{H}\right)\right)\right], \quad (23)$$

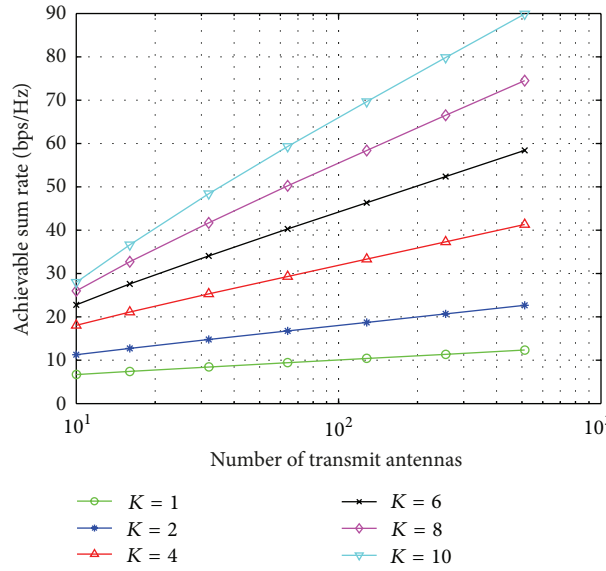

Figure 3: Optimal sum rate curves of different K values for $\gamma = 10$ dB.

where $\mathbf{\Lambda}$ is a $K \times K$ diagonal matrix for power allocation with factor λ_i on its main diagonal and $\sum \lambda_i = 1$.

Figure 3 depicts the optimal sum rate curves achieved by DPC for multiuser MIMO with K scheduled UEs equipped single-receive antenna under 10 dB SNR setting. Since the curves for different NLOS scenarios defined by [16], including urban macrocell (UMa), urban microcell (UMi), and indoor hotspot (InH) of the URA deployment are very close, we only draw the curves for the UMa scenario in this figure. From the result, we can see that the optimal sum rate increases linearly with the increase of the logarithm of N_t that is, we need to double the number of antennas in order to improve the capacity by roughly K bps/Hz. However, for large numbers of transmit antennas, the signal processing complexity, scheduling algorithm complexity for numerous users, and the CSI feedback overhead are significantly high, which may overshadow the capacity gain.

While the optimal sum rate can be used as the upper bound for the limited feedback precoding, the achievable sum rate of the precoding system using a quantized codebook can be used as an important indicator of the quality of the codebook [17]. For the multiuser MIMO system, if the channel estimation is considered to be ideal (i.e., $\widehat{\mathbf{H}}_k = \mathbf{H}_k$), the power of each transmit antenna is uniform, and the MF receiver is adopted (as shown in formula (6)) the instantaneous achievable sum rate can be expressed as

$$R(\mathbf{H}) = \sum_{k=1}^{K} \log_2\left(1 + \frac{\left\|\mathbf{H}_k \mathbf{W}_k\right\|_2^2}{K/\gamma + \sum_{i \neq k}\left\|\mathbf{H}_k \mathbf{W}_i\right\|_2^2}\right), \quad (24)$$

where K is the number of scheduled users, $\gamma = P_t/\sigma^2$ is the signal-to-noise ratio (SNR) with P_t as the total transmit

power, $\mathbf{H}_k$, the column vector of $\mathbf{H}$ denotes the channel matrix for UE k, and $\mathbf{W}_k$ is its requested codeword.

Derivation. The received signal for UE k can be expressed as

$$y_k = \mathbf{H}_k \mathbf{W}_k s_k + \sum_{i \neq k} \mathbf{H}_k \mathbf{W}_i s_i + z_k. \tag{25}$$

With formula (6), the demodulated signal can be written as

$$\begin{aligned} \widehat{s}_k &= \left(\mathbf{H}_k \mathbf{W}_k\right)^* y_k = \left|\mathbf{H}_k \mathbf{W}_k\right|^2 s_k \\ &\quad + \left(\mathbf{H}_k \mathbf{W}_k\right)^* \sum_{i \neq k} \mathbf{H}_k \mathbf{W}_i s_i + \left(\mathbf{H}_k \mathbf{W}_k\right)^* z_k. \end{aligned} \tag{26}$$

And the power of the demodulated signal is

$$\begin{aligned} E\left[\widehat{s}_k^* \widehat{s}_k\right] &= \left|\mathbf{H}_k \mathbf{W}_k\right|^4 E\left[s_k^* s_k\right] + \left|\mathbf{H}_k \mathbf{W}_k\right|^2 E\left[z_k^* z_k\right] \\ &\quad + \sum_{i \neq k} \left|\left(\mathbf{H}_k \mathbf{W}_k\right)^* \mathbf{H}_k \mathbf{W}_i\right|^2 E\left[s_i^* s_i\right] \\ &= \left|\mathbf{H}_k \mathbf{W}_k\right|^2 \left(\frac{P_t}{K}\left|\mathbf{H}_k \mathbf{W}_k\right|^2 + \sigma^2 + \frac{P_t}{K} \sum_{i \neq k} \left\|\mathbf{H}_k \mathbf{W}_i\right\|_2^2\right). \end{aligned} \tag{27}$$

Noting that the first term is the power of the wanted signal while the second and the third ones denote the power of the noise and the interference, we can compute the SINR as follows:

$$\mathrm{SINR} = \frac{\left(P_t/K\right)\left|\mathbf{H}_k \mathbf{W}_k\right|^2}{\sigma^2 + \left(P_t/K\right) \sum_{i \neq k} \left\|\mathbf{H}_k \mathbf{W}_i\right\|_2^2} = \frac{\left\|\mathbf{H}_k \mathbf{W}_k\right\|_2^2}{K/\gamma + \sum_{i \neq k} \left\|\mathbf{H}_k \mathbf{W}_i\right\|_2^2}. \tag{28}$$

Thus, we have the instantaneous achievable sum rate expression given by formula (24).

The ergodic achievable rate can be expressed as

$$R = E_{\mathbf{H}}\left(R\left(\mathbf{H}\right)\right). \tag{29}$$

In order to evaluate the codebooks with the achievable sum rate metric, we adopt the Monte-Carlo simulation method and take the arithmetic mean of the instantaneous values under different channel realizations as the output metric. The simulation flow is described by the pseudocode in Algorithm 1.

4.3. Results. Based on the evaluation metrics, we present some simulation results in this section. The Winner II channel model [18] can be used for the ULA deployment in the simulation. But it needs to be modified to support the URA deployment. Thus, we extend the model by associating elevation angles to paths generated by the original Winner II model and correlating elevation statistics with other large-scale fading parameters. Without loss of generality, we take the case of 64 transmit antennas as an example for the performance evaluation of different codebook designs under different scenarios. For the sake of clarity, the conventional ULA DFT codebook and the proposed URA DFT codebook are termed as DFT-ULA and DFT-URA, respectively.

```
// L: the total number of channel realizations
// N_u: the total number of UEs
// K: the number of scheduled UEs
Initialization
for l = 1 : L
    generate the channel matrix H
    for u = 1: N_u
        compute the requested codeword W_u
        report W_u to the BS
    end for
    scheduling: select K UEs from the N_u UEs
    form the precoder P
    compute the instantaneous rate R_l (formula (23))
end for
Compute the metric R̄ = (1/L) Σ_{l=1}^{L} R_l
output R̄
```

Algorithm 1: Simulation flow.

Table 1 gives the parameter configuration for the following simulations. As we are discussing the capability of codebooks to reflect the channel correlation, we focus on the design of the first codeword $\mathbf{W}^1$ for DFT codebooks; hence, we set $M = 1$, which means that the codebooks have only one second codeword; that is, $\mathbf{W}^2 = 1$.

4.3.1. Channel Coverage. With the fixed number of transmit antennas, the codebook can be enlarged in order to improve the quantization accuracy, but the feedback overhead would limit the codebook size and codeword selection complexity would become a significant bottleneck. Consequently, it is necessary for us to investigate the performance of codebooks with different feedback overhead limits. Figure 4 presents the channel coverage defined by formula (22) as a function of the feedback overhead (B) for the DFT-ULA, the DFT-URA, and the Kerdock codebook under different NLOS scenarios with the URA deployment. It is noted that the maximum number of codewords in the Kerdock codebook for 64-dimensional space is 4096, and thus, the curve ends at the point of 12-bit feedback overhead. From the curves, we can see that when the feedback overhead becomes larger than 10 bits, the improvement becomes insignificant. In conclusion, the 8~10 bits of feedback is adequate for 64 transmit antennas with the URA. This feedback overhead is close to that of LTE-Advanced Release 10 in which the 8-bit rank-1 codebook for eight crosspolarized antennas is utilized [19]. Besides, effective approaches [20] can be used to further reduce the feedback overhead.

4.3.2. Achievable Sum Rate. We have run the multiuser MIMO simulation described in Algorithm 1 with 10-bit feedback overhead (i.e., $B = 10$), and the results are shown in Figures 5 and 6.

Table 1: Simulation configuration.

Parameter	Value
Channel model	UMa NLOS; UMi NLOS; InH NLOS
BS antenna setup	URA, 64 copolarized antennas, and $\lambda/2$ spacing
UE antenna setup	Single antenna
System frequency (GHz)	2.1
Number of channel realizations	1000
Number of UEs	10
Scheduling criteria	Minimizing the codeword correlation coefficient
Number of DFT matrices	
DFT-ULA	$G = 2^B$
DFT-URA	$G_x = G_y = 2^{B/2}$
Size of DFT matrices	
DFT-ULA	$N = 64,\ M = 1$
DFT-URA	$N_x = N_y = 8,\ M_x = M_y = 1$

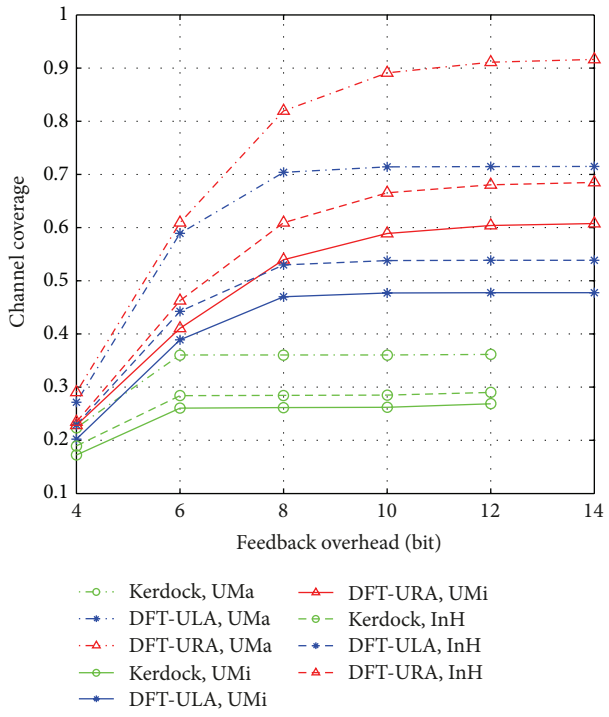

Figure 4: Channel coverage as a function of the feedback overhead.

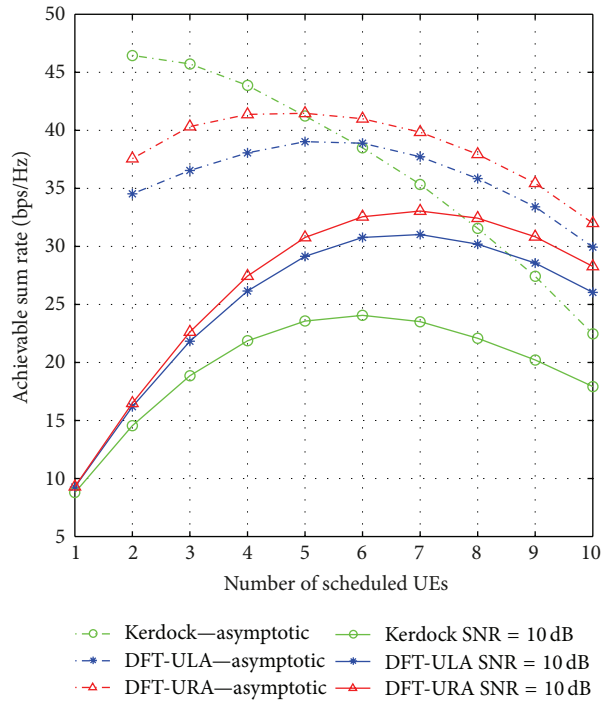

Figure 5: Achievable sum rate as a function of K for $\gamma \to \infty$ and $\gamma = 10$ dB.

Figure 5 illustrates the curves as a function of the number of scheduled UEs (K) in the UMa scenario. From the curves, we can see that the DFT-URA outperforms the other codebooks for different number of UEs with $\gamma = 10$ dB. Figure 5 also shows the asymptotic curves as $\gamma \to \infty$, which measure the impact of the interuser interference. The gap between the DFT-URA and the DFT-ULA indicates that the DFT-URA can better mitigate the inter-user interference. Besides, in the capability of the inter-user interference suppression, the DFT-URA defeats the Kerdock when the number of scheduled UEs is relatively large ($K > 5$), since the DFT-URA is able to provide more beams targeting at more UEs separated in different angular positions.

Figure 6 depicts the achievable sum rate of the Kerdock, the DFT-ULA, and the DFT-URA for four scheduled UEs ($K = 4$) as a function of SNR under the three scenarios; the theoretical curves drawn by formula (23) with perfect CSIT are presented as the upper bound. The results indicate that the DFT-URA designed to the URA deployment has remarkable performance gain compared to the DFT-ULA and especially the Kerdock codebook under different scenarios. It is because the design based on the Kronecker-type approximation of

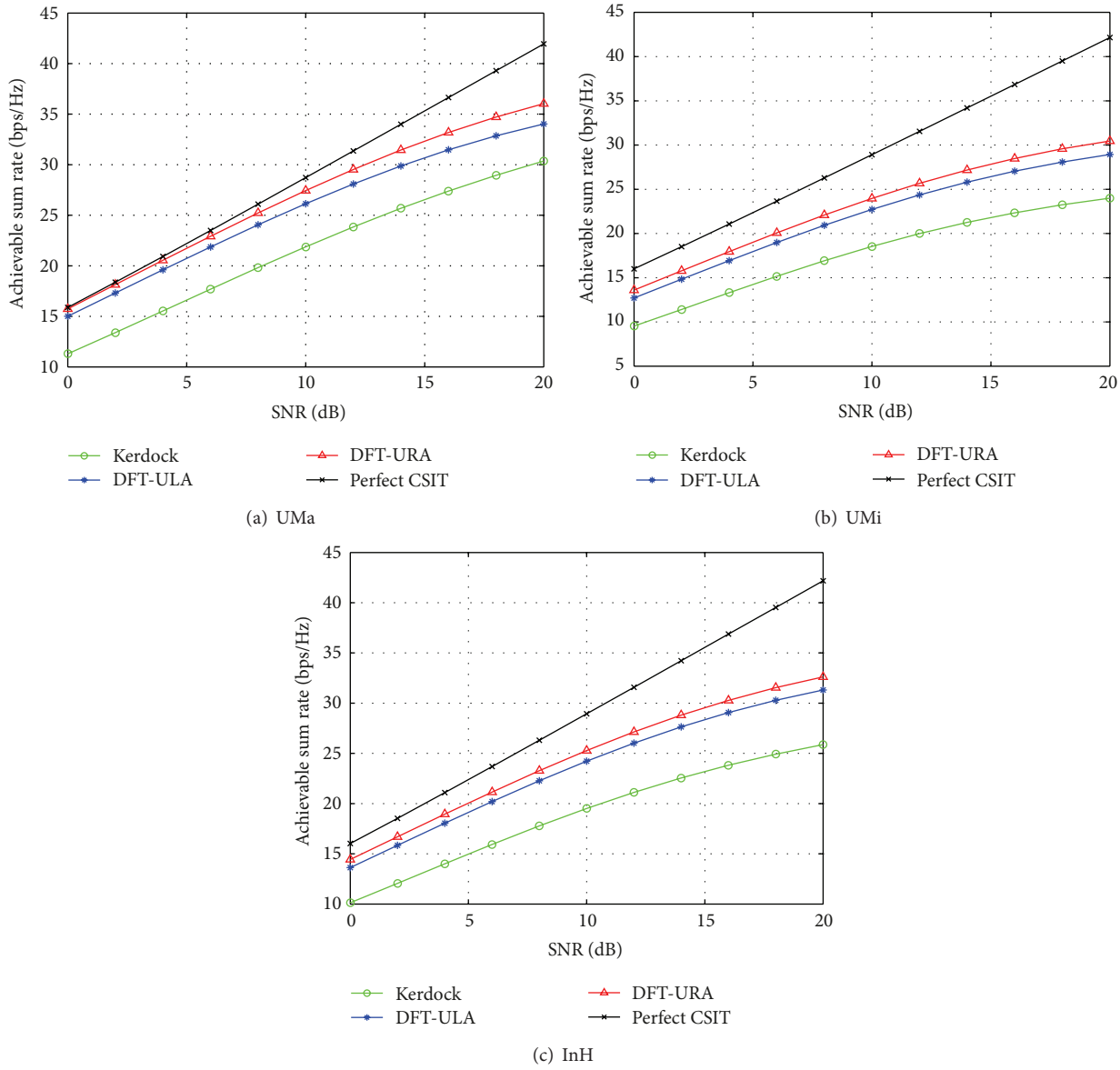

Figure 6: Achievable sum rate with $K = 4$. (a) Uma, (b) UMi, and (c) InH.

the array correlation structure better reflects the channel property with the URA, and thus physically leads to more accurate beams, making it suitable for multiuser MIMO in the case where UEs are separated spatially in angular domain. In addition, the performance in the UMa scenario is better than the other two scenarios, since this scenario has stronger channel correlation, making the DFT vectors better adapt to the channel.

5. Conclusion

In this paper, we discussed the limited feedback precoding techniques for the downlink of massive MIMO systems. On the theoretical basis of Kronecker-type approximation of the array correlation structure, we proposed a novel codebook design for the URA deployment of the numerous closely spaced antennas, which would be probably adopted by massive MIMO. This codebook design constructs the first codeword representing the whole long-term channel correlation in the plane with the Kronecker product of two DFT matrices generated for two orthogonal ULAs. We proved the validity of this construction theoretically, and verified that the proposed codebook outperforms other kinds of codebooks in terms of the channel coverage and the achievable sum rate under various scenarios via simulations. The proposed codebook design can contribute to precoding solutions for large-scale array antenna technologies, which would be probably applied to future Beyond 4 G systems. Our future work will consider advanced multiuser scheduling algorithms as well as robust receiving algorithms for massive MIMO.

Acknowledgments

This work was supported by Beijing Natural Science Foundation funded project (no. 4110001), National S&T Major Project (no. 2013ZX03003003-003), and Samsung Company.

References

[1] F. Rusek, D. Persson, B. K. Lau et al., "Scaling up MIMO: opportunities and challenges with very large arrays," *IEEE Signal Processing Magazine*, vol. 30, no. 1, pp. 40–60, 2013.

[2] E. Visotsky and U. Madhow, "Space-time transmit precoding with imperfect feedback," *IEEE Transactions on Information Theory*, vol. 47, no. 6, pp. 2632–2639, 2001.

[3] T. Inoue and R. W. Heath Jr., "Kerdock codes for limited feedback precoded MIMO systems," *IEEE Transactions on Signal Processing*, vol. 57, no. 9, pp. 3711–3716, 2009.

[4] J. C. Roh and B. D. Rao, "Design and analysis of MIMO spatial multiplexing systems with quantized feedback," *IEEE Transactions on Signal Processing*, vol. 54, no. 8, pp. 2874–2886, 2006.

[5] D. J. Love and R. W. Heath Jr., "Limited feedback unitary precoding for spatial multiplexing systems," *IEEE Transactions on Information Theory*, vol. 51, no. 8, pp. 2967–2976, 2005.

[6] K. Schober, R. Wichman, and T. Koivisto, "MIMO adaptive codebook for closely spaced antenna arrays," in *Proceedings of the European Signal Processing Conference (EUSIPCO '11)*, pp. 1–5, Barcelona, Spain, August 2011.

[7] D. J. Ryan, I. V. L. Clarkson, I. B. Collings, D. Guo, and M. L. Honig, "QAM codebooks for low-complexity limited feedback MIMO beamforming," in *Proceedings of the IEEE International Conference on Communications (ICC '07)*, pp. 4162–4167, June 2007.

[8] A. L. Moustakas, H. U. Baranger, L. Balents, A. M. Sengupta, and S. H. Simon, "Communication through a diffusive medium: coherence and capacity," *Science*, vol. 287, no. 5451, pp. 287–290, 2000.

[9] T. Shuang, T. Koivisto, H.-L. Määttänen, K. Pietikäinen, T. Roman, and M. Enescu, "Design and evaluation of LTE-Advanced double codebook," in *Proceedings of the IEEE 73rd Vehicular Technology Conference (VTC '11)*, pp. 1–5, Yokohama, Japan, May 2011.

[10] A. M. Sayeed, "Deconstructing multiantenna fading channels," *IEEE Transactions on Signal Processing*, vol. 50, no. 10, pp. 2563–2579, 2002.

[11] K. Amiri, D. Shamsi, B. Aazhang, and J. R. Cavallaro, "Adaptive codebook for beamforming in limited feedback MIMO systems," in *Proceedings of the 42nd Annual Conference on Information Sciences and Systems (CISS '08)*, pp. 994–998, March 2008.

[12] G. Levin and S. Loyka, "On capacity-maximizing angular densities of multipath in MIMO channels," in *Proceedings of the 72nd Vehicular Technology Conference Fall (VTC '10)*, Ottawa, Canada, September 2010.

[13] C. F. V. Loan, "The ubiquitous Kronecker product," *Journal of Computational and Applied Mathematics*, vol. 123, no. 1-2, pp. 85–100, 2000.

[14] A. Paulraj, R. Nabar, and D. Gore, *Introduction To Space-Time Wireless Communications*, Cambridge University Press, Cambridge, UK, 2003.

[15] X. Gao, O. Edfors, F. Rusek, and F. Tufvesson, "Linear precoding performance in measured very-large MIMO channels," in *Proceedings of the 74th Vehicular Technology Conference (VTC '11)*, San Francisco, Calif, USA, September 2011.

[16] Rec. ITU-R M. 1225, guidelines for evaluation of radio transmission technologies for IMT-2000, 1998.

[17] J. C. Roh and B. D. Rao, "Design and analysis of MIMO spatial multiplexing systems with quantized feedback," *IEEE Transactions on Signal Processing*, vol. 54, no. 8, pp. 2874–2886, 2006.

[18] "IST-WINNER II Deliverable 1. 1. 2 v. 1. 2. WINNER II Channel Models, IST-WINNER2," Tech. Rep., 2007, http://www.ist-winner.org/deliverables.html.

[19] "Evolved Universal Terrestrial Radio Access (E-UTRA), Physical layer procedures," 3GPP TS 36. 213 V10. 6. 0, 2012.

[20] E. Jorswieck, A. Sezgin, B. Ottersten, and A. Paulraj, "Feedback reduction in uplink MIMO OFDM systems by chunk optimization," *Eurasip Journal on Advances in Signal Processing*, vol. 2008, Article ID 597072, pp. 1–14, 2008.

Hindawi Publishing Corporation
International Journal of Antennas and Propagation
Volume 2013, Article ID 298538, 8 pages
http://dx.doi.org/10.1155/2013/298538

Research Article

Full-Wave Analysis of Microstrip Antennas in Three-Layered Spherical Media

Tao Yu and Chengyou Yin

Department of Radar Engineering, Hefei Electronic Engineering Institute, 460 Huangshan Road, Hefei, Anhui 230037, China

Correspondence should be addressed to Chengyou Yin; cyouyin@sina.com

Received 31 December 2012; Revised 29 June 2013; Accepted 16 July 2013

Academic Editor: Mugen Peng

A model of three-layered spherical microstrip antenna has been analyzed based on Rao-Wilton-Glisson (RWG) triangular basis functions using mixed potential integral equation (MPIE). Firstly, the model of antenna and the dyadic Green's function in spherical microstrip antennas are given at the beginning of this paper. Then, due to the infinite series convergence problem, asymptotic extraction approach is presented to accelerate the Green's functions convergence speed when source and field points are located in the same layer and different layers. The convergence speed can be accelerated observably by using this method. Finally, in order to simplify impedance matrix elements calculation at the junction of the probe and patch, a novel division fashion of pair of triangles is adopted in this paper. The input impedance result obtained shows the validity and effectiveness of the analysis method comparing with published data.

1. Introduction

Nowadays, conformal microstrip antennas have been the subject of several research works, where cylindrical, spherical, and conical microstrip antennas have been studied [1–3]. Among the studies, the spherical microstrip antenna is found to be helpful in improving width of beam problem involved with the planar arrays at low elevation [4]. The spherical microstrip antenna is the emphasis of research in this paper.

Several methods have been used to analyze the characteristics of spherical microstrip antenna. The analysis methods include mainly generalized transmission line model (GTLM) analysis, cavity model theory, and full-wave method. The process of the GTLM analysis [5] and cavity model theory [6] is simple; however, the result obtained is accurate only when the substrate thickness is much smaller than wavelength and the radius of the sphere ($h/\lambda < 0.01$). On the contrary, the full-wave method [7] is complicated with accurate and rigorous calculated result, which is adopted widely without the substrate thickness limitation.

In aforementioned study methods, the method of moments based on full-wave solution has been adopted widely in analysis. In general, Green's functions should be considered in the calculated process. The dyadic Green's functions for simple spherical geometry have been presented earlier in [8]. A general expression of dyadic Green's functions in a spherically arbitrary multilayered medium is introduced in [9, 10] by applying the method of scattering superposition, where the functions have been expressed in the form of an infinite series of spherical eigenmodes. Another type of Green's function has been given by using the GLDMULT algorithm that calculates spectral-domain Green's function of multilayer spherical, circular, cylindrical, and planar structures, and more details about GLDMULT algorithm can be found in [11]. Based on the GLDMULT algorithm, spherical stacked-patch arrays with emphasis on the physical interpretation of mutual coupling are analyzed in [12]. In [13], a rigorous MoM model that can be used to analyze spherical antennas of any configuration and substrate thickness is presented, and the dyadic Green's functions are decomposed into fast and slow convergent parts, with the slower part incorporated into a single scalar potential expression. Other jobs have been done to accelerate the infinite summation convergence [14, 15], with the source and field points located in the same layer and different layers. A probe-fed circularly polarized loop antenna printed on a layered dielectric sphere has been studied in [16].

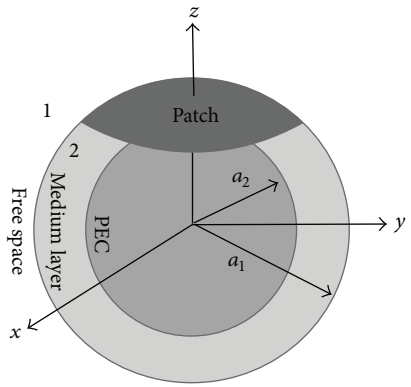

Figure 1: The microstrip antenna in a layered spherical media.

In this paper, the model of three-layered spherical microstrip antenna is established, where the problem about substrate thickness and feeding probe is considered. The method of moment based on Rao-Wilton-Glisson triangular basis functions and the dyadic Green's functions in [9] is used in the model using mixed potential integral equation (MPIE). Asymptotic extraction approach is presented to accelerate the Green's functions convergence speed, and a novel division fashion of pair of triangles is adopted to simplify impedance matrix at the junction of the probe and patch. The input impedance of microstrip antennas in spherically layered media is calculated, and calculated results of the input impedance are in good agreement with published data, which shows the validity and effectiveness of the analysis method.

2. Theory and Formulation

The model of three-layered spherical microstrip antenna is presented in Figure 1. The patch is located in the free space while the probe is located in the medium layer. A conducting spherical core can be modeled as the inner-most layer.

2.1. Expressions of Dyadic Green's Functions. The electromagnetic dyadic Green's functions in the layered media have been deduced in detail in [9]. The dyadic Green's function can be considered as the sum of an unbounded dyadic Green's function $\overline{\mathbf{G}}_{oe}(\mathbf{r},\mathbf{r}')$ and a scattering dyadic Green's function $\overline{\mathbf{G}}_{es}^{(fs)}(\mathbf{r},\mathbf{r}')$, and the unbounded dyadic Green's function can be expressed as

$$\overline{\mathbf{G}}_{oe}\left(\mathbf{r},\mathbf{r}'\right)=\left(\overline{\mathbf{I}}+\frac{1}{k_s^2}\nabla\nabla'\right)\frac{e^{-jk_s|\mathbf{r}-\mathbf{r}'|}}{4\pi\left|\mathbf{r}-\mathbf{r}'\right|}, \tag{1}$$

which can be employed only when the source and field points are located in the same layer [13]. In this paper, according to research requirement, four types of $\overline{\mathbf{G}}_{es}^{(fs)}(\mathbf{r},\mathbf{r}')$ should be considered (f denotes the layer number of field point's position and s denotes the layer number of source point's position as shown in Figure 1), including $\overline{\mathbf{G}}_{es}^{(11)}(\mathbf{r},\mathbf{r}')$, $\overline{\mathbf{G}}_{es}^{(21)}(\mathbf{r},\mathbf{r}')$, $\overline{\mathbf{G}}_{es}^{(12)}(\mathbf{r},\mathbf{r}')$, and $\overline{\mathbf{G}}_{es}^{(22)}(\mathbf{r},\mathbf{r}')$. To save the space, the expression of all types of Green's functions will not be given here. Only take $\overline{\mathbf{G}}_{es}^{(11)}(\mathbf{r},\mathbf{r}')$ for example:

$$\begin{aligned}\overline{\mathbf{G}}_{es}^{(11)}\left(\mathbf{r},\mathbf{r}'\right)&=\frac{-jk_1}{4\pi}\sum_{n=1}^{\infty}\sum_{m=0}^{n}\left(2-\delta_m^0\right)\frac{2n+1}{n(n+1)},\\ &\frac{(n-m)!}{(n+m)!}\times\begin{bmatrix}\mathbf{M}^{(2)e}{}_{omn}(k_1)\,B_M^{11}\mathbf{M}'^{(2)e}{}_{omn}(k_1)\\ +\mathbf{N}^{(2)e}{}_{omn}(k_1)\,B_N^{11}\mathbf{N}'^{(2)e}{}_{omn}(k_1)\end{bmatrix},\end{aligned} \tag{2}$$

where vector eigenfunctions $\mathbf{M}^{(2)}$, $\mathbf{M}'^{(2)}$, $\mathbf{N}^{(2)}$, and $\mathbf{N}'^{(2)}$ can be found in [9]. In this case, (2) represents Green's function that both the source and field points are located in the free space, and the coefficients B_M^{11}, B_N^{11} are derived and presented by

$$B_{M,N}^{11}=-\frac{R_{F1}^{H,V}\cdot T_{P1}^{H,V}+T_{F1}^{H,V}\cdot R_{F2}^{H,V}}{T_{P1}^{H,V}+R_{F2}^{H,V}R_{P1}^{H,V}T_{F1}^{H,V}}, \tag{3}$$

where the equivalent reflection and transmission coefficients $R_{(P,F)f}^{H,V}$, $T_{(P,T)f}^{H,V}$ can be calculated by [9] and cannot be given here. The scattering dyadic Green's function $\overline{\mathbf{G}}_{es}^{(11)}(\mathbf{r},\mathbf{r}')$ contains nine components, which can be obtained through the substitution of general expressions of vector eigenfunction for (2). Take $\widehat{\boldsymbol{\theta}}\widehat{\boldsymbol{\theta}}$ component, for example,

$$G_{\theta\theta}^{11}=\frac{-jk_1}{4\pi}\sum_{n=1}^{\infty}\frac{2n+1}{n(n+1)}\left\{\begin{array}{l}B_M^{11}h_n^{(2)}(k_1r)\,h_n^{(2)}\left(k_1r'\right)\alpha\\ \quad+B_N^{11}\dfrac{1}{k_1^2rr'}\dfrac{d\left[rh_n^{(2)}(k_1r)\right]}{dr}\\ \quad\times\dfrac{d\left[r'h_n^{(2)}\left(k_1r'\right)\right]}{dr'}\beta\end{array}\right\}, \tag{4}$$

where

$$\begin{aligned}\alpha&=-\sin^2\left(\phi-\phi'\right)\sin\theta\sin\theta'\frac{P_n^2(\cos\gamma)}{(\sin\gamma)^2}\\ &\quad+\cos\left(\phi-\phi'\right)\frac{\partial P_n(\cos\gamma)}{\partial\cos\gamma},\end{aligned} \tag{5a}$$

$$\begin{aligned}\beta&=\frac{{P_n}^2(\cos\gamma)}{(\sin\gamma)^2}\left(-\cos\theta\sin\theta'+\sin\theta\cos\theta'\cos\left(\phi-\phi'\right)\right)\\ &\quad\times\left(-\sin\theta\cos\theta'+\cos\theta\sin\theta'\cos\left(\phi-\phi'\right)\right)\\ &\quad+\frac{\partial P_n(\cos\gamma)}{\partial\cos\gamma}\\ &\quad\times\left(\sin\theta\sin\theta'+\cos\theta\cos\theta'\cos\left(\phi-\phi'\right)\right),\end{aligned} \tag{5b}$$

$$\cos\gamma=\cos\theta\cos\theta'+\sin\theta\sin\theta'\cos\left(\varphi-\varphi'\right), \tag{5c}$$

$h_n^{(2)}(k_1 r)$ is the spherical Hankel function of the second type, $P_n(\cos\gamma)$ is the Legendre function of degree n, and $P_n^2(\cos\gamma)$ is the associated Legendre function of the first kind with the order 2 and degree n.

Each component of the scattering dyadic Green's functions can be expressed as an infinite summation of spherical harmonic and be constitutive of two components. Take (4) for example; the first part represents the TE modes, and the second one represents TM modes. Proper truncation of the summation is essential for an infinite summation. The summation of the TE modes converges much faster than that of the corresponding TM modes according to the asymptotic spherical Bessel and Hankel functions, and in order to improve the computation efficiency, TM modes of nine components are incorporated into a unified potential G_φ [13].

The electric field can be expressed using the scattering dyadic Green's functions

$$\mathbf{E}(\mathbf{r}) = -j\omega\mu_f \iint_s \overline{\mathbf{G}}_{es}^{fs}\left(\mathbf{r},\mathbf{r}'\right)\cdot\mathbf{J}_s\left(\mathbf{r}'\right)ds'. \tag{6}$$

Equation (6) also can be expressed as

$$\mathbf{E}(\mathbf{r}) = -j\omega\mu_f \iint_s \left(\overline{\mathbf{G}}_{es}^{\mathrm{TE}}\left(\mathbf{r},\mathbf{r}'\right) + \overline{\mathbf{G}}_{es}^{\mathrm{TM}}\left(\mathbf{r},\mathbf{r}'\right)\right)\cdot\mathbf{J}_s\left(\mathbf{r}'\right)ds', \tag{7a}$$

$$\mathbf{E} = -j\omega\mathbf{A} - \nabla\phi, \tag{7b}$$

where

$$\mathbf{A} = \mu_f \iint_{s'} \overline{\mathbf{G}}_A\cdot\mathbf{J}_s\left(r'\right)ds', \tag{8a}$$

$$\phi = \iint_{s'} \nabla' G_\varphi\cdot\mathbf{J}_s\left(r'\right)ds'. \tag{8b}$$

We can regard the magnetic vector potential $\mathbf{A}$ and the potential scalar ϕ as TM modes contributions and TE modes contributions, respectively. Then

$$\begin{aligned}\overline{\mathbf{G}}_A &= \overline{\mathbf{G}}_{es}^{\mathrm{TE}},\\ \nabla\phi &= j\omega\mu_f \iint_s \overline{\mathbf{G}}_{es}^{\mathrm{TM}}\left(\mathbf{r},\mathbf{r}'\right)\cdot\mathbf{J}_s\left(\mathbf{r}'\right)ds',\end{aligned} \tag{9}$$

where $\overline{\mathbf{G}}_A$, G_φ can be found in [13].

2.2. Asymptotic Dyadic Green's Functions. In this paper, asymptotic extraction approach has been adopted which can accelerate the infinite summation convergence [14]. This can be completed by using the large order spherical Bessel and Hankel functions principal asymptotic expressions:

$$j_n(kr) \approx \sqrt{\frac{1}{2kr(2n+1)}}\left(\frac{ekr}{2n+1}\right)^{n+(1/2)} \quad n\longrightarrow\infty, \tag{10a}$$

$$h_n^{(2)}(kr) \approx j\sqrt{\frac{2}{kr(2n+1)}}\left(\frac{ekr}{2n+1}\right)^{-n-(1/2)} \quad n\longrightarrow\infty, \tag{10b}$$

$$\frac{d\left[rj_n(kr)\right]}{dr} \approx nj_n(kr) \quad n\longrightarrow\infty, \tag{10c}$$

$$\frac{d\left[rh_n^{(2)}(kr)\right]}{dr} \approx -nh_n^{(2)}(kr) \quad n\longrightarrow\infty. \tag{10d}$$

When the source and field points are located in the free space (the first layer), the Green's function coefficients are shown as

$$B_M^{11}\big|_a \approx 0, \tag{11a}$$

$$B_N^{11}\big|_a = -\frac{\varepsilon_1-\varepsilon_2}{\varepsilon_1+\varepsilon_2}\frac{j_n(k_1a_1)}{h_n^{(2)}(k_1a_1)} - \frac{\varepsilon_2-\varepsilon_3}{\varepsilon_2+\varepsilon_3}\frac{j_n(k_1a_2)}{h_n^{(2)}(k_1a_2)}, \tag{11b}$$

where the subscript a denotes an asymptotic expression. It can be seen that TE modes coefficients asymptote to zero when n is large, while TM modes coefficients depend on the wave reflections at the dielectric. The asymptotic dyadic Green's function can be presented, and take $\widehat{\boldsymbol{\theta}}\widehat{\boldsymbol{\theta}}$ component for example:

$$G_{\theta\theta}^{11}\big|_a = \frac{-jk_1}{4\pi} \times\sum_{n=1}^{\infty}\frac{2n+1}{n(n+1)}\left\{\begin{array}{c} B_N^{11}\dfrac{d\left[rh_n^{(2)}(k_1r)\right]}{dr}\dfrac{d\left[r'h_n^{(2)}\left(k_1r'\right)\right]}{dr'} \\ \times\dfrac{1}{k_1^2rr'}\dfrac{\partial^2P_n(\cos\gamma)}{\partial\theta\,\partial\theta'}\end{array}\right\}; \tag{12}$$

using (10d), (12) can be written as

$$G_{\theta\theta}^{11}\big|_a = \frac{-j}{4\pi k_1} \times\sum_{n=1}^{\infty}(2n+1)\left\{\begin{array}{c}\left[B_N^{11}\big|_a\, h_n^{(2)}(k_1r)\; h_n^{(2)}\left(k_1r'\right)\right] \\ \times\dfrac{1}{rr'}\dfrac{\partial^2P_n(\cos\gamma)}{\partial\theta\,\partial\theta'}\end{array}\right\}, \tag{13}$$

where one assumes $(n+1) \approx n$ for large n. The other asymptotic $\overline{\mathbf{G}}_{es}^{(11)}(\mathbf{r},\mathbf{r}')$ components can be derived in the same way and then incorporated into a unified expression:

$$\overline{\mathbf{G}}_{es}^{11}|_a = \nabla\nabla' G_1 = \frac{j}{4\pi k_1}\nabla\nabla'\sum_{n=0}^{\infty}(2n+1)\,P_n(\cos\gamma) \times\left\{\left(-\frac{\varepsilon_1-\varepsilon_2}{\varepsilon_1+\varepsilon_2}\right)\frac{a_1}{r}\times j_n\left(k_1\frac{a_1^2}{r}\right)h_n^{(2)}(k_1 r') - \left(\frac{\varepsilon_2-\varepsilon_3}{\varepsilon_2+\varepsilon_3}\right)\frac{a_2}{r}\times h_n^{(2)}\left(k_1\frac{a_2^2}{r}\right)j_n(k_1 r')\right\}; \tag{14}$$

with the aid of the addition theorem of the spherical Hankel function

$$\frac{e^{-jk|\mathbf{r}-\mathbf{r}'|}}{4\pi|\mathbf{r}-\mathbf{r}'|} = \frac{-jk}{4\pi}\sum_{n=0}^{\infty}(2n+1)\,h_n^{(2)}(kr')\,j_n(kr)\,P_n(\cos\gamma), \tag{15}$$

equation (14) can be reduced to

$$\overline{\mathbf{G}}_{es}^{11}|_a = \nabla\nabla' G_2 = \frac{j}{4\pi k_1^2}\nabla\nabla' \times\left(\left(-\frac{\varepsilon_1-\varepsilon_2}{\varepsilon_1+\varepsilon_2}\right)\frac{a_1}{r}\frac{e^{-jk_1R_1}}{R_1}+\left(-\frac{\varepsilon_2-\varepsilon_3}{\varepsilon_2+\varepsilon_3}\right)\frac{a_2}{r}\frac{e^{-jk_1R_2}}{R_2}\right), \tag{16}$$

where $R_1 = \sqrt{r'^2+(a_1^2/r)^2-2r'(a_1^2/r)\cos\gamma}$, $R_2 = \sqrt{r'^2+(a_2^2/r)^2-2r'(a_2^2/r)\cos\gamma}$, then $\overline{\mathbf{G}}_{es}^{(11)}(\mathbf{r},\mathbf{r}')$ can be expressed as

$$\overline{\mathbf{G}}_{es}^{11} = \left(\overline{\mathbf{G}}_{es}^{11} - \nabla\nabla' G_1\right) + \nabla\nabla' G_2, \tag{17}$$

and $\nabla\nabla' G_1$, $\nabla\nabla' G_2$ are given by (14), (16), respectively. The component in (17) right hand bracket is the infinite summation of spherical harmonic; however the Green's functions convergence speed is accelerated. The other component is a close-form representation and can be treated as similar as that of unbounded dyadic Green's function (1). Asymptotic dyadic Green's functions of $\overline{\mathbf{G}}_{es}^{(21)}(\mathbf{r},\mathbf{r}')$, $\overline{\mathbf{G}}_{es}^{(12)}(\mathbf{r},\mathbf{r}')$, and $\overline{\mathbf{G}}_{es}^{(22)}(\mathbf{r},\mathbf{r}')$ can be obtained in the same way, which are given in the Appendix.

2.3. MoM Solution. The method of moments based on Rao-Wilton-Gilson triangular basis function is adopted in the model using the mixed potential integral equation (MPIE), where the antenna surface and probe are divided into a mesh of triangular patches as shown in Figure 2, and the probe is modeled by strip. A problem that needs special attention is the connection of the feeding probe to the patch. A possible solution [13] is introduced by the double use of the edge shared by the probe and the patch, where the common triangle is located in the probe as shown in Figure 3, which is

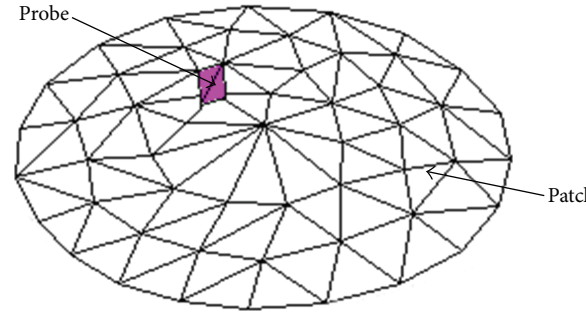

Figure 2: Mesh of triangular patches.

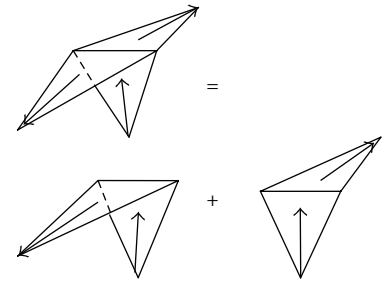

Figure 3: Division fashion of pair of triangles in [13].

efficient in [13] because the probe and the patch are located in the same layer, where only a type of dyadic Green's function $\overline{\mathbf{G}}_{es}^{(22)}(\mathbf{r},\mathbf{r}')$ is used in the model.

In this paper, the analysis process is complicated if the aforementioned division fashion is adopted since there are two pairs of RWG basis functions at the junction. A novel division fashion of pair of triangles is adopted to simplify impedance matrix where the common triangle is located in the patch as shown in Figure 4, and only a pair of RWG basis function positions at the junction.

The impedance matrix elements can be calculated based on MoM using the mixed potential integral equation (MPIE):

$$Z_{mn} = \left\langle\left(j\omega\mathbf{A}_n + \nabla\phi_n\right), \mathbf{f}_m\right\rangle, \tag{18}$$

where $\mathbf{f}_m$ is testing basis function, and

$$\langle\nabla\phi, \mathbf{f}_m\rangle = \int_s \nabla\cdot(\phi\mathbf{f}_m)\,dS - \int_s \phi\nabla\cdot\mathbf{f}_m dS, \tag{19}$$

using Gauss theorem

$$\int_s \nabla\cdot(\phi\mathbf{f}_m)\,dS = \oint_l \phi\mathbf{f}_m\cdot\hat{\mathbf{n}}dl, \tag{20}$$

where l are three edges around the triangle and $\hat{\mathbf{n}}$ is normal unit vector. The term $\mathbf{f}_m\cdot\hat{\mathbf{n}}$ equals zero on the boundary edge. To the common edge, (20) equals zero because the component of function normal to the common edge is unity.

An undesirable line integral will appear at the junction as shown in Figure 5 if the Gauss theorem is employed to transfer the differential operators ∇ or ∇' [17] just because the ϕ in the two triangles at the junction are not identical.

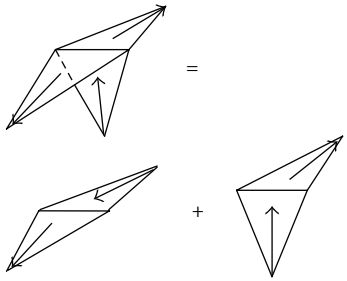

Figure 4: Division fashion of pair of triangles in this paper.

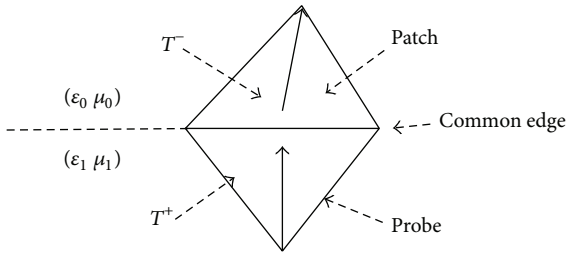

Figure 5: The triangle pair at the junction.

For example, when source point is located in the triangle pair at the patch and field point is located in the triangle pair at the junction,

$$\begin{aligned}\langle \nabla\phi, \mathbf{f}_m \rangle &= \int_s \nabla\cdot(\phi\mathbf{f}_m)\,dS - \int_s \phi\nabla\cdot\mathbf{f}_m dS \\ &= \oint_l \phi\mathbf{f}_m\cdot\hat{\mathbf{n}}\,dl - \int_s \phi\nabla\cdot\mathbf{f}_m dS \\ &= \int_l \phi_2\mathbf{f}_m^+\cdot\hat{\mathbf{n}}^+ dl + \int_l \phi_1\mathbf{f}_m^-\cdot\hat{\mathbf{n}}^- dl \\ &\quad - \int_{T^+} \phi_2\nabla\cdot\mathbf{f}_m^+ dS - \int_{T^-} \phi_1\nabla\cdot\mathbf{f}_m^- dS,\end{aligned} \tag{21}$$

where l is the common edge as shown in Figure 5. ϕ_2 is the electric scalar when source is located in the first layer and field is located in the second layer; and ϕ_1 is the one when source locates in the first layer and field is located in the first layer.

The integration over the testing triangle surface and line is avoided through using the approximate Galerkin method, in which testing functions can be implemented at the centroid of the triangle and line. The surface integral over the source triangle is calculated using symmetric quadrature rules over the triangle.

Noticeably, calculating the self-element of impedance matrix at the junction is much complicated because four types of the dyadic Green's functions will be calculated, and difficult line integral singularity will also be met. The calculation formulation when both source and field triangle pairs position at the junction is as same as (21), but the meaning of ϕ_2 and ϕ_1 is not same as the ones of (21). ϕ_2 is the electric scalar when field is located in the second layer, and ϕ_1 is the one when field is located in the first layer. The

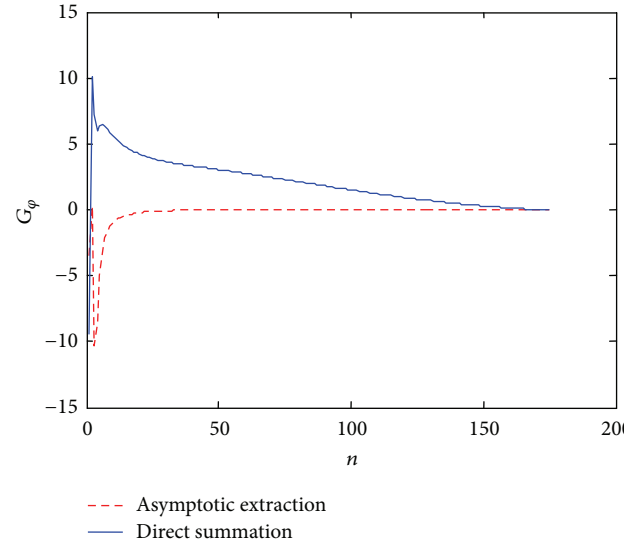

Figure 6: Convergence of G_φ^{11} when source and field points are located in the same triangle at the patch.

position of source is in the first layer and second layer. In this case, the first term of (21) can be expressed as

$$\begin{aligned}&\int_l \phi_2\mathbf{f}_m^+\cdot\hat{\mathbf{n}}^+ dl \\ &\quad= \int_l\int_{s'} \nabla' G_\varphi\cdot\mathbf{f}_n dS' dl \\ &\quad= \int_l\int_{l'} G_\varphi^{(22)}\mathbf{f}_n^+\cdot\hat{\mathbf{n}}^+ dl\,dl' + \int_l\int_{l'} G_\varphi^{(21)}\mathbf{f}_n^-\cdot\hat{\mathbf{n}}^- dl\,dl' \\ &\qquad - \int_l\int_{T^+} G_\varphi^{(22)}\nabla'\cdot\mathbf{f}_n^+ dS' dl - \int_l\int_{T^-} G_\varphi^{(21)}\nabla'\cdot\mathbf{f}_n^- dS' dl.\end{aligned} \tag{22}$$

Then, (21) can be decomposed as 16 terms involving the calculation of four types of the dyadic Green's functions. Besides, the line integral singularity will be met when calculating (22):

$$f = \int_l\int_{l'} \frac{1}{|\mathbf{r}-\mathbf{r}'|} dl\,dl'. \tag{23}$$

Hence, calculating the self-element of impedance matrix at the junction is much complicated. The patch is positioned at the interface between the two layers, and it can be regarded as being located at the bottom of free space or the top of the medium layer. Then, a smart method is regarding the two triangles at the junction as being located in the medium layer when calculating the self-element of impedance matrix at the junction.

3. Calculated Results

In this paper, the presented example in [13] has also been adopted, where the radius of the PEC spherical core is 5 cm, with a spherical medium of $\varepsilon_2 = 2.47$ and a 0.32 cm thickness.

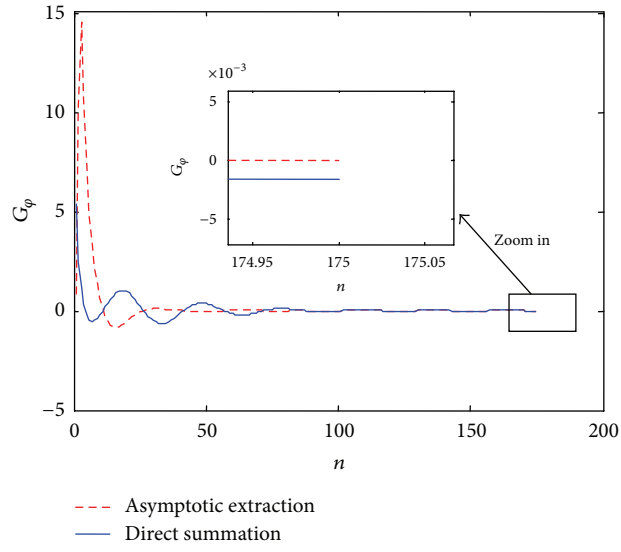

FIGURE 7: Convergence of G_φ^{12} when source is located in the patch and field locate in the probe.

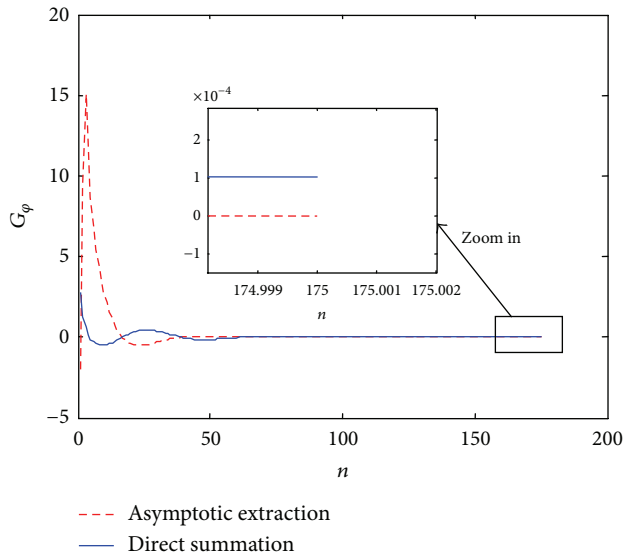

FIGURE 8: Convergence of G_φ^{21} when source is located in the probe and field locate in the patch.

The conformal patch has an arc radius of 1.88 cm, and the probe is located in an arc distance of 0.94 cm from the center of the patch. The width of the probe is 0.2 cm. A delta gap voltage source has been placed at the base of the probe. The convergences of four types of Green's function are shown in Figures 6, 7, 8, and 9. The convergence has been accelerated significantly when the asymptotic extraction is applied in computing the summation between the source and field points that are located in the same layer and different layers.

The input impedance of the spherical microstrip antenna has been calculated compared with that cited in [13] as shown in Figure 10. The summation of G_φ has been truncated

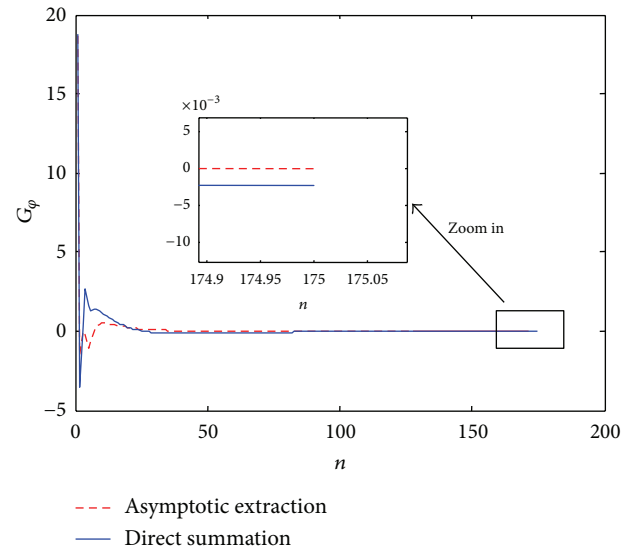

FIGURE 9: Convergence of G_φ^{22} when source and field points are located in the same triangle at the probe.

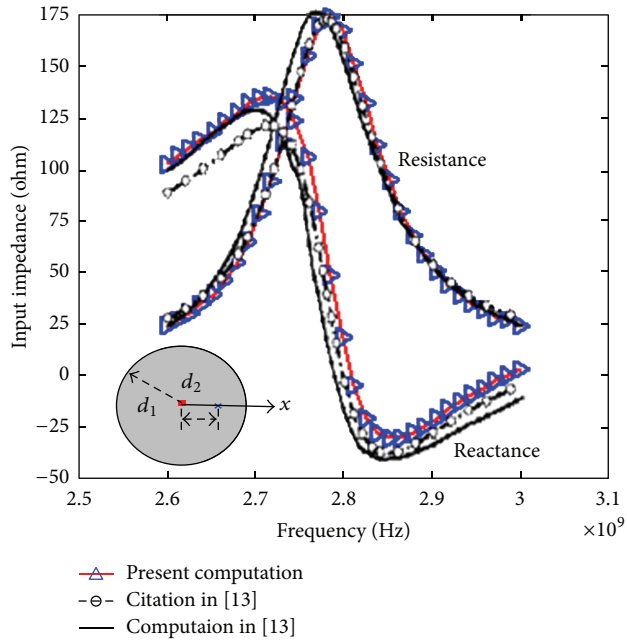

FIGURE 10: The comparison between the calculated result in this paper and the one of reference [13].

using 40 terms, which improves the computation efficiency significantly.

4. Conclusions

The input impedance of a three-layered spherical microstrip antenna has been calculated based on RWG triangular basis functions using mixed potential integral equation (MPIE). Asymptotic extraction approach is presented to accelerate the Green's functions convergence speed when source and

field points are located in the same layer and different layers. A novel division fashion of pair of triangles is adopted to simplify impedance matrix element calculation at the junction of the probe and patch.

Appendix

When the source is located in the free space and the field is located in the medium, the asymptotic dyadic Green's functions of the $\overline{\mathbf{G}}_{es}^{(21)}(\mathbf{r},\mathbf{r}')$ are given as

$$\begin{aligned}\overline{\mathbf{G}}_{es}^{21}|_a &= \nabla\nabla' G_1 \\ &= \frac{j}{4\pi k_2}\nabla\nabla'\sum_{n=0}^{\infty}(2n+1)\,P_n(\cos\gamma) \\ &\quad\times\left\{w_1\frac{a_2}{r}\,j_n\left(k_1\frac{a_2^2}{r}\right)h_n^{(2)}(k_1r') \right. \\ &\quad\left. +w_2\,j_n(k_1r)\,h_n^{(2)}(k_1r')\right\},\end{aligned} \tag{A.1}$$

$$\begin{aligned}\overline{\mathbf{G}}_{es}^{21}|_a &= \nabla\nabla' G_2 \\ &= \frac{j}{4\pi k_2 k_1}\nabla\nabla'\left(w_1\frac{a_2}{r}\frac{e^{-jk_2R_1}}{R_1}+w_2\frac{e^{-jk_2R_2}}{R_2}\right),\end{aligned}$$

where

$$\begin{aligned}w_1 &= \frac{((\varepsilon_2-\varepsilon_3)/(\varepsilon_2+\varepsilon_3))\left(((\varepsilon_1-\varepsilon_2)/(\varepsilon_1+\varepsilon_2))^2-1\right)}{2\sqrt{\varepsilon_1\varepsilon_2}/(\varepsilon_1+\varepsilon_2)}, \\ w_2 &= \frac{\left[1-((\varepsilon_1-\varepsilon_2)/(\varepsilon_1+\varepsilon_2))^2\right]}{2\sqrt{\varepsilon_1\varepsilon_2}/(\varepsilon_1+\varepsilon_2)}, \\ R_1 &= \sqrt{r'^2+\left(\frac{a_2^2}{r}\right)^2-2r'\left(\frac{a_2^2}{r}\right)\cos\gamma}, \\ R_2 &= \sqrt{r'^2+r^2-2r'r\cos\gamma}.\end{aligned} \tag{A.2}$$

When the source is located in the medium and the field is located in free space, the asymptotic dyadic Green's functions of the $\overline{\mathbf{G}}_{es}^{(12)}(\mathbf{r},\mathbf{r}')$ are given as

$$\begin{aligned}\overline{\mathbf{G}}_{es}^{12}|_a &= \nabla\nabla' G_1 = \frac{j}{4\pi k_1}\nabla\nabla'\sum_{n=0}^{\infty}(2n+1)\,P_n(\cos\gamma) \\ &\quad\times\left\{w_1 h_n^{(2)}(k_2r)\,j_n(k_2r')\right. \\ &\quad\left. +w_2\left(\frac{a_2}{r}\right)j_n\left(k_2\frac{a_2^2}{r}\right)h_n^{(2)}(k_2r')\right\},\end{aligned}$$

$$\overline{\mathbf{G}}_{es}^{12}|_a = \nabla\nabla' G_2 = \frac{j}{4\pi k_1 k_2}\nabla\nabla'\left(w_1\frac{e^{-jk_2R_1}}{R_1}+w_2\frac{a_2}{r}\frac{e^{-jk_2R_2}}{R_2}\right), \tag{A.3}$$

where

$$\begin{aligned}w_1 &= \frac{2\sqrt{\varepsilon_1\varepsilon_2}}{\varepsilon_1+\varepsilon_2}, \qquad w_2 = -\frac{2\sqrt{\varepsilon_1\varepsilon_2}}{\varepsilon_1+\varepsilon_2}\frac{\varepsilon_2-\varepsilon_3}{\varepsilon_2+\varepsilon_3}, \\ R_1 &= \sqrt{r'^2+r^2-2r'r\cos\gamma}, \\ R_2 &= \sqrt{r'^2+\left(\frac{a_2^2}{r}\right)^2-2r'\left(\frac{a_2^2}{r}\right)\cos\gamma}.\end{aligned} \tag{A.4}$$

When the source and fields is located in the medium, the asymptotic dyadic Green's functions of the $\overline{\mathbf{G}}_{es}^{(22)}(\mathbf{r},\mathbf{r}')$ are given as

$$\begin{aligned}\overline{\mathbf{G}}_{es}^{22}|_a &= \nabla\nabla' G_1 = \frac{j}{4\pi k_2}\nabla\nabla'\sum_{n=0}^{\infty}(2n+1), \\ P_n(\cos\gamma)&\times\left\{w_1\frac{a_2}{r}\times j_n\left(k_2\frac{a_2^2}{r}\right)h_n^{(2)}(k_2r')\right. \\ &\left. +\,w_2\frac{a_1}{r}\times h_n^{(2)}\left(k_2\frac{a_1^2}{r}\right)j_n(k_2r')\right\},\end{aligned} \tag{A.5}$$

$$\begin{aligned}\overline{\mathbf{G}}_{es}^{22}|_a &= \nabla\nabla' G_2 \\ &= \frac{j}{4\pi k_2^2}\nabla\nabla'\left(w_1\frac{a_2}{r}\frac{e^{-jk_2R_1}}{R_1}+w_2\frac{a_1}{r}\frac{e^{-jk_2R_2}}{R_2}\right),\end{aligned}$$

where

$$\begin{aligned}w_1 &= -\frac{\varepsilon_2-\varepsilon_3}{\varepsilon_2+\varepsilon_3}, \qquad w_2 = \frac{\varepsilon_1-\varepsilon_2}{\varepsilon_1+\varepsilon_2}, \\ R_1 &= \sqrt{r'^2+\left(\frac{a_2^2}{r}\right)^2-2r'\left(\frac{a_2^2}{r}\right)\cos\gamma}, \\ R_2 &= \sqrt{r'^2+\left(\frac{a_2^2}{r}\right)^2-2r'\left(\frac{a_2^2}{r}\right)\cos\gamma}.\end{aligned} \tag{A.6}$$

References

[1] C. Y. Yin and M. Z. Hu, "An efficient analysis method for cylindrical ormal microstrip antenna fed by microstripline," *International Journal of Antennas and Propagation*, vol. 2012, Article ID 629748, 8 pages, 2012.

[2] K.-M. Luk and W.-Y. Tam, "Patch antennas on a spherical body," *IEE Proceedings H*, vol. 138, no. 1, pp. 103–108, 1991.

[3] R. Shavit, "Circular polarization microstrip antenna on a conical surface," *IEEE Transactions on Antennas and Propagation*, vol. 45, no. 7, pp. 1086–1092, 1997.

[4] B. Ke and A. A. Kishk, "Analysis of spherical circular microstrip antennas," *IEE Proceedings H: Microwaves, Antennas and Propagation*, vol. 138, no. 6, pp. 542–548, 1991.

[5] A. A. Kishk, "Analysis of spherical annular microstrip antennas," *IEEE Transactions on Antennas and Propagation*, vol. 41, no. 3, pp. 338–343, 1993.

[6] A. C. de Castro Lima, J. R. Descardeci, and A. J. Giarola, "Circular microstrip antenna on a spherical surface," *Microwave and Optical Technology Letters*, vol. 5, no. 5, pp. 221–224, 1992.

[7] H.-T. Chen and Y.-T. Cheng, "Full-wave analysis of the annular-ring loaded spherical-circular microstrip antenna," *IEEE Transactions on Antennas and Propagation*, vol. 45, no. 11, pp. 1581–1583, 1997.

[8] Z. D. Dai and S. Lu, *Dyadic Green's Functions in Electromagnetic Theory*, Wuhan University Press, Wuhan, China, 2005.

[9] L.-W. Li, P.-S. Kooi, M.-S. Leong, and T.-S. Yeo, "Electromagnetic dyadic Green's function in spherically multilayered media," *IEEE Transactions on Microwave Theory and Techniques*, vol. 42, no. 12, pp. 2302–2310, 1994.

[10] S. K. Khamas, "Moment method analysis of an Archimedean spiral printed on a layered dielectric sphere," *IEEE Transactions on Antennas and Propagation*, vol. 56, no. 2, pp. 345–352, 2008.

[11] Z. Šipuš, P.-S. Kildal, R. Leijon, and M. Johansson, "An algorithm for calculating Green's functions of planar, circular cylindrical, and spherical multilayer substrates," *Applied Computational Electromagnetics Society Journal*, vol. 13, no. 3, pp. 243–254, 1998.

[12] Z. Sipus, S. Skokic, M. Bosiljevac, and N. Burum, "Study of mutual coupling between circular stacked-patch antennas on a sphere," *IEEE Transactions on Antennas and Propagation*, vol. 56, no. 7, pp. 1834–1844, 2008.

[13] S. K. Khamas, "Electromagnetic radiation by antennas of arbitrary shape in a layered spherical media," *IEEE Transactions on Antennas and Propagation*, vol. 57, no. 12, pp. 3827–3834, 2009.

[14] S. K. Khamas, "Asymptotic extraction approach for antennas in a multilayered spherical media," *IEEE Transactions on Antennas and Propagation*, vol. 58, no. 3, pp. 1003–1008, 2010.

[15] S. K. Khamas, "A generalized asymptotic extraction solution for antennas in multilayered spherical media," *IEEE Transactions on Antennas and Propagation*, vol. 58, no. 11, pp. 3743–3747, 2010.

[16] M. N. M. Yasin and S. K. Khamas, "Measurements and analysis of a probe-fed circularly polarized loop antenna printed on a layered dielectric sphere," *IEEE Transactions on Antennas and Propagation*, vol. 60, no. 4, pp. 2096–2100, 2012.

[17] K. A. Michalski and D. Zheng, "Electromagnetic scattering and radiation by surfaces of arbitrary shape in layered media—II: implementation and results for contiguous half-spaces," *IEEE Transactions on Antennas and Propagation*, vol. 38, no. 3, pp. 345–352, 1990.

Hindawi Publishing Corporation
International Journal of Antennas and Propagation
Volume 2013, Article ID 546260, 7 pages
http://dx.doi.org/10.1155/2013/546260

Research Article

Secrecy Balancing over Two-User MISO Interference Channels with Rician Fading

Jiqing Ni, Zesong Fei, Chengwen Xing, Di Zhao, Niwei Wang, and Jingming Kuang

School of Information and Electronics, Beijing Institute of Technology, Beijing 100081, China

Correspondence should be addressed to Zesong Fei; feizesong@bit.edu.cn

Received 11 January 2013; Accepted 8 July 2013

Academic Editor: Cheng-Xiang Wang

This paper considers a 2-user multiple-input single-output (MISO) interference channel with confidential messages (IFC-CM), in which the Rician channel model is assumed. The coordinated beamforming vectors at the two transmitters have the similar parameterizations as those for perfect CSI, which could be optimized jointly and achieved by agreeing on the real parameters between the two users. Our main contribution is that a quadratic relationship between the two real-valued parameters can be derived for the Rician channel to reach the ergodic secrecy rate balancing point. Simulation results present the secrecy performance over the 2-user MISO IFC-CM scenario.

1. Introduction

Security can be provided in the physical layer instead of using passwords or keys, where signal processing techniques can be adopted to degrade an eavesdropper's channel so that meaningful detection at the eavesdropper is difficult or even impossible. Information-theoretic security, widely known as physical-layer security, was first introduced in the 1970s by Wyner [1]. In particular, the notion of secrecy capacity, which is the maximum achievable rate that can be kept confidential to the eavesdropper, was defined. Later, the work was extended to the Gaussian wiretap channel in [2]. In [3], Csiszar and Korner considered a more general wiretap channel model and showed that secure communication is in fact possible without using key encryption in the presence of the eavesdropper. Recently, the advances in multiple-input multiple-output (MIMO), multicell communication and relay offer new opportunities for physical-layer security.

For MIMO wiretap channel, [4] studied the performance tradeoffs and derived upper and lower bounds on the secrecy capacity both for finite systems and in the large-system limit. Using artificial noise to confuse the eavesdropper, masked MIMO beamforming has also been considered in multicast system [5, 6]. For cooperative communication employing relays, [7] established the utility of user cooperation in facilitating secure communication and derived an outer-bound on the optimal rate-equivocation region based on a four-terminal relay-eavesdropper channel. In [8], the optimization of cooperative jamming (CJ) is examined to enhance the physical-layer security of a wiretap fading channel via distributed relays. Also, He and Yener in [9] provided an achievable secrecy rate region for the general channel with an untrusted relay. Most recently, physical layer secrecy has been also applied to other communication systems, such as two-way relay [10], satellite communications [11], and interference channel with confidential messages (IFC-CM) [12].

In [12], the achievable secrecy rate region and an outer bound for the IFC-CM were presented, while [13] derived the inner and outer bounds of a one-sided IFC-CM and analyzed the gap between them. A K-user Gaussian IFC with secrecy constraints was investigated in [14] and by using an interference alignment scheme with secrecy precoding at each transmitter, and it was revealed that a nonzero secure degree of freedom can be achieved. The scenario was extended to the K-user Gaussian many-to-one IFC in [15] where the achievable secrecy sum-rate over all users was shown to be achievable by using nested lattice codes.

From the signal-processing perspective, secure (or secret) communications has also received much attention. Literature [16] has studied the power control problem and artificial noise parameter optimization for the max-min point and the single-user point over the two-user symmetric IFC-CM

without multiple antennas. For the two-user MISO IFC-CM, [17] analyzed the key points on the Pareto boundary of the secrecy rate region for the two-user IFC with multiple-input single-output (MISO) antennas. Also, the multiple-input multiple-output (MIMO) Gaussian IFC-CM was investigated in [18] where a game-theoretic approach was proposed to permit the two transmitters to compromise to an operating point that better balances the network performance.

The focus of this paper is on a two-user interference channel with confidential messages (IFC-CM) in which each receiver is to decode its own message but could eavesdrop the message intended for the other user, where the imperfect CSI with Rician fading is assumed. First, the beamforming vectors corresponding to the Pareto-optimal ergodic secrecy rate points are characterized similar to the perfect CSI case. The coordinated optimal beamforming vectors at the two transmitters could be achieved by agreeing on the real parameters between the two users. Further, a quadratic relationship between the two real valued parameters can be derived, and the ergodic secrecy-rate balancing point which provides a secrecy rate-fair operating point will be determined by searching only one real-valued parameter.

The remainder of this paper is organized as follows. In Section 2, we present the system model. In Section 3, the Pareto boundary of the secrecy rate region is characterized, and some special operating points are considered. Section 4 extends the work to the statistical CSI, and the closed-form ergodic secrecy rate expressions are derived. Section 5 presents simulation results, and conclusions are drawn in Section 6 finally.

Notations. Throughout, vectors are denoted by boldface small letters while matrices are written in boldface capital letters. We use the superscripts $(\cdot)^*$, $(\cdot)^T$, and $(\cdot)^H$ to denote, respectively, the complex conjugate, transpose and Hermitian transpose operations. An identity matrix is denoted by $\mathbf{I}$.

2. MISO IFC-CM Model

We consider a two-user MISO IFC-CM, which may arise from a downlink cellular network with two multiantenna base stations (BSs) each transmitting to one desirable mobile station (MS). The message sent by each BS is confidential and required to be kept confidential to the other unintended MS. Due to the broadcast nature of wireless channels, however, the MSs may eavesdrop on the transmitted signals not intended for them and thus be regarded as eavesdroppers to each other, as is shown in Figure 1. Note that the two BSs trust each other so that they could design the coordinated beamformers together to optimize the secrecy rates. The MS receivers are assumed to have a single antenna, and each BS is equipped with N transmit antennas.

Based on the model, the received signals at the two MSs can be written as

$$y_1 = \mathbf{h}_{11}^T \mathbf{w}_1 s_1 + \mathbf{h}_{21}^T \mathbf{w}_2 s_2 + n_1,$$
$$y_2 = \mathbf{h}_{22}^T \mathbf{w}_2 s_2 + \mathbf{h}_{12}^T \mathbf{w}_1 s_1 + n_2, \quad (1)$$

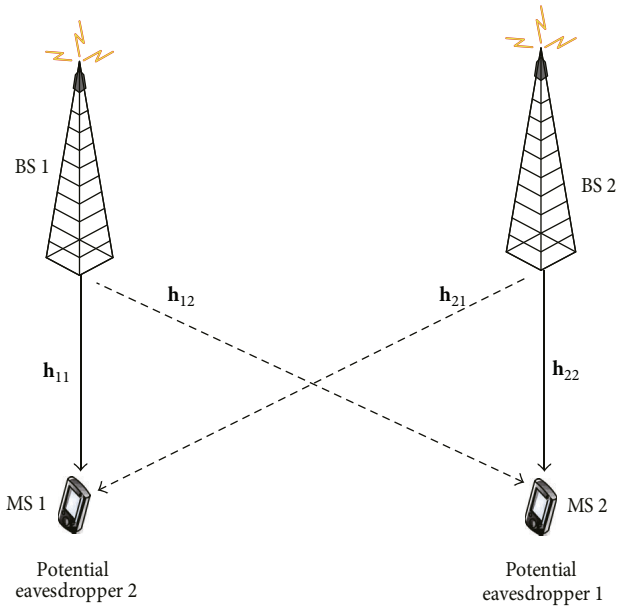

Figure 1: Coordinated beamforming with two BSs and two untrusted MSs.

where $\mathbf{h}_{ij} \in \mathbb{C}^{N\times 1}$ $(i, j = 1, 2)$ denotes the complex channel vector between BS i and MS j, s_i denotes the information symbol intended for MS i sent by BS i, n_i is the complex Gaussian noise with zero mean and variance σ^2, and $\mathbf{w}_i$ denotes the transmit beamforming vector at the ith BS and, without loss of generality, satisfies the peak power constraint $\|\mathbf{w}_i\| \leq 1$. The noises and the channels are all independent to each other.

The received signal at each MS contains the desirable message and also the message intended for the other MS, and the channel can therefore be viewed as a virtual multiple-access channel (MAC) with the achievable rate already known in [19], which is given in the following lemma for completeness.

Lemma 1 (capacity for MAC [19]). *For a K-user MAC with channels $\{\mathbf{h}_k\}$ and transmit covariance matrices $\{\mathbf{\Sigma}_k\}$, for $k = 1, \ldots, K$, joint decoding with successive interference cancelation can achieve all the corner points of the capacity region. Given a decoding order $(\pi(1), \pi(2), \ldots, \pi(K))$ in which user $\pi(1)$ is decoded first, user $\pi(2)$ is decoded second, and so on, the achievable rate for user k is given by*

$$R_{\pi(k)} = \log_2 \left(1 + \frac{\mathbf{h}_{\pi(k)}^H \mathbf{\Sigma}_{\pi(k)} \mathbf{h}_{\pi(k)}}{\sigma^2 + \sum_{l=k+1}^{K} \mathbf{h}_{\pi(l)}^H \mathbf{\Sigma}_{\pi(l)} \mathbf{h}_{\pi(l)}} \right). \quad (2)$$

Lemma 1 states that the decoding order has no impact on the channel sum-rate but determines the achievable rate for each user. Specifically, the decoding order for the intended message and the eavesdropped message determines the message rate and the equivocation rate. We assume that the intended message is decoded first by treating the eavesdropped message as noise, and then the eavesdropped

message is decoded without any interference. Then, the eavesdropped signals at the MSs can be equivalently expressed as

$$y_{e1} = \mathbf{h}_{12}^T \mathbf{w}_1 s_1 + n_2,$$
$$y_{e2} = \mathbf{h}_{21}^T \mathbf{w}_2 s_2 + n_1. \tag{3}$$

The level of secrecy can be quantified by *secrecy rate* which is given by [3]

$$R_s = R_d - R_e, \tag{4}$$

where R_d denotes the message rate and R_e denotes the equivocation rate. With the intended message being decoded first, the secrecy rates for MS 1 and MS 2 can be, respectively, written as

$$R_{s1} = \log_2\left(1 + \frac{\left|\mathbf{h}_{11}^T \mathbf{w}_1\right|^2}{\sigma^2 + \left|\mathbf{h}_{21}^T \mathbf{w}_2\right|^2}\right) - \log_2\left(1 + \frac{\left|\mathbf{h}_{12}^T \mathbf{w}_1\right|^2}{\sigma^2}\right),$$
$$R_{s2} = \log_2\left(1 + \frac{\left|\mathbf{h}_{22}^T \mathbf{w}_2\right|^2}{\sigma^2 + \left|\mathbf{h}_{12}^T \mathbf{w}_1\right|^2}\right) - \log_2\left(1 + \frac{\left|\mathbf{h}_{21}^T \mathbf{w}_2\right|^2}{\sigma^2}\right). \tag{5}$$

Based on the decoding order, the smallest R_d and the largest R_e are obtained at the MS receivers, and the achievable secrecy rates in (5) correspond to the inner bound for the secrecy rates over the general Gaussian MISO IFC-CM [12], which provides a worst-case scenario for analysis and optimization of the beamforming vectors. A similar argument has been used in [18] to justify their formulation.

We can define the *achievable secrecy rate region* to be the set of all secrecy rate pairs where the MISO beamforming vectors satisfy the power constraints at the BSs:

$$\mathscr{R}_s \triangleq \bigcup_{(\mathbf{w}_1,\mathbf{w}_2):\|\mathbf{w}_1\|,\|\mathbf{w}_2\|\le 1} (R_{s1}, R_{s2}). \tag{6}$$

The outer boundary of this region is called the *Pareto boundary*, because it consists of the operating points (R_{s1}, R_{s2}) for which it is impossible to improve one secrecy rate, without simultaneously decreasing the other secrecy rate. More precisely, we define the Pareto optimality of an operating point as follows.

Definition 2. A secrecy rate tuple (R_{s1}, R_{s2}) is Pareto optimal if there is no other tuple $(\widetilde{R}_{s1}, \widetilde{R}_{s2})$ such that $(\widetilde{R}_{s1}, \widetilde{R}_{s2}) \ge (R_{s1}, R_{s2})$ and $(\widetilde{R}_{s1}, \widetilde{R}_{s2}) \ne (R_{s1}, R_{s2})$ where the inequality operates component wisely.

It is noted that for a fixed channel, the secrecy rate region $\mathscr{R}_s$ is compact because the set $(\mathbf{w}_1, \mathbf{w}_2)$ subject to the power constraint is compact and the mapping from $(\mathbf{w}_1, \mathbf{w}_2)$ to (R_{s1}, R_{s2}) is continuous.

3. Ergodic Secrecy Rate Region with Rician Channel

3.1. Rician Channel Model. We consider that the channel vectors follow the Rician channel model, that is,

$$\mathbf{h}_{ij} = \overline{\mathbf{h}}_{ij} + \sqrt{\alpha}\Delta\mathbf{h}_{ij}, \tag{7}$$

where $\overline{\mathbf{h}}_{ij}$ is channel mean vector, $\Delta\mathbf{h}_{ij} \in \mathscr{CN}(0, I)$ denotes channel error vector and its entries are modelled as independent nonzero-mean random variables, α is the error coefficient and without losing generality, and α is assumed to be same for all the channels.

3.2. Ergodic Secrecy Rate Region. The ergodic secrecy rates are obtained by taking the expectation over the distribution of the channels, that is,

$$\overline{R}_{s1} = \mathbb{E}_{\mathbf{h}_{11},\mathbf{h}_{12},\mathbf{h}_{21}}\left[R_{s1} \mid \mathbf{h}_{11}, \mathbf{h}_{12}, \mathbf{h}_{21}\right],$$
$$\overline{R}_{s2} = \mathbb{E}_{\mathbf{h}_{22},\mathbf{h}_{21},\mathbf{h}_{12}}\left[R_{s2} \mid \mathbf{h}_{22}, \mathbf{h}_{21}, \mathbf{h}_{12}\right]. \tag{8}$$

The achievable ergodic secrecy rate region can be expressed as the set of all the ergodic secrecy rates:

$$\overline{\mathscr{R}}_s \triangleq \bigcup_{(\mathbf{w}_1,\mathbf{w}_2):\|\mathbf{w}_1\|,\|\mathbf{w}_2\|\le 1} \left(\overline{R}_{s1}, \overline{R}_{s2}\right). \tag{9}$$

Consider $\overline{R}_{s1}$ first, and it has

$$\begin{aligned}\overline{R}_{s1} = {} & \mathbb{E}_{\mathbf{h}_{11},\mathbf{h}_{21}}\left[\log_2\left(1 + \left|\mathbf{h}_{11}^T \mathbf{w}_1\right|^2 + \left|\mathbf{h}_{21}^T \mathbf{w}_2\right|^2\right)\right] \\ & - \mathbb{E}_{\mathbf{h}_{21}}\left[\log_2\left(1 + \left|\mathbf{h}_{21}^T \mathbf{w}_2\right|^2\right)\right] \\ & - \mathbb{E}_{\mathbf{h}_{12}}\left[\log_2\left(1 + \left|\mathbf{h}_{12}^T \mathbf{w}_1\right|^2\right)\right],\end{aligned} \tag{10}$$

where the second and third terms could be tackled using [20]

$$\begin{aligned}&\mathbb{E}_{\mathbf{h}}\left[\log_2\left(1 + \left|\mathbf{h}^T \mathbf{w}\right|^2\right)\right] \\ &= \int_0^\infty \frac{e^{-t}}{t} \times \left(1 - \frac{1}{1+tp} \exp\left(-\frac{\alpha\left|\overline{\mathbf{h}}^T \mathbf{w}\right|^2 t}{1+t}\right)\right) dt,\end{aligned} \tag{11}$$

which involves a single integral which can be effectively calculated by using high-precision numerical integral methods [21]. Also note that it is monotonic increasing with $|\overline{\mathbf{h}}^T \mathbf{w}|^2$. While for the first term, it is more difficult to reexpress it with simpler expression, but we know that $|\mathbf{h}_{11}^T \mathbf{w}_1|^2 + |\mathbf{h}_{21}^T \mathbf{w}_2|^2$ belongs to noncentral chi-squared distribution, that is, the sum of the squares of independent Gaussian random variables having unit variance and nonzero means [22], the expectation is monotonic increasing with each mean. Although we do not present the closed form of the ergodic secrecy rate, but the monotony is very useful for us to further characterize the achievable ergodic secrecy rate region. $\overline{R}_{s2}$ has similar monotony.

3.3. Characterization of Ergodic Secrecy Rate Region. It shows that any point on the Pareto boundary should be achieved with full power and the corresponding beamforming vectors have the same characterization as perfect CSI case. To proceed, we first state the following lemma, which deals with the monotony of $\overline{R}_s$. The lemma is stated for $\overline{R}_{s1}$; similar results hold for $\overline{R}_{s2}$.

Lemma 3. *$\overline{R}_{s1}$ is monotonic increasing with $|\overline{\mathbf{h}}_{11}^T\mathbf{w}_1|$ and monotonic decreasing with $|\overline{\mathbf{h}}_{21}^T\mathbf{w}_2|$ and $|\overline{\mathbf{h}}_{12}^T\mathbf{w}_1|$.*

Proof. From discussions in the previous subsection, we know that $\mathbb{E}_{\mathbf{h}_{12}}[\log_2(1+|\mathbf{h}_{12}^T\mathbf{w}_1|^2)]$ is monotonic increasing with $|\overline{\mathbf{h}}_{12}^T\mathbf{w}_1|$, and $\mathbb{E}_{\mathbf{h}_{11},\mathbf{h}_{21}}[\log_2(1+|\mathbf{h}_{11}^T\mathbf{w}_1|^2+|\mathbf{h}_{21}^T\mathbf{w}_2|^2)]$ is monotonic increasing with $|\overline{\mathbf{h}}_{11}^T\mathbf{w}_1|$ and $|\overline{\mathbf{h}}_{21}^T\mathbf{w}_2|$. Thus, it is easy to see $\overline{R}_{s1}$ is monotonic increasing with $|\overline{\mathbf{h}}_{11}^T\mathbf{w}_1|$ and decreasing with $|\overline{\mathbf{h}}_{12}^T\mathbf{w}_1|$.

Next we consider the term $|\overline{\mathbf{h}}_{21}^T\mathbf{w}_2|$, which is included in both the first term and second term in (10). We will show it using the method that for fixed $|\mathbf{h}_{11}^T\mathbf{w}_1|>0$, it has that $\overline{R}_{s1}$ is monotonic decreasing with $|\overline{\mathbf{h}}_{21}^T\mathbf{w}_2|$. Further for any positive random variable $|\mathbf{h}_{11}^T\mathbf{w}_1|>0$, the monotony still holds, that is, the term

$$\begin{aligned}&\mathbb{E}_{\mathbf{h}_{21}}\left[\log_2\left(1+\left|\mathbf{h}_{11}^T\mathbf{w}_1\right|^2+\left|\mathbf{h}_{21}^T\mathbf{w}_2\right|^2\right)\right]\\&-\mathbb{E}_{\mathbf{h}_{21}}\left[\log_2\left(1+\left|\mathbf{h}_{21}^T\mathbf{w}_2\right|^2\right)\right]\end{aligned}\tag{12}$$

is monotonic decreasing with $|\overline{\mathbf{h}}_{21}^T\mathbf{w}_2|$. Note that since the expectation over $|\mathbf{h}_{11}^T\mathbf{w}_1|$ does not affect the monotony of this term. Thus, we have that $\overline{R}_{s1}$ is monotonic decreasing with $|\overline{\mathbf{h}}_{21}^T\mathbf{w}_2|$, which completes the proof. □

From the monotonicity of $\overline{R}_{s1}$, we see that the same conflicting situation happens as the perfect CSI case associated with the beamforming vectors. By utilizing the similar method, any beamforming vector leading to a Pareto-optimal ergodic secrecy rate tuple can be expressed as a linear combination of stochastic maximal-ratio combining (MRC) and stochastic zero-forcing (ZF) beamformers, which are defined as

$$\begin{aligned}\overline{\mathbf{w}}_1^{\mathrm{MRC}}&=\frac{\overline{\mathbf{h}}_{11}^*}{\|\overline{\mathbf{h}}_{11}\|},\qquad \overline{\mathbf{w}}_2^{\mathrm{MRC}}=\frac{\overline{\mathbf{h}}_{22}^*}{\|\overline{\mathbf{h}}_{22}\|},\\ \overline{\mathbf{w}}_1^{\mathrm{ZF}}&=\frac{\Pi_{\overline{\mathbf{h}}_{12}^*}^{\perp}\overline{\mathbf{h}}_{12}^*}{\|\Pi_{\overline{\mathbf{h}}_{12}^*}^{\perp}\overline{\mathbf{h}}_{12}\|},\qquad \overline{\mathbf{w}}_2^{\mathrm{ZF}}=\frac{\Pi_{\overline{\mathbf{h}}_{21}^*}^{\perp}\overline{\mathbf{h}}_{21}^*}{\|\Pi_{\overline{\mathbf{h}}_{21}^*}^{\perp}\overline{\mathbf{h}}_{21}\|}.\end{aligned}\tag{13}$$

Theorem 4. *Any Pareto-optimal ergodic secrecy rate point is achievable with the beamforming strategy:*

$$\mathbf{w}_1=\frac{\lambda_1\overline{\mathbf{w}}_1^{MRC}+(1-\lambda_1)\overline{\mathbf{w}}_1^{ZF}}{\left\|\lambda_1\overline{\mathbf{w}}_1^{MRC}+(1-\lambda_1)\overline{\mathbf{w}}_1^{ZF}\right\|},\tag{14a}$$

$$\mathbf{w}_2=\frac{\lambda_2\overline{\mathbf{w}}_2^{MRC}+(1-\lambda_2)\overline{\mathbf{w}}_2^{ZF}}{\left\|\lambda_2\overline{\mathbf{w}}_2^{MRC}+(1-\lambda_2)\overline{\mathbf{w}}_2^{ZF}\right\|},\tag{14b}$$

where $0\le\lambda_1,\ \lambda_2\le 1$ are real-valued parameters.

Proof. The proof is essentially the same as that of its perfect CSI case. Hence, we only provide an outline here. The proof uses the method of contradiction.

To do so, we write any optimal beamforming vector as

$$\mathbf{w}_1'\triangleq\mathbf{w}_1+\mathbf{u}_1,\tag{15}$$

where $\mathbf{w}_1\in\mathrm{span}\{\overline{\mathbf{h}}_{11}^*,\overline{\mathbf{h}}_{12}^*\}$ and choosing $\mathbf{u}_1$ in the nullspace of $\mathrm{span}\{\overline{\mathbf{h}}_{11}^*,\overline{\mathbf{h}}_{12}^*\}$ such that $\|\mathbf{w}_1'\|=1$. Clearly, $\mathbf{w}_1'$ achieves the same secrecy rate performance as $\mathbf{w}_1$. Hence, the optimal beamforming vector should lie in the space spanned by $\overline{\mathbf{h}}_{11}^*$ and $\overline{\mathbf{h}}_{12}^*$.

Next, we prove that the Pareto-optimal ergodic secrecy rate point can be obtained only when full power is used. To show this, we first consider $\overline{R}_{s1}$ and assume $\|\mathbf{w}_1\|<1$. Construct $\mathbf{w}_1''=\mathbf{w}_1+\mathbf{v}_1$ such that $\|\mathbf{w}_1''\|=1$. Based on the monotony of the associated terms, it can prove that if $\|\mathbf{w}_i\|<1$, then it is possible to choose a new $\|\mathbf{w}_i''\|=1$, such that $\overline{R}_{s1}$ is increased and $\overline{R}_{s2}$ is unchanged. Therefore, in order to reach the Pareto boundary, the transmitter should operate at full power. And any optimal beamformer in the space of $\mathrm{span}\{\overline{\mathbf{h}}_{11}^*,\overline{\mathbf{h}}_{12}^*\}$ could be formulated as the form in (14a). See [23] for more details regarding the proof. □

It is worth highlighting that previous Theorem 4 aligns with the result for the two-user MISO IFC-CM with perfect CSI [23]; this is because that they have the similar monotony with the terms associated with beamformers. This theorem also shows that we only need to vary the scalar real-valued parameters λ_1 and λ_2 in order to achieve any specific point on the Pareto boundary of the ergodic secrecy rate region. That is, these two BSs could achieve this specific points by setting λ_1 and λ_2 together.

4. Ergodic Secrecy Rate Balancing Point

4.1. Ergodic Secrecy Balancing. In the IFC model, user fairness is an important metric which can be achieved by balancing the user secrecy rates so that the weaker user is not overly compromised. Technically, this can be obtained by maximizing the worse-user's secrecy rate. That is,

$$\max\ \min\left\{\overline{R}_{s1},\overline{R}_{s2}\right\}.\tag{16}$$

The secrecy rate balancing point can be realized by setting, if a solution exists,

$$\overline{R}_{s1}=\overline{R}_{s2},\tag{17}$$

which can be simplified as

$$\left|\overline{\mathbf{h}}_{11}^T\mathbf{w}_1\right|^2+\left|\overline{\mathbf{h}}_{21}^T\mathbf{w}_2\right|^2=\left|\overline{\mathbf{h}}_{22}^T\mathbf{w}_2\right|^2+\left|\overline{\mathbf{h}}_{12}^T\mathbf{w}_1\right|^2.\tag{18}$$

Then, a simple relationship between λ_1 and λ_2 can be achieved.

Proposition 5. *For any given* λ_2, (18) *could be transformed into a quadratic equation:*

$$a_2\lambda_1^2 + b_2\lambda_1 + c_2 = 0, \tag{19}$$

where the coefficients are specified as (25)–(28).

Proof. We first introduce the following terms [24]:

$$\begin{aligned} p_1(\lambda_1) &\triangleq \left|\overline{\mathbf{h}}_{11}^H \mathbf{w}_1(\lambda_1)\right|^2, \\ p_2(\lambda_2) &\triangleq \left|\overline{\mathbf{h}}_{22}^H \mathbf{w}_2(\lambda_2)\right|^2, \\ q_1(\lambda_2) &\triangleq \left|\overline{\mathbf{h}}_{21}^H \mathbf{w}_2(\lambda_2)\right|^2, \\ q_2(\lambda_1) &\triangleq \left|\overline{\mathbf{h}}_{12}^H \mathbf{w}_1(\lambda_1)\right|^2. \end{aligned} \tag{20}$$

Substituting $\mathbf{w}_1$ in (14a) into $p_1(\lambda_1)$ and $q_2(\lambda_1)$, we have

$$p_1(\lambda_1) = \left\|\overline{\mathbf{h}}_{11}\right\|^2 \frac{\left(\alpha_1\lambda_1 + (1-\alpha_1)\right)^2}{2\alpha_1\lambda_1^2 - 2\alpha_1\lambda_1 + 1}, \tag{21}$$

$$q_2(\lambda_1) = \frac{\beta_1^2\lambda_1^2}{2\alpha_1\lambda_1^2 - 2\alpha_1\lambda_1 + 1}, \tag{22}$$

where $\alpha_1 = 1 - (\|\Pi^{\perp}_{\overline{\mathbf{h}}_{12}} \overline{\mathbf{h}}_{11}\|/\|\overline{\mathbf{h}}_{11}\|)$ and $\beta_1 = |\overline{\mathbf{h}}_{12}^H \overline{\mathbf{h}}_{11}|/\|\overline{\mathbf{h}}_{11}\|$. The functions $p_2(\lambda_2), q_1(\lambda_2)$ can be expressed and defined in a similar way with parameters $\alpha_2 = 1 - (\|\Pi^{\perp}_{\overline{\mathbf{h}}_{21}} \overline{\mathbf{h}}_{22}\|/\|\overline{\mathbf{h}}_{22}\|)$ and $\beta_2 = |\overline{\mathbf{h}}_{21}^H \overline{\mathbf{h}}_{22}|/\|\overline{\mathbf{h}}_{22}\|$.

By substituting (20) into (18), we have

$$p_1(\lambda_1) - q_2(\lambda_1) = p_2(\lambda_2) - q_1(\lambda_2). \tag{23}$$

It can be easily seen that the left-hand-side (LHS) and the RHS of (23) are functions of only λ_1 and λ_2, respectively. Let the RHS of (23) be t_2. Then, we have

$$p_1(\lambda_1) - q_2(\lambda_1) = t_2. \tag{24}$$

Inserting (21) and (22) into (24) and simplifying the expression, we get the quadratic equation (19) with the coefficients as

$$a_2 = \alpha_1^2\left\|\overline{\mathbf{h}}_{11}\right\|^2 - \left(1+\sigma^2\right)\beta_1 - 2\alpha_1 t_2, \tag{25}$$

$$b_2 = 2(1-\alpha_1)\alpha_1\left\|\overline{\mathbf{h}}_{11}\right\|^2 + 2\alpha_1 t_2 + 2\alpha_1\beta_1\sigma^2, \tag{26}$$

$$c_2 = (1-\alpha_1)^2\left\|\overline{\mathbf{h}}_{11}\right\|^2 - t_2 + \beta_1\sigma^2, \tag{27}$$

$$t_2 = p_2(\lambda_2) - q_1(\lambda_2). \tag{28}$$

□

Next, we show by the method of contradiction that the secrecy rate balancing point corresponds to a unique solution in the feasible set if (19) is solvable. Assume that (19) has two solutions, λ_1 and λ_1', both corresponding to the secrecy balancing point, that is, $\overline{R}_{s1} = \overline{R}_{s2}(\lambda_1, \lambda_2) = \overline{R}_{s2}(\lambda_1', \lambda_2)$. However, from Lemma 3, $\overline{R}_{s2}(\lambda_1, \lambda_2)$ is a continuous monotonously decreasing function of λ_1 which means that for different λ_1 and λ_1', $\overline{R}_{s2}(\lambda_1, \lambda_2) \neq \overline{R}_{s2}(\lambda_1', \lambda_2)$. This contradicts the assumption which completes the proof.

For a given λ_1, λ_2 can be determined by solving a similar quadratic equation. Through Proposition 5, the secrecy rate balancing point can be determined by searching only one real-valued parameter in the feasible set. The secrecy rate balancing point achievable by $(\lambda_1^{\mathrm{SRB}}, \lambda_2^{\mathrm{SRB}})$ is the one that gives the maximal secrecy rate among all of the points that satisfy $\overline{R}_{s1} = \overline{R}_{s2}$. For the special case that there is no λ_1 satisfying the quadratic equation (19) for any λ_2 in the feasible set, it reduces to the single-user ergodic secrecy rate maximal point where the worse-user's secrecy rate is maximized. The single-user ergodic secrecy rate maximal point is where $\overline{R}_{s1}^{\max} < \overline{R}_{s2}^{\mathrm{ZF}}$ or $\overline{R}_{s2}^{\max} < \overline{R}_{s1}^{\mathrm{ZF}}$ is selected. Note that $\overline{R}_{s1}^{\max}$ denotes the maximal ergodic secrecy rate for $\overline{R}_{s1}$, and $\overline{R}_{s1}^{\mathrm{ZF}}$ corresponds to the case that the BS 1 chooses the stochastic ZF beamforming to minimize the interference for the other link.

4.2. Single-User Maximal Ergodic Secrecy Rate. At the single-user ergodic secrecy rate maximal point, one BS should choose the stochastic ZF beamforming strategy while the other BS tries to maximize the ergodic secrecy rate. In our two-user IFC-CM model, there are two single-user ergodic secrecy rate maximal points for $\overline{R}_{s1}$ and $\overline{R}_{s2}$, respectively. As the special case of secrecy balancing, the operating point is where $\overline{R}_{s1}^{\max} < \overline{R}_{s2}^{\mathrm{ZF}}$ or $\overline{R}_{s2}^{\max} < \overline{R}_{s1}^{\mathrm{ZF}}$ is selected.

$\overline{R}_{s1}$ can be formulated as a function of λ_1 with $\lambda_2 = 0$. In this case, there always exists an optimal λ_1, $\lambda_1^{\mathrm{SU-opt}}$, ensuring that $\overline{R}_{s1}(\lambda_1^{\mathrm{SU-opt}}) = \overline{R}_{s1}^{\max}$. The optimal $\lambda_1^{\mathrm{SU-opt}}$ can be easily obtained by searching over the feasible set $0 \leq \lambda_1 \leq 1$. Similarly, the single-user secrecy rate maximal point for $\overline{R}_{s2}$ can be derived by setting $\lambda_1 = 0$ and $\lambda_2 = \lambda_2^{\mathrm{SU-opt}}$. The single-user ergodic secrecy rate maximal points for $\overline{R}_{s1}$ and $\overline{R}_{s1}$ are endpoints on the Pareto boundary of the ergodic secrecy rate region. It can be also understood since there are no other operating points that could improve $\overline{R}_{s1}^{\max}$ or $\overline{R}_{s2}^{\max}$ further even sacrificing the other user's secrecy rate performance.

4.3. Other Key Points

4.3.1. Stochastic ZF. At this key point, both BSs choose the stochastic ZF beamformers, which can be achieved by simply setting $\lambda_1 = \lambda_2 = 0$. The secrecy ZF point is not on the Pareto boundary but in the interior of the ergodic secrecy rate region. Also, it is clear that at high SNR or for a large number of antennas, the secrecy ZF point will not be far away from the optimal point.

4.3.2. Nash Equilibrium. At the Nash equilibrium, the users (or BSs) selfishly optimize their beamforming vectors to maximize their own secrecy rates assuming that beamforming of

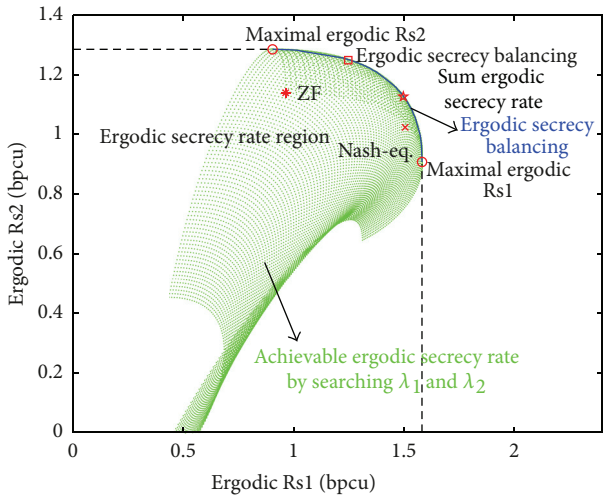

FIGURE 2: Ergodic secrecy rate region with 0 dB SNR for a random channel realization.

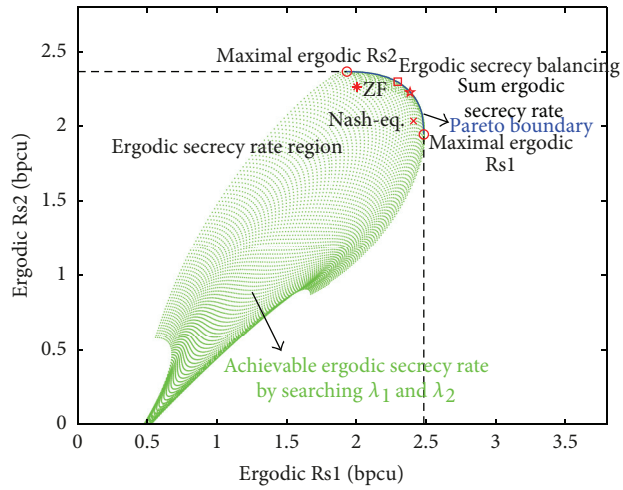

FIGURE 3: Ergodic secrecy rate region with 5 dB SNR for a random channel realization.

the other user is fixed [25]. We can iteratively search optimal λ_1 and λ_2 to reach the Nash-equilibrium point. This point is not optimal and thus in the interior of the ergodic secrecy rate region.

4.3.3. Sum Ergodic Secrecy Rate. The sum secrecy rate point is the point at which $\overline{R}_{s1} + \overline{R}_{s2}$ is maximized. Geometrically, this is where the Pareto boundary of the secrecy rate region, $\overline{\mathcal{R}}_s$, osculates a straight line with slope -1 [26]. It goes without saying that the sum secrecy rate point is on the Pareto boundary of $\overline{\mathcal{R}}_s$.

5. Simulation Results

Simulation results are provided to study the ergodic secrecy rate region for the two-user Gaussian MISO IFC-CM by the Pareto-boundary characterization for the cases with Rician channel. In the simulations, unless specified otherwise, we assume that the number of transmit antennas at each BS is 2 and the channel mean vector is randomly generated from an i.i.d. complex Gaussian distribution with zero mean and unit variance. Note that α is set as 0.1 in the all simulations.

Figure 2 shows an example of the ergodic secrecy rate region for a two-user Gaussian MISO IFC-CM over Rician fading with SNR at 0 dB. The achievable ergodic secrecy rate region generated from Theorem 4 by varying λ_1 and λ_2 in [0 1], and as we can see, the Pareto boundary including all the key operating points can be obtained through the parameterization. Also, the ergodic secrecy rate balancing point is on the Pareto boundary and it is where the Pareto boundary intersects the line $y = x$. In comparison, the sum secrecy rate point is the point where the Pareto boundary touches the straight line of slope -1. Results illustrate that the secrecy rate balancing point gives a lower sum secrecy rate compared to the sum secrecy rate point, but the worst-user secrecy rate is maximized. Also, the Nash-equilibrium point

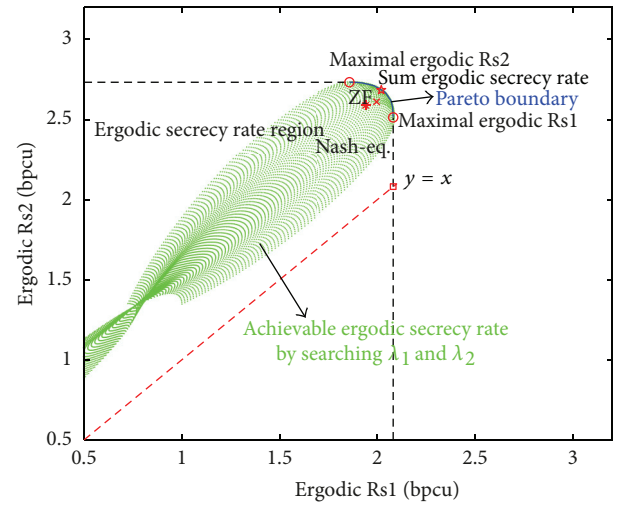

FIGURE 4: Ergodic secrecy rate region with 0 dB SNR for a random channel realization where the ergodic secrecy rate balancing point aligns with the single-user secrecy rate maximal point.

and the stochastic ZF point are in the interior of the secrecy rate region, that is, not Pareto optimal.

Figure 3 provides another example of the ergodic secrecy rate region but with SNR at 5 dB with same channel realization. As can be seen, when the SNR is increased, the corresponding ergodic secrecy rates are all improved and the stochastic ZF point in particular gets closer to the Pareto boundary.

Figure 4 considers the special case that the ergodic secrecy rate balancing point reduces to the single-user ergodic secrecy rate maximal point, which occurs when there is no solution to (18) for (λ_1, λ_2). Geometrically, the Pareto boundary of $\overline{\mathcal{R}}_s$ has no intersection point with the straight line $y = x$, which can be observed in the figure. Thus, the ergodic secrecy rate balancing point is reduced to the closest single-user ergodic secrecy rate maximal point.

6. Conclusion

In this paper, we studied the two-user MISO IFC-CM with Rician fading assumption. We revealed that the optimal beamforming vectors corresponding to the Pareto optimal point have the same parameterizations as those for perfect CSI. The secrecy rate balancing point, which provides the highest user fairness, was investigated. In particular, a quadratic relationship between the two real-valued parameters can be derived for the Rician channel to reach the ergodic secrecy rate balancing point. Simulation results show the secrecy performance of the proposed method.

Acknowledgments

This work was supported in part by China National S&T Major Project 2013ZX03003002-003, the National Natural Science Foundation of China under Grant no. 61101130, and the Excellent Young Scholar Research Funding of Beijing Institute of Technology under Grant no. 2013CX04038.

References

[1] A. D. Wyner, "Wire-tap channel," *Bell System Technical Journal*, vol. 54, no. 8, pp. 1355–1387, 1975.

[2] S. K. Leung-Yan-Cheong and M. E. Hellman, "Gaussian wiretap channel," *IEEE Transactions on Information Theory*, vol. IT-24, no. 4, pp. 451–456, 1978.

[3] I. Csiszar and J. Korner, "Broadcast channels with confidential messages," *IEEE Transactions on Information Theory*, vol. IT-24, no. 3, pp. 339–348, 1978.

[4] S. Goel and R. Negi, "Guaranteeing secrecy using artificial noise," *IEEE Transactions on Wireless Communications*, vol. 7, no. 6, pp. 2180–2189, 2008.

[5] M. Pei, J. Wei, K.-K. Wong, and X. Wang, "Masked beamforming for multiuser MIMO wiretap channels with imperfect CSI," *IEEE Transactions on Wireless Communications*, vol. 11, no. 2, pp. 544–549, 2012.

[6] A. Khisti and G. W. Wornell, "Secure transmission with multiple antennas I: the MISOME wiretap channel," *IEEE Transactions on Information Theory*, vol. 56, no. 7, pp. 3088–3104, 2010.

[7] L. Lai and H. El Gamal, "The relay-eavesdropper channel: cooperation for secrecy," *IEEE Transactions on Information Theory*, vol. 54, no. 9, pp. 4005–4019, 2008.

[8] G. Zheng, L.-C. Choo, and K.-K. Wong, "Optimal cooperative jamming to enhance physical layer security using relays," *IEEE Transactions on Signal Processing*, vol. 59, no. 3, pp. 1317–1322, 2011.

[9] X. He and A. Yener, "Cooperation with an untrusted relay: a secrecy perspective," *IEEE Transactions on Information Theory*, vol. 56, no. 8, pp. 3807–3827, 2010.

[10] H. Wang, Q. Yin, and X. Xia, "Distributed beamforming for physical-layer security of two-way relay networks," *IEEE Transactions on Signal Processing*, vol. 60, no. 7, pp. 3532–3545, 2012.

[11] G. Zheng, P.-D. Arapoglou, and B. Ottersten, "Physical layer security in multibeam satellite systems," *IEEE Transactions on Wireless Communications*, vol. 11, no. 2, pp. 852–863, 2012.

[12] R. Liu, I. Maric, P. Spasojevic, and R. D. Yates, "Discrete memoryless interference and broadcast channels with confidential messages: secrecy rate regions," *IEEE Transactions on Information Theory*, vol. 54, no. 6, pp. 2493–2507, 2008.

[13] Z. Li, R. D. Yates, and W. Trappe, "Secrecy capacity region of a class of one-sided interference channel," in *Proceedings of the IEEE International Symposium on Information Theory (ISIT '08)*, pp. 379–383, Toronto, Canada, July 2008.

[14] O. O. Koyluoglu, H. El Gamal, L. Lai, and H. V. Poor, "Interference alignment for secrecy," *IEEE Transactions on Information Theory*, vol. 57, no. 6, pp. 3323–3332, 2011.

[15] X. He and A. Yener, "The gaussian many-to-one interference channel with confidential messages," *IEEE Transactions on Information Theory*, vol. 57, no. 5, pp. 2730–2745, 2011.

[16] J. Zhu, J. Mo, and M. Tao, "Cooperative secret communication with artificial noise in symmetric interference channel," *IEEE Communications Letters*, vol. 14, no. 10, pp. 885–887, 2010.

[17] Z. Fei, J. Ni, D. Zhao, C. Xing, N. Wang, and J. Kuang, "Ergodic secrecy rate of two-user MISO interference channels with statistical CSI," submitted to *Science China Information Sciences*.

[18] S. A. A. Fakoorian and A. L. Swindlehurst, "MIMO interference channel with confidential messages: achievable secrecy rates and precoder design," *IEEE Transactions on Information Forensics and Security*, vol. 6, no. 3, pp. 640–649, 2011.

[19] S. Vishwanath, N. Jindal, and A. Goldsmith, "Duality, achievable rates, and sum-rate capacity of Gaussian MIMO broadcast channels," *IEEE Transactions on Information Theory*, vol. 49, no. 10, pp. 2658–2668, 2003.

[20] J. Li and A. P. Petropulu, "Ergodic secrecy rate for multiple-antenna wiretap channels with rician fading," *IEEE Transactions on Information Forensics and Security*, vol. 6, no. 3, pp. 861–867, 2011.

[21] D. H. Bailey, K. Jeyabalan, and X. S. Li, "A comparison of three high-precision quadrature schemes," *Experimental Mathematics*, vol. 14, no. 3, pp. 317–329, 2005.

[22] M. Alexander, F. A. Graybill, and D. C. Boes, *Introduction to the Theory of Statistics*, McGraw-Hill, 1974.

[23] E. A. Jorswieck and R. Mochaourab, "Secrecy rate region of MISO interference channel: pareto boundary and non- cooperative games," in *Proceedings of the International Workshop Smart Antennas*, Berlin, Germany, 2009.

[24] J. Lindblom, E. Karipidis, and E. G. Larsson, "Closed-form parameterization of the Pareto boundary for the two-user MISO interference channel," in *Proceedings of the 36th IEEE International Conference on Acoustics, Speech, and Signal Processing (ICASSP '11)*, pp. 3372–3375, Prague, Czech Republic, May 2011.

[25] P. Dubey, "Inefficiency of Nash equilibria," *Mathematics of Operations Research*, vol. 11, no. 1, pp. 1–8, 1986.

[26] E. G. Larsson and E. A. Jorswieck, "Competition versus cooperation on the MISO interference channel," *IEEE Journal on Selected Areas in Communications*, vol. 26, no. 7, pp. 1059–1069, 2008.

Hindawi Publishing Corporation
International Journal of Antennas and Propagation
Volume 2013, Article ID 764507, 8 pages
http://dx.doi.org/10.1155/2013/764507

Research Article

Dynamic Beamforming for Three-Dimensional MIMO Technique in LTE-Advanced Networks

Yan Li, Xiaodong Ji, Dong Liang, and Yuan Li

Wireless Signal Processing and Network Lab, Key Laboratory of Universal Wireless Communications (Ministry of Education), Beijing University of Posts and Telecommunications, Beijing 100876, China

Correspondence should be addressed to Yan Li; ly19880928@gmail.com

Received 8 March 2013; Revised 3 July 2013; Accepted 4 July 2013

Academic Editor: Feifei Gao

MIMO system with large number of antennas, referred to as large MIMO or massive MIMO, has drawn increased attention as they enable significant throughput and coverage improvement in LTE-Advanced networks. However, deploying huge number of antennas in both transmitters and receivers was a great challenge in the past few years. Three-dimensional MIMO (3D MIMO) is introduced as a promising technique in massive MIMO networks to enhance the cellular performance by deploying antenna elements in both horizontal and vertical dimensions. Radio propagation of user equipments (UE) is considered only in horizontal domain by applying 2D beamforming. In this paper, a dynamic beamforming algorithm is proposed where vertical domain of antenna is fully considered and beamforming vector can be obtained according to UEs' horizontal and vertical directions. Compared with the conventional 2D beamforming algorithm, throughput of cell edge UEs and cell center UEs can be improved by the proposed algorithm. System level simulation is performed to evaluate the proposed algorithm. In addition, the impacts of downtilt and intersite distance (ISD) on spectral efficiency and cell coverage are explored.

1. Introduction

As is generally known, long-term evolution (LTE) designed by the third generation partnership project (3GPP) helps operators to provide wireless broadband services with enhanced performance and capacity. A variety of targets and requirements for LTE have been suggested by 3GPP, including higher peak data rates and more UEs per cell as well as lower control plane latency than currently employed 3G architectures [1, 2]. Based on orthogonal frequency division multiple access (OFDMA), radio technology applies various scheduling and multiantenna methods. 3G LTE is further developed to meet requirements set for IMT-Advanced technologies. The role of antenna parameter selection in evolution of 3G LTE-Advanced has been widely discussed currently [3].

As one of the key techniques in LTE-Advanced system, multiple input multiple output (MIMO) [4–6] is considered as an effective way to obtain high data rates without sacrificing bandwidth and to improve the performance of both cell edge UE and the whole system. A trend toward deploying larger number of antennas [7, 8] can be noted in the evolution of some standards such as IEEE 802.11n/802.11ac and LTE. With Massive MIMO, huge numbers of elements in antenna arrays are able to deployed in systems being built today [9]. Larger numbers of terminals can always be accommodated by combining massive MIMO technology with conventional time and frequency division multiplexing via orthogonal frequency division multiplexing (OFDM). Massive MIMO is a new research field in communication theory, propagation, and electronics and represents a paradigm shift in the way of considering with regard to theory, systems, and implementation.

Three-dimensional MIMO (3D MIMO) can be seen as an effective method to approach massive MIMO without applying too much antennas on transmitter or receiver. Vertical dimension will be utilized in the antenna modeling, and downtilt of the antennas will become significant channel parameters. A typical two-dimensional (2D) antenna is used to cover a sector of 120 degrees only in horizontal domain [10]. Compared with the 2D channel propagation, scatterer is no longer located in the same plane with antennas and is supposed to distribute randomly in three-dimensional space.

We are considering the possibility of extending the current 2D antenna to the future 3D antenna, which means that the departure and arrival angles have to be modeled in two directions, that is, horizontal and vertical [11–13].

Beamforming of linear array antenna elements merely in horizontal dimension does not give full free-space gain. This is due to the azimuth spread of the received signal as seen from the base station (BS), which has been extensively investigated in previous studies. It is necessary to propose a novel beamforming algorithm which includes the gain of the vertical dimension. In this paper, we will present a dynamic beamforming algorithm in which vertical difference of 3D antennas will be taken into account. In conventional 2D MIMO scenario, cell edge UEs suffer serious intercell interference from neighboring cell due to their locations [14, 15]. Since the radio propagation from a transmission node to a UE is divided into horizontal direction and vertical direction, the power of intercell interference can be reduced largely, which results in an enhancement of the signal to interference plus noise ratio (SINR). Compared with the existing 2D beamforming algorithm, better system performance can be brought by dynamic beamforming algorithm.

The rest of this paper is organized as follows. Section 2 describes the system model of the downlink LTE-Advanced networks and the modeling of 3D MIMO channel. The principle and details of the dynamic beamforming algorithm are introduced in Section 3, and performance of the proposed algorithm with different configuration parameters is simulated and analyzed in Section 4. The conclusion of this paper is given in Section 5.

2. System Model

2.1. 3D MIMO System. The downlink of a cellular network with M hexagonal cells is considered as depicted in Figure 1, and each cell is partitioned into 3 sectors with K active UEs served within the coverage of each sector. The total number of BSs in the system is $3M$. Each BS which corresponds to one sector is equipped with N_t transmitting antennas, while each UE has N_r receiving antennas. For the received signal at the kth UE served by BS m, we have

$$\mathbf{y}_m^{(k)} = \underbrace{\mathbf{H}_m^{(k)}\mathbf{W}_m^{(k)}\mathbf{s}_m^{(k)}}_{\text{desired signal}} + \underbrace{\sum_{n\neq m}^{3M}\sum_{w=1}^{K}\mathbf{H}_n^{(k)}\mathbf{W}_n^{(k)}\mathbf{s}_n^{(w)}}_{\text{inter-sector interference}} + \mathbf{n}_m^{(k)}, \quad (1)$$

where $\mathbf{s}_m^{(k)}$ is the $l_k \times 1$ transmitted vector for UE k served by BS m and l_k is the number of data stream. Denote $\mathbf{s}_m^{(k)} = [\sqrt{p_k}s_{m,1}^{(k)}, \sqrt{p_k}s_{m,2}^{(k)}, \ldots, \sqrt{p_k}s_{m,l_k}^{(k)}]^T$, and p_k is the transmitting power of each data stream at UE k. For 3D MIMO, due to the introduction of vertical dimension in transmitting antenna, the channel coefficient matrix is three-dimensional, that is, the number of receiving antenna, the number of transmitting antenna, and the number of elevation element. It is assumed that each transmitting antenna has N_v elements,

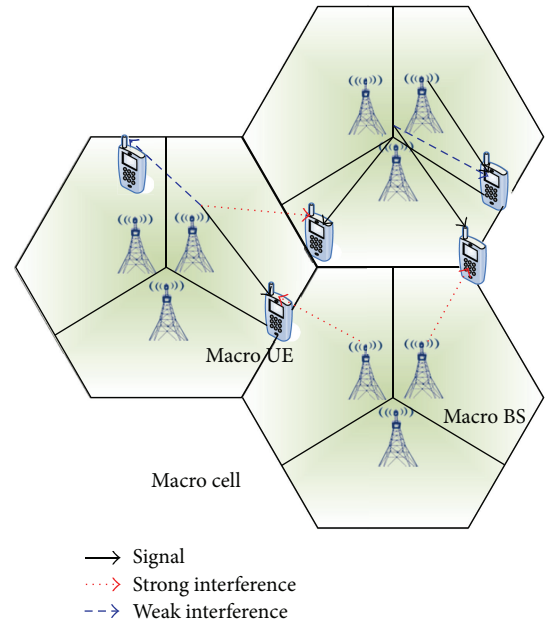

Figure 1: System model for downlink transmission of LTE-Advanced networks.

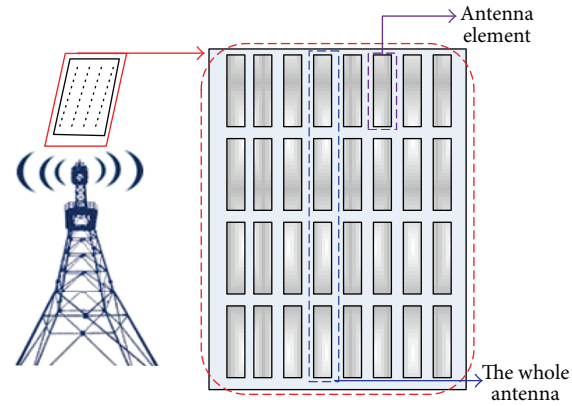

Figure 2: Structure of 8 × 4 rectangular 3D antenna array.

and receiving antenna remains as a conventional 2D antenna without a different element in vertical dimension. Thus, $\mathbf{H}_m^{(k)}$ is the $N_r \times (N_t \times N_v)$ channel matrix from BS m to UE k, and $\mathbf{W}_m^{(k)}$ is the $(N_t \times N_v) \times l_k$ precoding matrix. $\mathbf{n}_m^{(k)}$ is the additive white Gaussian noise with zero mean and variance $\mathbb{E}(\mathbf{n}_m^{(k)}\mathbf{n}_m^{(k)H}) = \sigma^2$. The detailed analysis of detected SINR for the received signal is in [16, 17].

2.2. 3D Antenna Modeling. Most geometry-based stochastic radio channel models are two-dimensional (2D) in the sense that they use only geometrical xy-coordinates or equivalent parameters of distance and rotation angle. This has been sufficient until these days, while vertical dimension of the arrays and the height of the BS are fully considered in 3D antenna [18, 19]. For instance, structure of 8 × 4 arrays with "rectangular" elements is shown in Figure 2.

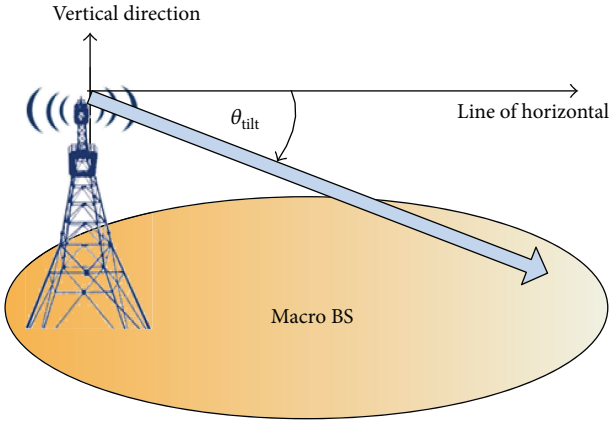

Figure 3: Electrical downtilt.

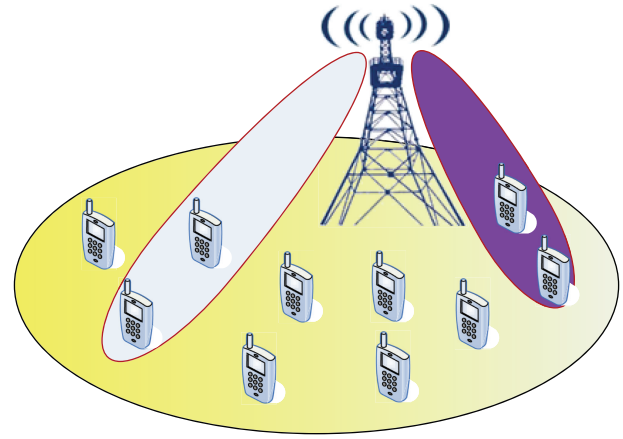

Figure 4: Conventional 2D MIMO beamforming.

The whole antenna can be divided into several elements which are controlled by different antenna port. Assuming that 14 dB is the maximum direction gain of an antenna, equal power is given for each element as defined in

$$G_{\max} = 14 - 10\log_{10} N_v, \tag{2}$$

where $G_{\max}$ is the maximum directional gain of the array elements and N_v is the number of elevation element.

In 3GPP LTE-Advanced simulations, we apply two formulas below for horizontal and vertical radiation patterns so that horizontal antenna gain and vertical antenna gain can be obtained, respectively:

$$\begin{aligned} A_H(\varphi) &= -\min\left[12\left(\frac{\varphi}{\varphi_{3\,\text{dB}}}\right), A_m\right], \\ A_m &= 20\,\text{dB}, \\ A_V(\theta) &= -\min\left[12\left(\frac{\theta-\theta_{\text{tilt}}}{\theta_{3\,\text{dB}}}\right), \text{SLA}_v\right], \\ \text{SLA}_v &= 20\,\text{dB}, \end{aligned} \tag{3}$$

where φ is defined as the angle between the direction of interest and the boresight of the antenna in horizontal dimension, which is similar to θ in vertical dimension. $\varphi_{3\,\text{dB}}$ and $\theta_{3\,\text{dB}}$ are the 3 dB beamwidth of the horizontal beam and the vertical beam, respectively. θ_{tilt} is the downtilt angle in transmitter. A_m is the front-to-back attenuation, and SLA_v is side lobe attenuation.

The 3D antenna gain is combined as a sum of horizontal pattern and elevation pattern antenna gain. Generation of the 3D pattern from two perpendicular cross-sections azimuth and elevation patterns is denoted as below:

$$A(\varphi,\theta) = -\min\left\{-\left[A_H(\varphi) + A_V(\theta)\right], A_m\right\}, \tag{4}$$

The angle of the main beam of the antenna up/below the horizontal plane is called antenna tilt as shown in Figure 3. Positive and negative angles are referred to as downtilt and uptilt, respectively. In electrical downtilt, main, side, and back lobes are tilted uniformly by adjusting phases of antenna elements [20].

Angle $\theta_{(i,k)}$ between horizontal line and LOS direction of connecting BS i and UE k in vertical plane is obtained by

$$\theta_{(i,k)} = \arctan\left(\frac{h_{(i,k)}}{d_{(i,k)}}\right), \tag{5}$$

where $d_{(i,k)}$ is distance between UE k and BS i and $h_{(i,k)}$ is the height difference between the antenna of UE k and the antenna of BS i.

3. Algorithms for 3D Dynamic Beamforming

3.1. 2D MIMO Beamforming. Conventional beamforming can be seen as a sort of 2D cell-specific beamforming. The UE data to be transmitted is processed in accordance with the channel information only in the horizontal dimension. The transmitter forms a small beam within the antenna radiation pattern to point at the UE to be served. This means that only in the horizontal dimension the UE channel state information is being tracked and utilized. Only in the case of several UEs within a cell, the horizontal antenna beam generated by beamforming can distinguish different UEs well.

However, as the UEs in a cell increase substantially, several UEs that request for service at the same time may be located in the same azimuth angle as shown in Figure 4, which means that 2D antenna gain from the serving BS is equivalent. Once several UEs are close to each other and located in the cell edge area, they own the same power of desired signal but will suffer serious intercell interference. In this case, transmitting beam simply formed by horizontal dimension beamforming is not enough to distinguish different UEs. For instance, if the beam is aligned with the UE near the base station, the remote UEs will be outside the range of radiation; otherwise, the beam aligned with the UEs far from the base station will result in severe intercell interference to the neighbor cell.

3.2. Proposed Beamforming Algorithm. In the same frequency resource allocation networks, the intercell interference decreases the performance of cell edge UE dramatically.

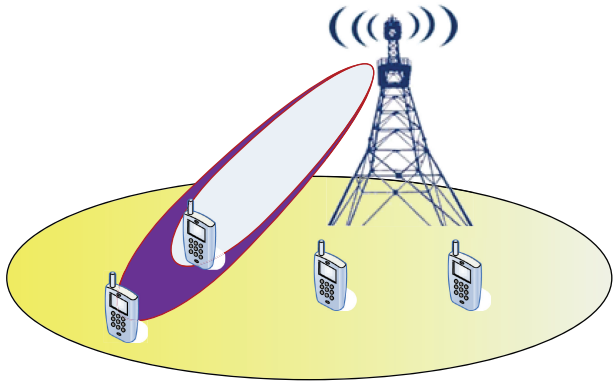

Figure 5: 3D dynamic beamforming in horizontal sight.

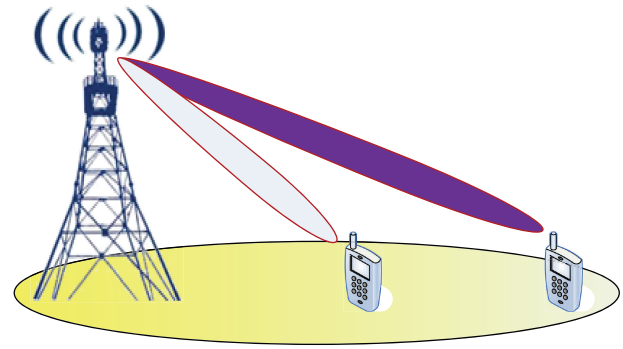

Figure 6: 3D dynamic beamforming in vertical sight.

3D MIMO can be seen as a dynamic interference cancellation method, which aims to eliminate intercell interference coming from neighbor cells and improve the throughput of cell edge UE through 3D dynamic beamforming. For each UE, since the introduction of vertical dimension, difference in height between BS and UE has been taken into account, and UE's position should be considered in three-dimension. According to both horizontal and vertical directions of the specific UE, transmitting beam generated by 3D antennas can be divided into both horizontal and vertical dimensions, which means it has much less influence on other UEs.

For instance, the two UEs in Figures 5 and 6 have the same azimuth angle. When they are scheduled at the same time, identical horizontal beam direction is shared. Due to the introduction of dynamic beamforming algorithm, transmitter is able to form two different vertical beams through setting different vertical power weight on the antenna elements. Thus, different maximum beam direction can be discriminated for the two specific UEs. Among noncodebook-based precoding technique, the calculation of the 3D MIMO beamforming vector seriously affects the performance of the interference cancellation, and the method of combining suitable horizontal beamforming vector and vertical beamforming vector together should be a big problem needed to be solved.

To implement precoding at BS, an improved beamforming algorithm is adopted. It is assumed that one UE is served by all the antenna elements, and data from a BS is transmitted in a single stream. Antenna number at Macro BS is N_t, and UE has N_r antennas. Firstly, compared with the conventional algorithms such as SVD algorithm and BD algorithm, equivalent process is done with the channel between BSs and UEs, and then traditional precoding methods are utilized. The main procedure of dynamic beamforming is as follows.

Step 1. Computation of horizontal beamforming vector. The horizontal beamforming vector represents the transmitting weight of the elements from different antenna in horizontal dimension. Therefore, the dimension of each horizontal beamforming vector is $N_t \times 1$. For there are N_v elements in an antenna, the total number of horizontal beamforming vector should be N_v. The channel from N_v layer antenna elements in transmitter to UE_k is $\mathbf{H}_{k,1}, \mathbf{H}_{k,2}, \ldots, \mathbf{H}_{k,N_v}$, respectively, and $\mathbf{H}_{k,i}$ denotes the $N_r \times N_t$ channel matrix from the ith layer transmitting antenna elements to UE_k. $\mathbf{V}_{k,i} \sim \mathrm{SVD}(\mathbf{H}_{k,i})$; $\mathbf{V}_{k,i}$ is the $\mathbf{V}$ matrix from the SVD decomposition of $\mathbf{H}_{k,i}$. $\mathbf{v}_{k,i}$ is the first column of matrix $\mathbf{V}_{i,k}$. The horizontal beamforming vector $\mathbf{v}_{\mathrm{horizontal}}$ for the whole antenna elements can be expressed as

$$\mathbf{v}_{\mathrm{horizontal}} = \left[\mathbf{v}_{k,1}^T, \mathbf{v}_{k,2}^T, \ldots, \mathbf{v}_{k,N_v}^T\right], \tag{6}$$

Step 2. Computation of vertical beamforming vector. The vertical beamforming vector represents the transmitting weight of the elements from a single antenna in vertical dimension. Therefore, the dimension of each vertical beamforming vector is $N_v \times 1$. For there is actual N_t antenna in transmitter, the total number of vertical beamforming vector should be N_t. The channel from vertical elements of N_t antennas in transmitter to UE_k is $\mathbf{H}_{k,1}^*, \mathbf{H}_{k,2}^*, \ldots, \mathbf{H}_{k,N_t}^*$, respectively; $\mathbf{H}_{k,i}^*$ denotes the $N_r \times N_v$ channel matrix from the vertical elements of the ith transmitting antenna to UE_k. $\mathbf{V}_{k,i}^* \sim \mathrm{SVD}(\mathbf{H}_{k,i}^*)$, where $\mathbf{V}_{k,i}^*$ is the $\mathbf{V}$ matrix from the SVD decomposition of $\mathbf{H}_{k,i}^*$. $\mathbf{v}_{k,i}^*$ is the first column of matrix $\mathbf{V}_{k,i}^*$. The vertical beamforming vector $\mathbf{v}_{\mathrm{vertical}}$ for the whole antenna elements can be expressed as

$$\mathbf{v}_{\mathrm{vertical}} = \left[\left(\mathbf{v}_{k,1}^*\right)^T, \left(\mathbf{v}_{k,2}^*\right)^T, \ldots, \left(\mathbf{v}_{k,N_t}^*\right)^T\right], \tag{7}$$

Step 3. Combination of horizontal beamforming vector and vertical beamforming vector. There are totally $N_v \times N_t$ antenna elements in transmitter. $\mathbf{H}$ is a combined channel and $\mathbf{H} = [\mathbf{H}_{k,1}^T, \mathbf{H}_{k,2}^T, \ldots, \mathbf{H}_{k,N_v}^T]$. Each element has its own horizontal transmitting weight as computed in Step 1. Thus, the complete horizontal beamforming vector's dimension is $N_v \times N_t \times 1$, combined by N_v subvectors which own dimension of $N_t \times 1$. Similar process is done with the complete vertical beamforming vector that N_t subvectors represent N_t antennas' vertical transmitting weight, respectively. Thus, vertical beamforming vector is generated from row combination of subvector $\mathbf{v}_{k,1}^*, \ldots, \mathbf{v}_{k,N_t}^*$ in Step 2. Finally, the dynamic beamforming vector is obtained from the complete horizontal beamforming vector and the complete vertical

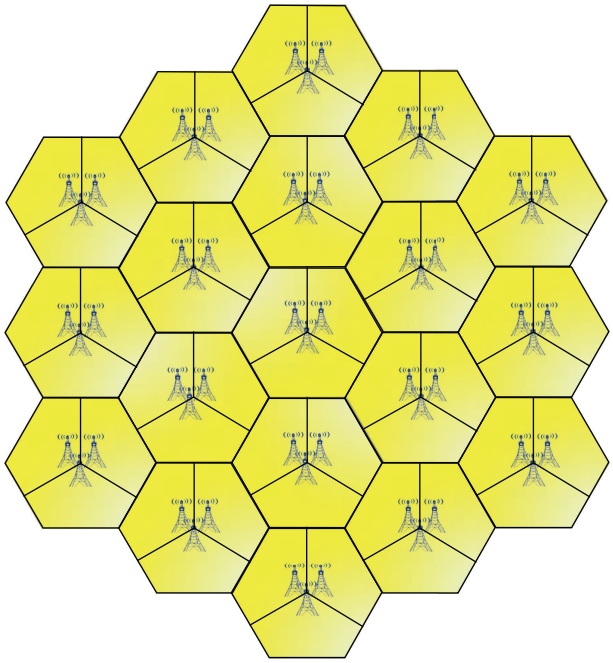

Figure 7: 19 cells' topological structure.

beamforming vector, for dot production will be done with these two $N_v \times N_t \times 1$ vectors. 3D beamforming vector $\mathbf{w}$ is available as follows:

$$\mathbf{w} = \mathbf{v}_{\text{horizontal}} * \mathbf{v}_{\text{vertical}}, \tag{8}$$

where the dimension of 3D dynamic beamforming vector is $N_v \times N_t \times 1$, representing $N_v \times N_t$ antenna elements' dynamic power transmitting weight.

4. Simulation Results

In this section, system level performance of the proposed 3D dynamic beamforming algorithm is evaluated in terms of average spectral efficiency, cell edge UE spectral efficiency, and SINR of the UEs. Consider a system with 19 homogeneous cells as shown in Figure 7. Each cell consists of 3 Macro BSs, which is supposed to provide service to its own sector's UEs. It is worth noting that the 3 BSs are located in the center of the cell, which means they share the same coordinate point. In order to eliminate border effect, wrap-around technique is used to simulate interference generated by UEs from at least 2 layers' neighbor cells. Since the simulated scene is configured to Uma (Urban Macro-cell), only outdoor UEs exist during the simulation process. Other detailed simulation parameters are listed in Table 1.

Figure 8(a) is the average spectral efficiency of different downtilt angle deployments with sector radius of 288 m. The performance of 3D MIMO without dynamic beamforming has 5%, 14%, 22%, and 24% enhancement compared to 2D MIMO networks, respectively. Although array gain due to the introduction of 3D MIMO can be obtained in the system, beamforming gain is not included in the performance improvement. As can be seen in the figure, the proposed dynamic beamforming algorithm is able to offer substantial beamforming gain compared to static beamforming. About 14%, 24%, 32%, and 34% of the gain compared to 2D MIMO can be achieved by the novel beamforming algorithm with different downtilt angle parameter. It can be concluded that the performance of 14° outperforms the performance of other 3 downtilt angles for the scenario with sector radius of 288 m.

Figure 8(b) is the cell edge UE (5% CDF) spectral efficiency. The proposed dynamic beamforming algorithm offers large performance gain compared to 2D MIMO networks as the intercell interference decreases apparently. For cell edge UEs, the UE spectral efficiency has been increased by about 21%, 51%, 79%, and 92%, respectively, and the performance of coverage has been increased dramatically.

For different scenarios with sector radius of 500 m, Figure 8(c) shows the average spectral efficiency of different

Table 1: Simulation configuration parameters.

Parameters	Assumptions
Cell type	Macro cell
Cellular layout	19 cells, each with 3 sectors
Sector radius	288 m, 500 m
Bandwidth	5 M
Channel model	WINNER II
Shadowing standard deviation	8 dB
Antenna number	Transmitter: 2Tx, Receiver: 2Rx
Antenna configuration	Co-polarized linear array
Antenna spacing	Transmitter: 0.5λ, Receiver: 0.5λ
Number of elevation element	2
Regular antenna gain	14 dBi
Downtilt angle	8°, 10°, 12°, 14°
BS max TX power	46 dBm
BS height	25 m
UE height	1.5 m
UE distribution	Uniformly distributed
UE numbers	10 UEs per sector
UE speed	3 km/h
Initial UE access criterion	Access by location
Scheduler	Proportional fair
CQI reporting interval	5 ms
Delay for scheduling and AMC	5 ms
Receiver	MMSE
Traffic model	Full buffer

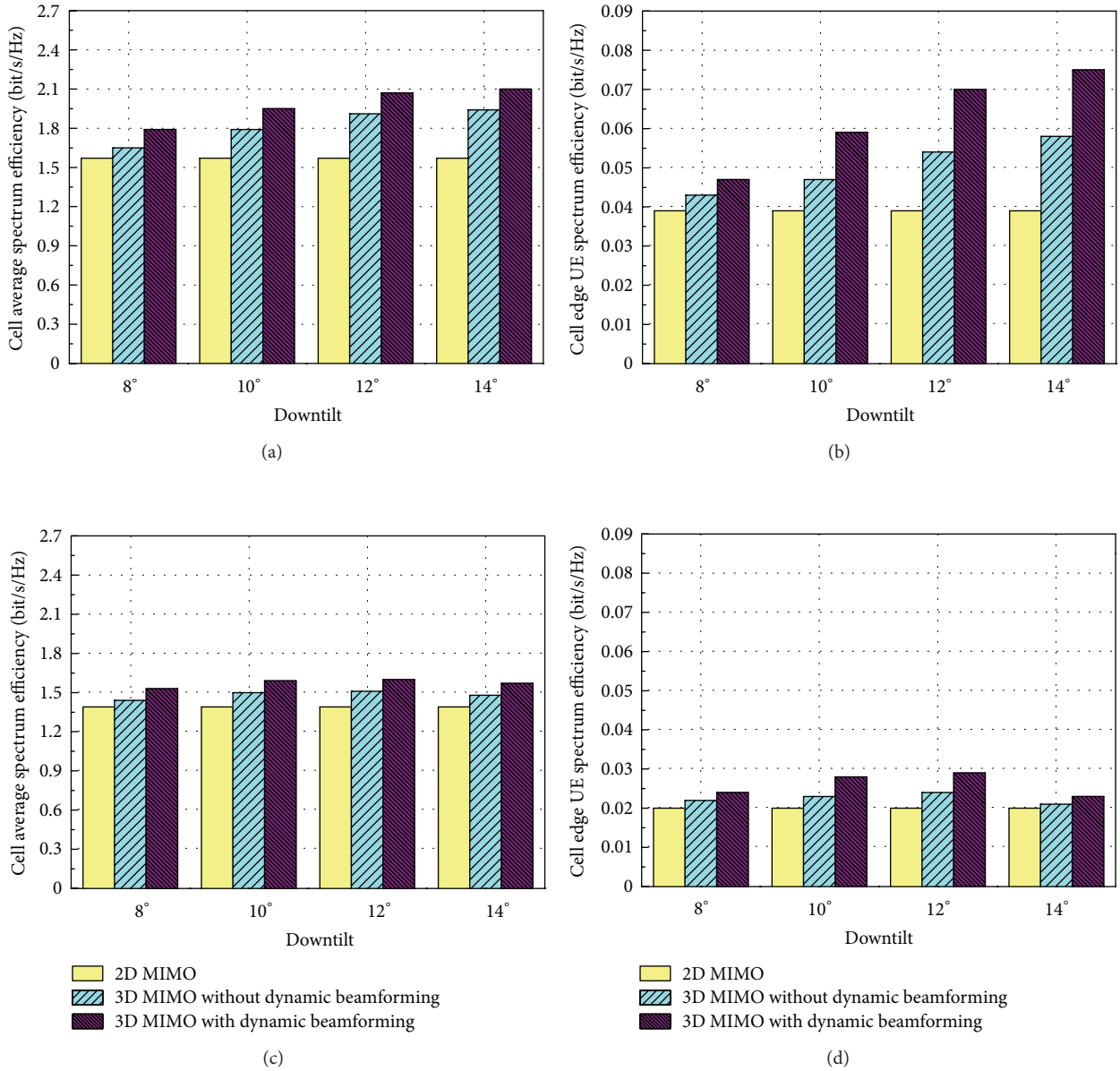

Figure 8: System level results of 2D MIMO, 3D MIMO without dynamic beamforming and 3D MIMO with dynamic beamforming: (a) cell average spectral efficiency with sector radius of 288 m; (b) cell edge UE spectral efficiency with sector radius of 288 m; (c) cell average spectral efficiency with sector radius of 500 m; (d) cell edge UE spectral efficiency with sector radius of 500 m.

downtilt angle deployments, and the performance of 3D MIMO with dynamic beamforming has 10%, 14%, 15%, and 13% enhancement compared to 2D MIMO networks, respectively. Since the radius of sector increases, the distribution of UEs within a sector changes a lot, and the elevation angles of UEs in the area decrease. Downtilt angle should be adjusted so as to cover more UEs. It can be observed from Figure 8 that the performance of 12° outperforms the performance of other 3 downtilt angles for the scenario with sector radius of 500 m.

For cell edge UEs, the UE spectral efficiency has been increased by about 20%, 40%, 45%, and 15% respectively as presented in Figure 8(d). Although the density of UE changed, the proposed algorithm can still offer considerable gain compared with 2D MIMO networks.

Figure 9 shows the receive SINR CDF curves of 2D MIMO UEs, 3D MIMO without dynamic beamforming UEs, and 3D MIMO with dynamic beamforming UEs. For scenario with sector radius of 288 m, the downtilt angle is set for 14° as summarized above. With the proposed algorithm,

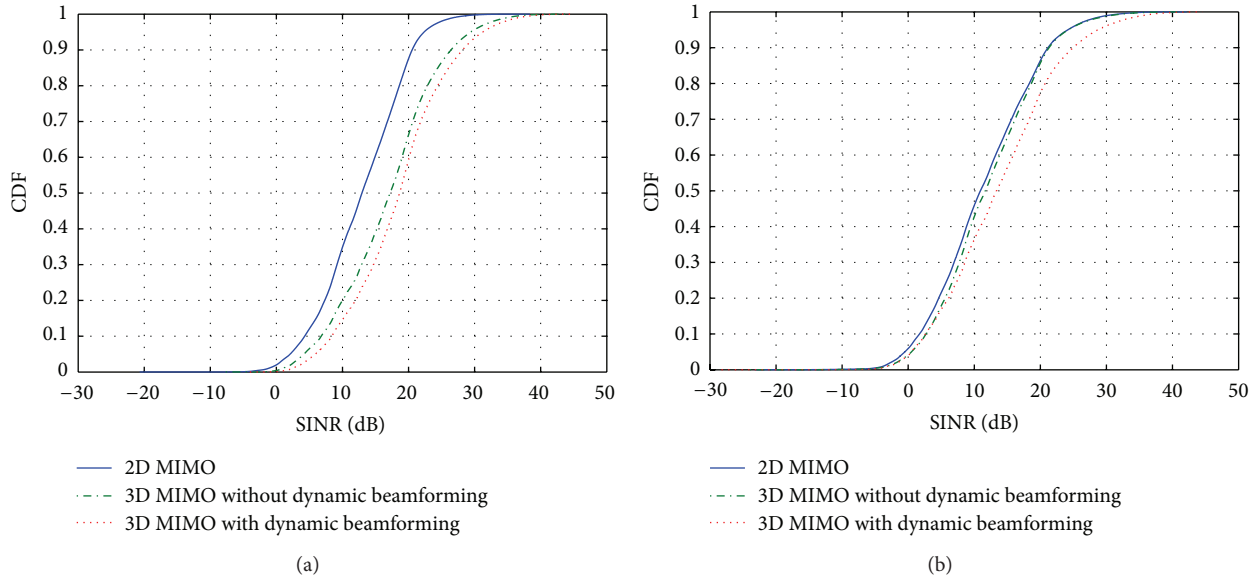

Figure 9: System level results of receive SINR CDF for 2D MIMO, 3D MIMO without dynamic beamforming and 3D MIMO with dynamic beamforming: (a) sector radius: 288 m; (b) sector radius: 500 m.

the SINR of the 3D MIMO with dynamic beamforming outperforms by 6 dB compared to the 2D MIMO and has approximately 2 dB gain compared with the 3D MIMO without dynamic beamforming. Both cell average UE and cell edge UE can be served much better than before.

Under the influence of larger sector radius, the change of downtilt configuration is not so apparent as it performs in 288 m scenario. Compared with the UEs in 288 m scenario, some UEs in 500 m scenario will receive decreased signal power so that less gain can be obtained in the average received SINR of UEs in 500 m scenario. Thus, there is not much difference between the SINR curved line of 2D MIMO UE and the SINR curved line of 3D MIMO UE as depicted in Figure 9(b). In spite of this, the positive effect brought by the proposed algorithm is still obvious.

5. Conclusion

In this paper, modeling of 3D channel and structure of 3D antenna have been introduced. A dynamic beamforming algorithm for 3D MIMO in LTE-Advanced networks is proposed, which can be proved as an effective method to reduce intercell interference. Simulation results for 3D MIMO with different downtilt angle parameters and sector radius parameters are presented. Compared with 2D beamforming, 3D dynamic beamforming can improve both the cell edge UE throughput and the whole system's performance significantly. At most 34% gain for cell center UE and 92% gain for cell edge UE over the conventional 2D beamforming are achieved, and the performance differences of different scenarios are analyzed in this paper.

Acknowledgments

This work was supported in part by the State Major Science and Technology Special Projects (Grant no. 2012ZX03001028-004, 2013ZX03001001-002, and 2013ZX03001001-003) and the Beijing Natural Science Foundation (Grant no. 4131003).

References

[1] M. Peng and W. Wang, "Technologies and standards for TD-SCDMA evolutions to IMT-advanced," *IEEE Communications Magazine*, vol. 47, no. 12, pp. 50–58, 2009.

[2] M. Peng, W. Wang, and H.-H. Chen, "TD-SCDMA evolution," *IEEE Vehicular Technology Magazine*, vol. 5, no. 2, pp. 28–41, 2010.

[3] 3GPP TS 36. 814 V0. 4. 1, Evolved universal terrestrial radio access (E-UTRA), Further advancements for E-UTRA physical layer aspects.

[4] L. Liu, R. Chen, S. Geirhofer, K. Sayana, Z. Shi, and Y. Zhou, "Downlink MIMO in LTE-advanced: SU-MIMO vs. MU-MIMO," *IEEE Communications Magazine*, vol. 50, no. 2, pp. 140–147, 2012.

[5] M. Peng, Z. Ding, Y. Zhou, and Y. Li, "Advanced self-organizing technologies over distributed wireless networks," *International Journal of Distributed Sensor Networks*, vol. 2012, Article ID 821982, 2 pages, 2012.

[6] O. N. C. Yilmaz, S. Hämäläinen, and J. Hämäläinen, "Analysis of antenna parameter optimization space for 3GPP LTE," in *Proceedings of the IEEE 70th Vehicular Technology Conference Fall (VTC '09)*, Anchorage, Alaska, USA, September 2009.

[7] S. K. Mohammed, A. Zaki, A. Chockalingam, and B. S. Rajan, "High-rate space-time coded large-MIMO systems: low-complexity detection and channel estimation," *IEEE Journal on*

Selected Topics in Signal Processing, vol. 3, no. 6, pp. 958–974, 2009.

[8] M. Peng, G. Xu, W. Wang, and H.-H. Chen, "McWiLL-a new mobile broadband access technology for supporting both voice and packet services," *IEEE Systems Journal*, vol. 4, no. 4, pp. 495–504, 2010.

[9] F. Rusek, D. Persson, B. K. Lau et al., "Scaling up MIMO: opportunities and challenges with very large arrays," *IEEE Signal Processing Magazine*, vol. 30, no. 1, 2013.

[10] P. Zetterberg, "Performance of antenna tilting and beamforming in an urban macrocell," in *Proceedings of the 1st International Conference on Wireless Communication, Vehicular Technology, Information Theory and Aerospace and Electronic Systems Technology, Wireless (VITAE '09)*, pp. 201–206, Aalborg, Denmark, May 2009.

[11] IST-4-027756 WINNER II D1.1.2 V1.2 WINNER II channel models.

[12] IST-WINNER D5.3 WINNER+ Final channel models v1.0.

[13] IST-2003-507581 WINNER D5.4 Final report on link level and system level channel models v1.4.

[14] X. You, D. Wang, P. Zhu, and B. Sheng, "Cell edge performance of cellular mobile systems," *IEEE Journal on Selected Areas in Communications*, vol. 29, no. 6, pp. 1139–1150, 2011.

[15] T. Zhou, M. Peng, W. Wang, and H. Chen, "Low-complexity coordinated beamforming for downlink multi-cell SDMA/OFDM system," *IEEE Transactions on Vehicular Technology*, vol. 62, no. 1, 2013.

[16] F. Shu, L. Lihua, C. Qimei, and Z. Ping, "Non-unitary codebook based precoding scheme for multi-user MIMO with limited feedback," in *Proceedings of the IEEE Wireless Communications and Networking Conference (WCNC '08)*, pp. 678–682, April 2008.

[17] M. Peng, X. Zhang, W. Wang, and H.-H. Chen, "Performance of dual-polarized MIMO for TD-HSPA evolution systems," *IEEE Systems Journal*, vol. 5, no. 3, pp. 406–416, 2011.

[18] M.-T. Dao, V.-A. Nguyen, Y.-T. Im, S.-O. Park, and G. Yoon, "3D polarized channel modeling and performance comparison of MIMO antenna configurations with different polarizations," *IEEE Transactions on Antennas and Propagation*, vol. 59, no. 7, pp. 2672–2682, 2011.

[19] G. Auer, "3D MIMO-OFDM channel estimation," *IEEE Transactions on Communications*, vol. 60, no. 4, pp. 972–985, 2012.

[20] O. N. C. Yilmaz, S. Hämäläinen, and J. Hämäläinen, "Comparison of remote electrical and mechanical antenna downtilt performance for 3GPP LTE," in *Proceedings of the IEEE 70th Vehicular Technology Conference Fall (VTC '09)*, Anchorage, Alaska, USA, September 2009.

Hindawi Publishing Corporation
International Journal of Antennas and Propagation
Volume 2013, Article ID 718482, 5 pages
http://dx.doi.org/10.1155/2013/718482

Research Article

Power Scaling for Spatial Modulation with Limited Feedback

Yue Xiao, Qian Tang, Lisha Gong, Ping Yang, and Zongfei Yang

National Key Laboratory of Science and Technology on Communications, University of Electronic Science and Technology of China, Chengdu 610054, China

Correspondence should be addressed to Yue Xiao; xiaoyue1979@gmail.com

Received 8 February 2013; Revised 6 May 2013; Accepted 8 May 2013

Academic Editor: Feifei Gao

Spatial modulation (SM) is a recently developed multiple-input multiple-output (MIMO) technique which offers a new tradeoff between spatial diversity and spectrum efficiency, by introducing the indices of transmit antennas as a means of information modulation. Due to the special structure of SM-MIMO, in the receiver, maximum likelihood (ML) detector can be combined with low complexity. For further improving the system performance with limited feedback, in this paper, a novel power scaling spatial modulation (PS-SM) scheme is proposed. The main idea is based on the introduction of scaling factor (SF) for weighting the modulated symbols on each transmit antenna of SM, so as to enlarge the minimal Euclidean distance of modulated constellations and improve the system performance. Simulation results show that the proposed PS-SM outperforms the conventional adaptive spatial modulation (ASM) with the same feedback amount and similar computational complexity.

1. Introduction

Spatial modulation (SM) [1] is a recently proposed multiple-input multiple-output (MIMO) transmission technique, in which the index of the transmit antenna is utilized for information modulation in the spatial domain. The main advantages of SM-MIMO can be described as follows. Firstly, only one transmit antenna is active on each time slot so that strict time synchronization is saved. Secondly, SM-MIMO can be used for any number of receive antennas so that it adapts to downlink communications on an unbalanced MIMO channels in which the number of transmit antennas is much larger than that of receive antennas. Finally, SM-MIMO can offer a new balance between spectrum efficiency and spatial diversity compared to the conventional MIMO techniques [2, 3].

For detecting the SM-MIMO signals at the receiver side, maximum likelihood (ML) algorithm was suggested in [4] to achieve the optimal performance, which also gives a performance bound of the SM-MIMO system. For controlling the computational complexity of ML detection while approaching the performance bound, in current research, a series of near-ML detectors has been proposed [5–7] to make a tradeoff between complexity and performance.

Traditional SM-MIMO cannot exceed the ML performance bound. In this case, for further improving the system performance, in recent research, limited feedback was considered for link adapted SM-MIMO. However, these techniques have their disadvantages. For example, adaptive SM (ASM) was firstly proposed in [8] to select the modulation styles according to the channel information. In ASM, the transmission rate of each data frame is not fixed, which is not good for system design. And error propagation may happen in low-SNR domain due to the wrong demodulation for any single data symbol. Furthermore, a combination of adaptive spatial modulation and antenna section scheme is proposed in [9] to enhance the performance. However, it inherits the drawbacks of ASM, and the introduction of additional antennas will introduce extra implementation cost and channel estimation complexity.

This paper considers another aspect as adaptive power scaling for SM-MIMO with limited feedback. A novel power scaling spatial modulation (PS-SM) scheme is proposed, based on the introduction of scaling factor (SF) for weighting the modulated symbols and enlarging the minimum Euclidean distance of the transmit signals. As a result the proposed method can effectively improve the system performance. We will show that the proposed PS-SM outperforms the conventional adaptive spatial modulation (ASM) with the same feedback. In this case, PS-SM can be an alternative scheme to ASM schemes by overcoming their disadvantages.

Furthermore, the enlarging of the minimum distance could lead to an improvement of equivalent transmit power. In this paper, a power attenuation factor is introduced to keep the minimal transmit power for improving the energy efficiency.

The rest of the paper is organized as follows. In Section 2, the basic structure of SM-MIMO and main idea of adaptive schemes are summarized. The proposed PS-SM scheme is described in Section 3. In Section 4, bit-error rate (BER) performance of PS-SM and conventional schemes are disclosed by simulation results. Finally, conclusions are given in Section 5.

2. Conventional SM and Adaptive Scheme

Assume an SM-MIMO [1] with N transmit and M receive antennas. The information bits vector $\mathbf{b}$, with length L, can be divided into two parts as $\log_2 N$ and $\log_2 P$ (P is the size of QAM constellation) bits, as $L = \log_2 NP$. Then the bit information vector $\mathbf{b}$ is mapped into transmit vector $\mathbf{x} = [0, \ldots, x_n^p, \ldots, 0]$ with length N, in which there is only one nonzero element x_n^p, where n is the index of transmit antennas with $n \in [1, 2, \ldots, N]$ and p is the index of QAM constellation with $p \in [1, 2, \ldots, P]$. Let $\mathbf{H}$ be the $M \times N$ MIMO channel matrix. Then the receive vector $\mathbf{y}$, with length M, can be written as

$$\mathbf{y} = \mathbf{H}\mathbf{x} + \mathbf{n} = \mathbf{h}_n x_n^p + \mathbf{n}, \tag{1}$$

where $\mathbf{h}_n$ represents the nth column of $\mathbf{H}$ and $\mathbf{n}$ is AWGN noise with variance of σ^2.

For optimal ML detector [4], the estimated SM-MIMO symbol is given by

$$\hat{\mathbf{x}} = \arg \min_{\mathbf{x} \in \Lambda} \left\| \mathbf{y} - \mathbf{H}\mathbf{x} \right\|_F^2, \tag{2}$$

where $\hat{\mathbf{x}}$ denotes the estimated transmit symbol vector, Λ is the set of all possible transmit symbols, and $\| \cdot \|_F$ represents the Frobenius norm of the vector.

The performance bound of ML detection is decided by the minimal Euclidean distance $d_{\min}$, defined as [8]

$$d_{\min} = \min_{\substack{\mathbf{x}_i, \mathbf{x}_j \in \Lambda, \\ \mathbf{x}_i \neq \mathbf{x}_j}} \left\| \mathbf{H}\left(\mathbf{x}_i - \mathbf{x}_j\right) \right\|_F. \tag{3}$$

In general, the minimal Euclidean distance $d_{\min}$ is determined by the transmit vector $\mathbf{x}$ and channel matrix $\mathbf{H}$ for conventional SM. In ASM [8, 9], the modulation styles for each antenna can be selected to offer extra freedom for generating a larger $d_{\min}$. However, ASM schemes suffer from a nonconstant data rate when different antennas employ different modulation styles. For instance, for an SM-MIMO with 2 transmit antennas, if the first and second antennas separately select BPSK and QPSK, the data rate may be variable between 2 and 3 bits/slot. Furthermore, in the receiver side, if the antenna index is estimated incorrectly, the number of the received bits will differ from that of original transmission, which will cause consecutive errors.

3. Power Scaling Spatial Modulation

For avoiding the drawback of ASM schemes, in this paper, a novel power scaling spatial modulation scheme is proposed. The system block is shown in Figure 1. Firstly, the information bits are divided into two parts to modulate the digital constellations and the active transmit antenna index. Then at each time instant one active transmit antenna is selected with a scaling factor (SF) $w_{n,k}$, $n = 1, 2, \ldots, N$, $k = 1, 2, \ldots, K$, for weighting the modulated symbols, where $w_{n,k} \in (0, 1]$ and K is the total number of candidate SF groups. In this case, the transmit SM symbol can be expressed as $\mathbf{x} = [0, \ldots, w_{n,k} x_n^p, \ldots, 0]$. For normalizing the transmit power, let $\sum_{n=1}^{N} w_{n,k}^2 = N$. According to (1) and (3), in PS-SM, the minimal Euclidean distance is a function of k, given and further computed as

$$\begin{aligned} d_{\min}(k) &= \min_{u \neq v \text{ or } i \neq j} \left\| w_{i,k} x_i^u \mathbf{h}_i - w_{j,k} x_j^v \mathbf{h}_j \right\|_F \\ &= \min_{u \neq v \text{ or } i \neq j} \left\| \begin{pmatrix} w_{i,k} x_i^u h_{1,i} \\ w_{i,k} x_i^u h_{2,i} \\ \vdots \\ w_{i,k} x_i^u h_{M,i} \end{pmatrix} - \begin{pmatrix} w_{j,k} x_j^v h_{1,j} \\ w_{j,k} x_j^v h_{2,j} \\ \vdots \\ w_{j,k} x_j^v h_{M,j} \end{pmatrix} \right\|_F \\ &= \min_{u \neq v \text{ or } i \neq j} \sqrt{x_i^u w_{i,k} m_1 + x_j^v w_{j,k} m_2 - 2\Re\left(x_i^u x_j^{v*} w_{i,k} w_{j,k} m_3\right)} \end{aligned} \tag{4}$$

with

$$\begin{aligned} m_1 &= \left|h_{1,i}^2\right|^2 + \left|h_{2,i}^2\right|^2 + \cdots + \left|h_{M,i}^2\right|^2 = \left\langle \mathbf{h}_i, \mathbf{h}_i \right\rangle, \\ m_2 &= \left|h_{1,j}^2\right|^2 + \left|h_{2,j}^2\right|^2 + \cdots + \left|h_{M,j}^2\right|^2 = \left\langle \mathbf{h}_j, \mathbf{h}_j \right\rangle, \\ m_3 &= h_{1,i} h_{1,j}^* + h_{2,i} h_{2,j}^* + \cdots + h_{M,i} h_{M,j}^* = \left\langle \mathbf{h}_i, \mathbf{h}_j \right\rangle, \end{aligned} \tag{5}$$

where $\Re(\cdot)$ denotes the real part of the input and m_1, m_2, m_3 are the inner products of the columns of the channel matrix and can be reused for reducing the calculation complexity. Comparing (4) to the processing of [8], it is shown that the proposed PS-SM scheme has similar computational complexity as ASM.

From every possible set of SF candidates as $w_{n,k}$, $k = 1, 2, \ldots, K$, there is one minimal Euclidean distance $d_{\min}(k)$. Then the optimal value of $d_{\min}(k_{\text{opt}})$, which is defined as the maximal value of $d_{\min}(k)$, is expressed as

$$k_{\text{opt}} = \arg \max \left\{ d_{\min}(k) \right\}, \quad k = 1, \ldots, K. \tag{6}$$

The only limitations for the selection of SF are given as $w_{n,k} \in (0, 1]$ and $\sum_{n=1}^{N} w_{n,k}^2 = N$. For example, we target a 2×2 PS-SM-MIMO transmission system with the scaling factors obeying uniform distribution, which is generated in Table 1, as $w_{n,k} \in \{\sqrt{0.333}, \sqrt{0.667}, \sqrt{1, 1.333}, \sqrt{1.667}\}$. With limited feedback, the proposed PS-SM algorithm presets the same candidate SF sets at both transceiver sides. And the selected

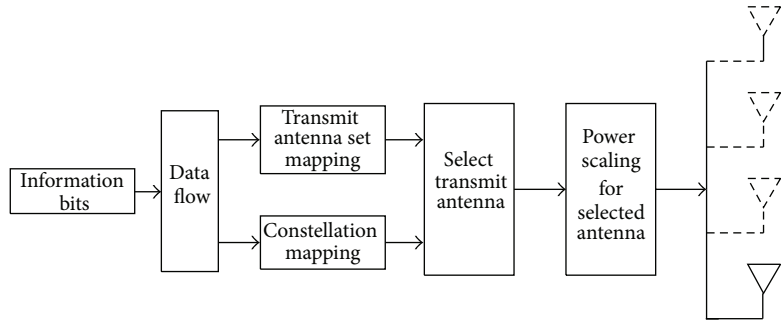

Figure 1: Block diagram of proposed power scaling SM-MIMO system.

Table 1: An SF generation example for 2 × 2 PS-SM.

Index	SF for Tx1	SF for Tx2
1	$\sqrt{0.333}$	$\sqrt{1.667}$
2	$\sqrt{0.667}$	$\sqrt{1.333}$
3	1	1
4	$\sqrt{1.333}$	$\sqrt{0.667}$
5	$\sqrt{1.667}$	$\sqrt{0.333}$

index of the optimal candidate will be delivered to the transmitter.

Figure 2 gives the complementary cumulative distribution functions (CCDF) of the minimum Euclidean distance for a 4 × 2 PS-SM-MIMO and conventional SM-MIMO. It is shown that with the introduction of scaling factor, the minimum Euclidean distance can be enlarged effectively. Moreover, with the increase in feedback amount, the increase in minimum Euclidean distance is more considerable. In this case, the system performance will be effectively improved. The following simulation results will show the benefit of PS-SM to system performance. In this case, the proposed PS-SM is an alternative scheme by overcoming the disadvantage of traditional ASM.

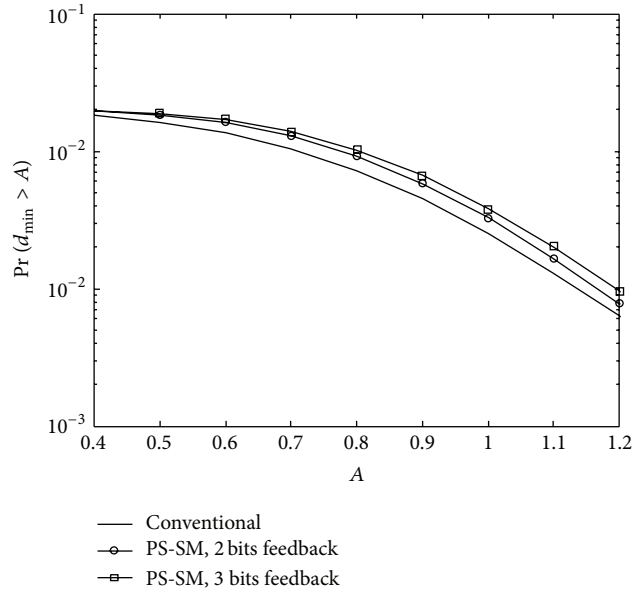

Figure 2: The distribution of minimal Euclidean distance for conventional and proposed methods.

4. Simulation Results

Computer simulation is performed for comparing the system performance of conventional SM, ASM, and PS-SM. We consider an SM-MIMO system with 2 and 4 transmit antennas and QPSK modulation under Rayleigh flat fading channel, so the transmission data rate is 3 and 4 bits per symbol, respectively. The number of receive antennas is 2. Assume that the channel information of Rayleigh flat fading channel is perfectly estimated at the receiver side.

Figure 3 gives the system performance of 2×2 SM-MIMO system. Both ASM, and PS-SM schemes are with 5 candidates for a fair comparison. Firstly, with limited feedback, both ASM and PS-SM outperform conventional SM. For example, at BER of 10^{-3}, there is a 1.7 dB SNR gap between ASM and conventional SM. Furthermore, with the same amount of candidate adaptive sets, the proposed PS-SM outperforms ASM. More specifically, at BER of 10^{-3}, 0.9 dB SNR gain can be achieved by the proposed PS-SM scheme.

Figure 4 shows the comparison of system performance of PS-SM with different amounts of feedback as 1, 2, and 3 bits in which 2, 4, and 8 candidate SF sets are assumed, respectively. The system is with 4 × 2 transceiver configuration and QPSK modulation. It is shown that the performance of PS-SM improves with the increase in the number of feedback bits which is related to the number of factor candidates. At a BER of 10^{-3}, there are 2.5 dB, 3.8 dB, and 4.4 dB performance gains in PS-SM with 1-bit, 2-bit, and 3-bit feedback, respectively. In this case, a feedback of 2 bits gives a better tradeoff between feedback amount and system performance.

Since PS-SM can effectively enlarge the minimum Euclidean distance, the equivalent transmit power is also enlarged. In this part, we consider a tradeoff between system performance and energy-efficient minimum power transmission (Figure 5). A power attenuation factor is introduced to normalize the enlarged minimum Euclidean distance to original SM. In this case, we keep the same system performance to traditional SM while minimizing the transmit power for improving the energy efficiency. A PS-SM with different

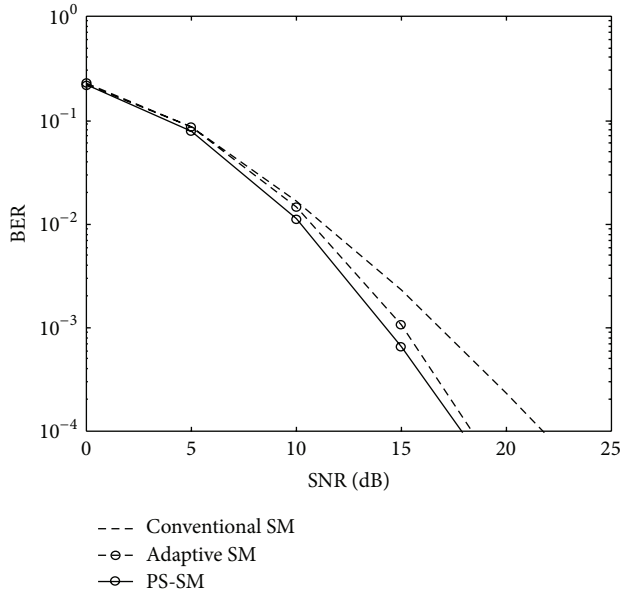

Figure 3: Performance comparison of SM, ASM, and PS-SM on 2×2 MIMO channels.

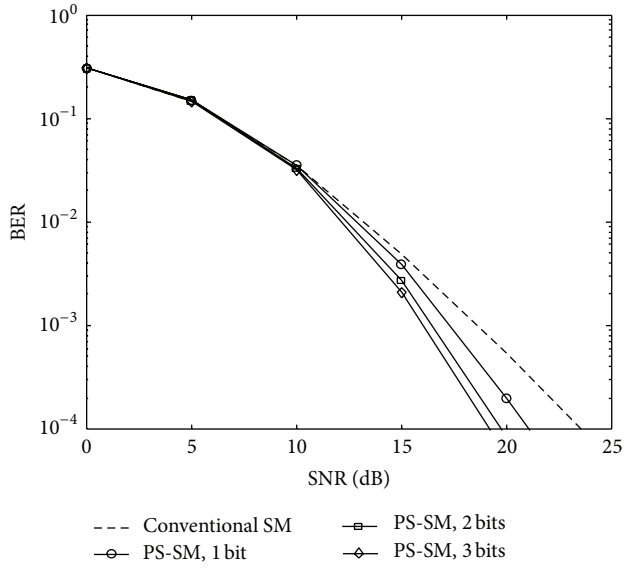

Figure 4: Performance of PS-SM with different feedback amounts on 4 × 2 MIMO channels.

amounts of feedback as 1, 2, and 3 bits in which 2, 4, and 8 candidate SF sets are assumed, respectively. The system is with 4 × 2 transceiver configuration and QPSK modulation. A PS-SM with different amounts of feedbacks as 1, 2, and 3 bits are assumed, with 2, 4, and 8 candidates SF sets respectively. Furthermore, energy saving of 0.4 dB, 1.5 dB, and 2.2 dB is achieved with feedback amounts of 1, 2, and 3 bits, respectively.

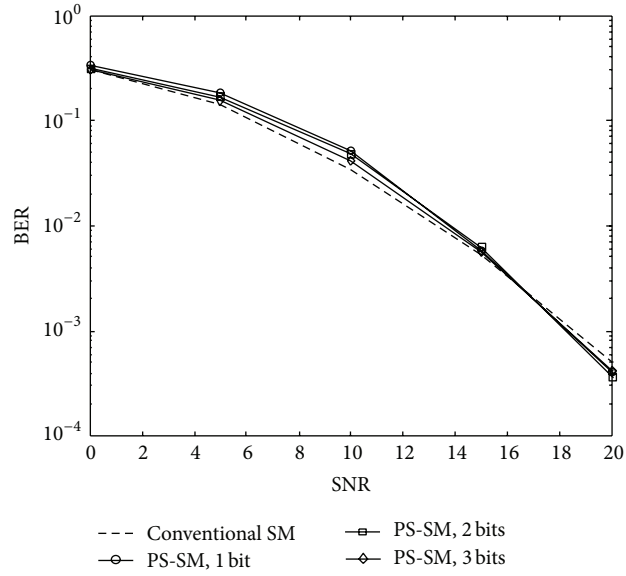

Figure 5: Performance of PS-SM with minimum transmit power.

5. Conclusions

For overcoming the disadvantages of original ASM schemes, a novel power scaling spatial modulation scheme was proposed as an alternative adaptive SM-MIMO scheme with limited feedback. In PS-SM, multiple candidate scaling factor sets are introduced for weighting the modulated symbols on each transmit antenna, so as to enlarge the minimal Euclidean distance and improve the system performance. Simulation results showed that the proposed PS-SM outperforms ASM schemes with the same feedback amount on similar computational complexity.

Acknowledgments

This work was supported in part by the National Science Foundation of China under Grant no. 61101101, the National High-Tech R&D Program of China ("863" Project under Grant no. 2011AA01A105), and the Foundation Project of National Key Laboratory of Science and Technology on Communications under Grant 9140C020404110C0201.

References

[1] R. Mesleh, H. Haas, S. Sinanovic, C. W. Ahn, and S. Yun, "Spatial modulation," *IEEE Transactions on Vehicular Technology*, vol. 57, no. 4, pp. 2228–2241, 2008.

[2] J. Fu, C. Hou, W. Xiang, L. Yan, and Y. Hou, "Generalised spatial modulation with multiple active transmit antennas," in *Proceedings of the IEEE Globecom Workshops (GC '10)*, pp. 839–844, December 2010.

[3] P. Yang, Y. Xiao, B. Zhou, and S. Li, "Initial performance evaluation of spatial modulation OFDM in LTE-based systems," in *Proceedings of the 6th International ICST Conference on Communications and Networking in China (CHINACOM '11)*, pp. 102–107, August 2011.

[4] J. Jeganathan, A. Ghrayeb, and L. Szczecinski, "Spatial modulation: optimal detection and performance analysis," *IEEE Communications Letters*, vol. 12, no. 8, pp. 545–547, 2008.

[5] Q. Tang, Y. Xiao, P. Yang, Q. Yu, and S. Li, "A new low-complexity near-ML detection algorithm for spatial modulation," *IEEE Wireless Communications Letters*, no. 2, pp. 1–4, 2012.

[6] C. Xu, S. Sugiura, S. Ng, and L. Hanzo, "Spatial modulation and space-time shift keying: optimal performance at a reduced detection complexity," *IEEE Transactions on Communications*, vol. 61, no. 1, pp. 206–216, 2013.

[7] P. Yang, Y. Xiao, L. Li, Q. Tang, and S. Li, "An improved matched-filter based detection algorithm for space-time shift keying systems," *IEEE Signal Processing Letters*, vol. 19, no. 5, pp. 271–274, 2012.

[8] P. Yang, Y. Xiao, Y. Yu, and S. Li, "Adaptive spatial modulation for wireless mimo transmission systems," *IEEE Communications Letters*, vol. 15, no. 6, pp. 602–604, 2011.

[9] P. Yang, Y. Xiao, L. Li, Q. Tang, Y. Yu, and S. Li, "Link adaptation for spatial modulation with limited feedback," *IEEE Transactions on Vehicular Technology*, vol. 61, no. 8, pp. 3808–3813, 2012.

Hindawi Publishing Corporation
International Journal of Antennas and Propagation
Volume 2013, Article ID 589591, 11 pages
http://dx.doi.org/10.1155/2013/589591

Research Article

Energy Efficiency Maximization through Cooperative Transmit and Receive Antenna Selection for Multicell MU-MIMO System

Yanjie Dong,[1,2] Yinghai Zhang,[1] Weidong Wang,[1] Gaofeng Cui,[1] and Yang Yu[1]

[1] *Key Laboratory of Universal Wireless Communication of Ministry of Education, Beijing University of Posts and Telecommunications, Beijing 100876, China*
[2] *China Mobile Design Institute, Beijing 100876, China*

Correspondence should be addressed to Yanjie Dong; dongyanjie@cmdi.chinamobile.com

Received 10 January 2013; Accepted 9 April 2013

Academic Editor: Mugen Peng

The capacity of Multiple Input Multiple Output (MIMO) system is highly related to the number of active antennas. But as the active antenna number increases, the MIMO system will consume more energy. To maximize the energy efficiency of MIMO system, we propose an antenna selection scheme which can maximize the energy efficiency of BS cluster. In the scheme, ergodic energy efficiency is derived according to large scale channel state information (CSI). Based on this ergodic energy efficiency, we introduce a cost function varied with the number of antennas, in which the effect to the energy efficiency of both the serving BS and the neighbor BS is considered. With this function, we can transform the whole system optimization problem to a sectional optimization problem and obtain a suboptimal antenna set using a heuristic algorithm. Simulation results verify that the proposed approach performs better than the comparison schemes in terms of network energy efficiency and achieves 98% network energy efficiency of the centralized antenna selection scheme. Besides, since the proposed scheme does not need the complete CSI of the neighbor BS, it can effectively reduce the signaling overhead.

1. Introduction

Due to the challenge of global climate change, reducing carbon dioxide emissions is of high priority for industries. In wireless communications, "green communication" is highly appreciated by many research bodies, which aims to improve the network energy efficiency [1]. Researchers proposed a lot of energy-saving methods on different levels of the wireless network, such as application of new power source, development of lower power consumption device, improvement of network framework, and energy-saving mode of network node [2]. Base station (BS) is one of the most important nodes in wireless network, and it consumes 60–80 percent [2] of the whole network's power. Thus, how to improve the energy efficiency of the BS is the key to realize energy saving of the wireless network.

The existing techniques about BS energy saving can be divided into two categories. One is based on OFDMA [3], and the other is based on Multiple Input Multiple Output (MIMO). For the former, one carrier can only be allocated to one single user, while it can be allocated to multiple users for the latter. We also call it as "MU-MIMO" when multiple users use the same carrier. MU-MIMO technology can improve the system capacity without increasing the system power consumption and carrier bandwidth. So MU-MIMO is regarded as one of the key technologies of IMT-Advanced by 3GPP [4–6] and IEEE 802.16 m. In this paper, we focus on the energy efficiency of MU-MIMO systems.

According to the definition of energy efficiency [7], it is mainly restricted by two factors in MU-MIMO system. One is the system capacity; the other is the system power consumption. The capacity of MU-MIMO system is affected by many factors, such as the distance between user and BS, the number of data stream, antenna beam-forming gain, and number of users. For the single cell MU-MIMO system, the system capacity grows as the number of transmit antenna increases. But in multiple cell system, it is not always the truth because of the interference caused by transmit antennas of the neighbor cells. Besides, the system power consumption increases with the growth of transmit antennas. This paper

focuses on how to maximize the system energy efficiency by selecting the transmitting antennas and the serving users in multiple cell systems.

1.1. Related Work. MIMO system can effectively improve link quality or increase system capacity. The performance of polarized MIMO is investigated in [8]. However, the deployment of MIMO system requires a high digital signal processing (DSP) ability of the BS which is equipped with a mass of radio circuit. In order to achieve the gains of MIMO system in an economic and less complex way, the application of antenna selection technique has attracted significant attention in recent years. The work in [9, 10] analyzes the impact of antenna selection in MIMO system. In [11, 12], low-complexity transmit antenna selection is investigated, and [11] proposes an inverse matrix update method which greatly reduces the matrix operation complexity of transmit antenna selection. In [13–15], receive antenna selection schemes are investigated when the number of transmit antenna is fixed. The work in [13] proposes a low-complexity scheme based on the capacity/channel norm. In order to improve system capacity further, the work in [16] proposes a joint transmit and receive antenna selection strategy. In [17], the performance of transmit and receive antenna selection based on bit error rate in flat fading channel is analyzed. However, these schemes mentioned previously are based on single BS scenario without considering the influence of interference from neighbor BSs. Reference [18] uses statistical information of neighbor BSs on transmit antenna set selection to avoid vast signaling exchanges among neighbor BSs. In [19], a coordinated beamforming method is given for downlink multicell MIMO network. However, all of these previous researches are based on the assumption that the BS can use all the available radio circuit to maximize system capacity or minimize link error probability. This assumption does not consider the power consumption and cannot ensure the maximization of the BS energy efficiency.

In [20], taking into account both the transmit power and power consumed by circuits, energy efficiency problem of MIMO system based on short range communication (SRD) is investigated. The authors in [20] show that the energy efficiency of MIMO system would be greater than that of SISO system only if a combination of adaptive modulation techniques and MIMO techniques is used. The work in [21] analyzes the impact of the spatial diversity on energy efficiency and concludes that antenna selection is in general the most energy efficient option for MIMO systems. In [22], a power amplifier selection scheme is given to improve the energy efficiency. The work in [23] analyzes the impact of antenna selection on improving the energy efficiency. In [24], system energy efficiency is improved through antenna selection for downlink broadcast channel. The impact of transmit antenna selection on energy efficiency in distributed antenna systems (DASs) is analyzed in [25]. The work in [26] investigates the problem of user selection and power allocation to maximize energy efficiency. In [27], energy efficiency is maximized through joint optimization of transmit power, number of transmit antennas, and transmit/receive antenna sets. However, these researches mentioned previously are all based on single-cell scenario and do not consider the impact of the number of transmit antennas and the active receive antenna set on the energy efficiency. The work in [28] proposes an energy efficient coordinated beamforming method for clustered MIMO network. The work in [29] maximizes network energy efficiency through BS transmit antenna selection and transmission mode selection. However, since this method is based on interference nulls and uses ergodic search strategy and considers the three-cell single-user scenario, the computation complexity will be very high when the number of BSs increases, and it cannot be applied to multiuser scenario.

1.2. Contribution. In this paper, we focus on transmit and receive antenna selection for multicell MU-MIMO system to maximize the system energy efficiency. The main contribution of our work can be summarized as follows.

1.2.1. Ergodic Energy Efficiency Based on Large Scale CSI. We derive the available ergodic energy efficiency obtained by BS. This ergodic energy efficiency is only related to the number of BS transmit antenna and large scale CSI between the UE and its severing BS.

1.2.2. Transmit and Receive Antenna Selection Scheme Based on Maximizing the Energy Efficiency of BS Cluster. Based on the ergodic energy efficiency, we introduce a cost function of transmit and receive antenna selection. This cost function consists of two parts: one part is ergodic energy efficiency of the target BS; the other is energy efficiency change of neighbor BSs after the number of transmit antennas of the target BS changes. With this function, we can convert the global optimization of overall system energy efficiency to local optimization problem based on the maximization of BS cluster energy efficiency. Then we develop a heuristic transmit and receive antenna selection algorithm to solve the problem. Since ergodic energy efficiency is only related to the number of BS transmit antennas and large scale CSI between the UE and its severing BS, the proposed scheme can effectively reduce the signaling overhead among different BSs.

1.3. Organization. The remainder of this paper is organized as follows. Section 2 describes the system model. Section 3 derives ergodic energy efficiency and develops a heuristic transmit and receive antenna selection scheme based on this term. Section 4 gives simulation results and analysis. Finally, conclusions are drawn in Section 5.

In this paper, $\mathbf{A}^H$, $|\mathbf{A}|$, $\|\mathbf{A}\|_F^2$, and $\mathbf{A}^{-1}$ express the Hermitian transpose, determinant, Frobenius norm, and inverse of matrix $\mathbf{A}$, respectively. The expectation operator is denoted by $E\{\cdot\}$.

2. System Model

In this paper, we consider a downlink multicell MU-MIMO system model which consists of a cellular network with J cells; each cell consists of K_i users. We assume that each cell has

one BS consisting of $N_{\max}$ transmit antennas, and each user is equipped with single antenna. Although $N_{\max}$ is assumed to be the same for different BSs, it can vary according to the type of individual BS. And each user can only be served by one BS. Partial CSI is shared among BSs; that is, BS can obtain the CSI between itself and its serving users and users it interferes with. The received signal of user k can be expressed as

$$y_{k,i} = \sqrt{\frac{\rho_{k,i}}{M_i}}\mathbf{H}_{k,i}\mathbf{W}_{k,i}\mathbf{x}_{k,i} + \sqrt{\frac{\rho_{k,i}}{M_i}}\sum_{k\neq l}^{K_i}\mathbf{H}_{k,i}\mathbf{W}_{l,i}\mathbf{x}_{l,i} + \sum_{i\neq j,j=1}^{J}\sum_{\bar{k}=1}^{K_j}\sqrt{\frac{\rho_{k,j}}{M_j}}\mathbf{H}_{k,j}\mathbf{W}_{\bar{k},j}\mathbf{x}_{\bar{k},j} + \mathbf{n}_{k,i}, \tag{1}$$

where $\rho_{k,i} = P/L_{k,i}$, $L_{k,i}$ is the path loss between user k and BSi, P is the overall BS transmit power, M_i is the number of transmit data streams of BSi, which can be different according to i, and $\mathbf{x}_{k,i}$ is the transmit signal of user k. We assume that different data streams adopt the same transmit power; that is, $E\{\mathbf{x}_{k,i}\mathbf{x}_{k,i}^{\mathbf{H}}\} = 1$. $\mathbf{H}_{k,i}$ denotes the small scale fading between user k and BSi, the fading coefficients in $\mathbf{H}_{k,i}$ are i.i.d. with zero-mean and variance 1, $\mathbf{W}_{k,i} \in C^{N_i\times 1}$ is the precoding matrix of user k, $\|\mathbf{W}_{k,i}\|_F^2 = 1$, N_i ($N_i \leq N_{\max}$) is the transmit antenna activated by BSi, and $\mathbf{n}_{k,i}$ is additive white Gaussian noise (AWGN) with zero-mean and variance 1. The second term on the right side of the equal sign in formula (1) is interuser interference (IUI), and the third term is intercell interference (ICI).

Assuming that Zero Forcing Beamforming (ZFBF) [30] is adopted to eliminate IUI, the direction of user k's precoding vectors must be the same as the projections of $\mathbf{H}_{k,i}$ on the null space of $\overline{\mathbf{H}} = [\mathbf{H}_{1,i}^{\mathbf{H}}, \mathbf{H}_{2,i}^{\mathbf{H}}, \mathbf{H}_{k-1,i}^{\mathbf{H}}, \mathbf{H}_{k+1,i}^{\mathbf{H}}, \mathbf{H}_{K_i,i}^{\mathbf{H}}]^{\mathbf{H}}$. Thus, the normalized $\mathbf{W}_{k,i}$ can be expressed as

$$\mathbf{W}_{k,i} = \left(\mathbf{I} - \overline{\mathbf{H}}^{\mathbf{H}}\left(\overline{\mathbf{H}}\,\overline{\mathbf{H}}^{\mathbf{H}}\right)^{-1}\overline{\mathbf{H}}\right)\mathbf{H}_{k,i}, \tag{2}$$

where, $\mathbf{I} \in C^{N_i\times N_i}$ is an identity matrix.

After the IUI has been eliminated, (1) can be rewritten as

$$y_{k,i} = \sqrt{\frac{\rho_{k,i}}{M_i}}\mathbf{H}_{k,i}\mathbf{W}_{k,i}\mathbf{x}_{k,i} + \sum_{i\neq j,j=1}^{J}\sum_{\bar{k}=1}^{K_j}\sqrt{\frac{\rho_{k,j}}{M_j}}\mathbf{H}_{k,j}\mathbf{W}_{\bar{k},j}\mathbf{x}_{\bar{k},j} + \mathbf{n}_{k,i}. \tag{3}$$

Therefore, the received signal to interference plus noise (SINR) can be expressed as

$$\mathrm{SINR}_{k,i} = \frac{\left(\rho_{k,i}/M_i\right)\mathbf{H}_{k,i}\mathbf{W}_{k,i}\mathbf{W}_{k,i}^{\mathbf{H}}\mathbf{H}_{k,i}^{\mathbf{H}}}{1 + \sum_{j=1,i\neq j}^{J}\sum_{\bar{k}=1}^{K_j}\left(\rho_{k,j}/M_j\right)\mathbf{H}_{k,j}\mathbf{W}_{\bar{k},j}\mathbf{W}_{\bar{k},j}^{\mathbf{H}}\mathbf{H}_{k,j}^{\mathbf{H}}}. \tag{4}$$

The ergodic capacity of single user can be expressed as

$$C_{k,i} = E\left[B\log_2\left(1 + \mathrm{SINR}_{k,i}\right)\right]. \tag{5}$$

Thus, the system ergodic capacity for J BSs can be obtained as

$$C = \sum_{i=1}^{J}\sum_{k=1}^{M_i}C_{k,i}. \tag{6}$$

Furthermore, the power consumption of BSs can be formulated as [7]

$$P_{\mathrm{total},i}\left(N_i, P, B\right) = \frac{P}{\eta} + P_D + P_S, \tag{7}$$

where P is the transmit power of BS, η is the amplifier efficiency, P_D is the dynamic power of BS, which is determined by the number of transmit antennas and bandwidth, $P_D = N_iP_{\mathrm{cir}} + BP_{\mathrm{ac}} + N_iP_{\mathrm{sp,bw}}B$, P_{cir} is the power consumed in circuits, P_{ac} is the power consumed by A/D converter, $P_{\mathrm{sp,bw}}$ is the power consumed by the signal processing unit, B is the system bandwidth, and P_S is the static power of BS which consists of power consumption such as air-condition and power supply.

The network energy efficiency (NEE) can be defined as [29]

$$\mathrm{NEE} = \frac{\sum_{i=1}^{J}\sum_{k=1}^{M_i}C_{k,i}}{\sum_{i=1}^{J}P_{\mathrm{total},i}\left(N_i, P, B\right)}. \tag{8}$$

The maximization problem of system NEE can be expressed as

$$\max_{\substack{\{N_i\}\{M_i\}\\ \Omega_{T,i},\Omega_{R,i}}}\left\{\frac{\sum_{i=1}^{J}\sum_{k=1}^{M_i}C_{k,i}}{\sum_{i=1}^{J}P_{\mathrm{total},i}\left(N_i, P, B\right)}\right\}$$
$$\text{subject to}\begin{cases}1 \leq N_i \leq N_{\max}\\ 1 \leq M_i \leq N_i\\ \Omega_{T,i} \subseteq \Phi_{T,i}\\ \Omega_{R,i} \subseteq \Phi_{R,i},\end{cases} \tag{9}$$

where $\Omega_{T,i}$ denotes the set of transmit antennas activated by BSi, $\Phi_{T,i}$ is the transmit antenna set of BSi, $\Omega_{R,i}$ is the set of activated receive antennas of users served by BSi, and $\Phi_{R,i}$ is the receive antenna set of users served by BSi.

3. Transmit and Receive Antenna Selection Scheme Based on Maximizing the Energy Efficiency of BS Cluster

From (9), we can find that NEE relates to the capacity and power consumption of all the BSs in the network. Especially for the available capacity, it is determined by not only its selection of transmit and receive antenna sets, but also its neighbor BSs' selection of transmit and receive antenna sets. The latter influences the interference suffered by its serving users. Therefore, maximization of NEE is a nonconvex problem. In order to resolve this problem, we first derive ergodic energy efficiency based on large scale CSI. Then a transmit and receive antenna selection strategy based on cost function is proposed to leverage this ergodic energy efficiency.

3.1. Ergodic Energy Efficiency Based on Large Scale CSI. Since each user is equipped with single antenna and $\mathbf{H}_{k,i}\mathbf{W}_{k,i}\mathbf{W}_{k,i}^{\mathbf{H}}\mathbf{H}_{k,i}^{\mathbf{H}} = \|\mathbf{H}_{k,i}\mathbf{W}_{k,i}\|_F^{\mathbf{2}}$ in (4), $\mathrm{SINR}_{k,i}$ can be rewritten as

$$\begin{aligned}\mathrm{SINR}_{k,i} &= \frac{\left(\rho_{k,i}/M_i\right)\left\|\mathbf{H}_{k,i}\mathbf{W}_{k,i}\right\|_F^2}{1+\sum_{j=1,i\neq j}^{J}\sum_{\bar{k}=1}^{M_j}\left(\rho_{k,j}/M_j\right)\left\|\mathbf{H}_{k,j}\mathbf{W}_{\bar{k},j}\right\|_F^2} \\ &= \frac{\left(\rho_{k,i}/M_i\right)\left\|\mathbf{H}_{k,i}\mathbf{W}_{k,i}\right\|_F^2}{1+\sum_{j=1,i\neq j}^{J}\left(\rho_{k,j}/M_j\right)\sum_{\bar{k}=1}^{M_j}\left\|\mathbf{H}_{k,j}\mathbf{W}_{\bar{k},j}\right\|_F^2}.\end{aligned} \tag{10}$$

In (10), because $\mathbf{W}_{k,i}$ belongs to the null space of the channel set of the other serving users in the same cell, $\|\mathbf{H}_{k,i}\mathbf{W}_{k,i}\|_F^2$ obeys Chi-square distribution with degree of freedom $2(N_i-(M_i-1))$, that is, $\|\mathbf{H}_{k,i}\mathbf{W}_{k,i}\|_F^2 \sim \chi^2_{2(N_i-(M_i-1))}$, where M_i is the number of data streams. Since $\mathbf{W}_{\bar{k},j}$ is uncorrelated with $\mathbf{H}_{k,j}$,$\|\mathbf{H}_{k,j}\mathbf{W}_{\bar{k},j}\|_F^2 \sim \chi_2^2$ is independent with the number of data streams. From the above mentioned, when the BS adopts ZFBF to implement beamforming, useful signal strength can be regarded as random variable which obeys Chi-square distribution with degree of freedom $2(N_i-(M_i-1))$, and the signal strength of interferences from the neighbor cells can be regarded as random variable which obeys Chi-square distribution with degree of freedom 2. Defining $Z_{k,i} = \|\mathbf{H}_{k,i}\mathbf{W}_{k,i}\|_F^2$ and $Y_{k,j,\bar{k}} = \|\mathbf{H}_{k,j}\mathbf{W}_{\bar{k},j}\|_F^2$, where $Z_{k,i}$ and $Y_{k,j,\bar{k}}$ are mutually independent, $Z_{k,i} \sim \chi^2_{2(N_i-(M_i-1))}$ and $Y_{k,j,\bar{k}} \sim \chi_2^2$, (10) can be rewritten as

$$\begin{aligned}\mathrm{SINR}_{k,i} &= \frac{\left(\rho_{k,i}/M_i\right)Z_{k,i}}{1+\sum_{j=1,i\neq j}^{J}\left(\rho_{k,j}/M_j\right)\sum_{\bar{k}=1}^{M_j}Y_{k,j,\bar{k}}} \\ &\leq \frac{\left(\rho_{k,i}/M_i\right)Z_{k,i}}{1+\sum_{j=1,i\neq j}^{J}\left(\rho_{k,j}/N_{\max}\right)Y_{k,j,\bar{k}}}.\end{aligned} \tag{11}$$

When users suffer weaker interference from neighbor cells, the upper bound of $\mathrm{SINR}_{k,i}$ in (11) is tight. Defining $\alpha_{k,i} = \rho_{k,i}/M_i$, $\beta_{k,j} = \rho_{k,j}/N_{\max}$ and $Y_{k,j} = Y_{k,j,\bar{k}}$, $X_{k,i}$ can be expressed as

$$X_{k,i} = \frac{\alpha_{k,i}Z_{k,i}}{1+\sum_{j=1,i\neq j}^{J}\beta_{k,j}Y_{k,j}}. \tag{12}$$

Thus, the ergodic capacity of single user can be expressed as

$$\begin{aligned}C_{k,i}\left(\alpha_{k,i},\beta_{k,j},N_i,M_i,B\right) &\leq E\left[B\log_2\left(1+X_{k,i}\right)\right] \\ &= E\left[B\log_2(e)\ln\left(1+X_{k,i}\right)\right] \\ &= B\log_2(e)\,E\left[\ln\left(1+X_{k,i}\right)\right].\end{aligned} \tag{13}$$

Then, the upper bound of network capacity can be expressed as

$$\overline{C}_{k,i}\left(\alpha_{k,i},\beta_{k,j},N_i,M_i,B\right) = B\log_2(e)\,E\left[\ln\left(1+X_{k,i}\right)\right]. \tag{14}$$

Theorem 1. (1) *When* $J = 1$,

$$\begin{aligned}&\overline{C}_{k,i}\left(\alpha_{k,i},\beta_{k,j},N_i,M_i,B\right) \\ &\quad= B\log_2(e)\sum_{r=0}^{N_i-M_i}\sum_{l=0}^{r}\frac{\left(\alpha_{k,i}\right)^{l+1-r}}{\beta_{k,1}(r-l)!}I_1\left(\frac{1}{\alpha_{k,i}},\frac{\alpha_{k,i}}{\beta_{k,1}},r,l+1\right).\end{aligned} \tag{15}$$

(2) *When* $J = 2$,

$$\begin{aligned}&\overline{C}_{k,i}\left(\alpha_{k,i},\beta_{k,j},N_i,M_i,B\right) \\ &\quad= B\log_2(e)\sum_{r=0}^{N_i-M_i}\sum_{l=0}^{r}\frac{\left(\alpha_{k,i}\right)^{l+1-r}}{\left(\beta_{k,1}-\beta_{k,2}\right)(r-l)!} \\ &\qquad\times\left[I_1\left(\frac{1}{\alpha_{k,i}},\frac{\alpha_{k,i}}{\beta_{k,1}},r,l+1\right)-I_1\left(\frac{1}{\alpha_{k,i}},\frac{\alpha_{k,i}}{\beta_{k,2}},r,l+1\right)\right],\end{aligned} \tag{16}$$

where $I_1(a,b,c,d)$ *is an integral function [31].*

Proof. The proof procedure can be found in [31]. □

Theorem 2. *When* $J = 3$,

$$\begin{aligned}&\overline{C}_{k,i}\left(\alpha_{k,i},\beta_{k,j},N_i,M_i,B\right) \\ &\quad= B\log_2(e)\sum_{r=0}^{N_i-M_i}\sum_{l=0}^{r}\frac{\left(\alpha_{k,i}\right)^{l+1-r}}{(r-l)!} \\ &\qquad\times\left[\begin{array}{l}\dfrac{\beta_{k,1}}{\left(\beta_{k,1}-\beta_{k,2}\right)\left(\beta_{k,1}-\beta_{k,3}\right)}I_1\left(\dfrac{1}{\alpha_{k,i}},\dfrac{\alpha_{k,i}}{\beta_{k,1}},r,l+1\right) \\ -\dfrac{\beta_{k,2}}{\left(\beta_{k,1}-\beta_{k,2}\right)\left(\beta_{k,2}-\beta_{k,3}\right)}I_1\left(\dfrac{1}{\alpha_{k,i}},\dfrac{\alpha_{k,i}}{\beta_{k,2}},r,l+1\right) \\ +\dfrac{\beta_{k,3}}{\left(\beta_{k,1}-\beta_{k,3}\right)\left(\beta_{k,2}-\beta_{k,3}\right)}I_1\left(\dfrac{1}{\alpha_{k,i}},\dfrac{\alpha_{k,i}}{\beta_{k,3}},r,l+1\right)\end{array}\right].\end{aligned} \tag{17}$$

Proof. For the proof, see the Appendix. □

Considering the signal attenuation caused by distance, the users are mainly affected by the interference from the three neighbor BSs. Therefore, this paper only calculates the interference from the three neighbor BSs to the users. For $J > 3$ cases, the upper bound of network capacity can be obtained by the same previous method. From (14), the upper bound of network energy efficiency is

$$\begin{aligned}&\mathrm{NEE}_{\mathrm{upper}}\left(N_i,M_i,B,P\right) \\ &\quad= \frac{\sum_{i=1}^{J}\sum_{k=1}^{M_i}\overline{C}_{k,i}\left(\alpha_{k,i},\beta_{k,j},N_i,M_i,B\right)}{\sum_{i=1}^{J}P_{\mathrm{total},i}\left(N_i,P,B\right)}.\end{aligned} \tag{18}$$

According to the upper bound of network energy efficiency in (18), $\mathrm{NEE}_{\mathrm{upper}}$ is only related to the large scale CSI between BS and its serving users, the number of transmit antennas, and transmit power. Using (18) to implement antenna selection can effectively reduce the signaling overhead caused by the complete CSI sharing among different BSs.

3.2. The Introduction of the Cost Function and the Transmit and Receive Antenna Selection Strategy. Based on (18), we can convert the maximization problem of network energy efficiency in (9) into the maximization problem of the upper bound $\mathrm{NEE}_{\mathrm{upper}}$ of network energy efficiency. Then, (9) can be rewritten as

$$\max_{\substack{\{N_i\}\{M_i\}\\ \Omega_{T,i},\Omega_{R,i}}} \left\{ \frac{\sum_{i=1}^{J}\sum_{k=1}^{M_i}\overline{C}_{k,i}\left(\alpha_{k,i},\beta_{k,j},N_i,M_i,B\right)}{\sum_{i=1}^{J}P_{\mathrm{total},i}\left(N_i,P,B\right)} \right\}$$
$$\text{subject to} \begin{cases} 1 \le N_i \le N_{\max} \\ 1 \le M_i \le N_i \\ \Omega_{T,i} \subseteq \Phi_{T,i} \\ \Omega_{R,i} \subseteq \Phi_{R,i}. \end{cases} \tag{19}$$

It can be drawn from (19) that the average network energy efficiency is mainly related to the transmit and receive antenna sets of each BS, when both the bandwidth and the BS transmit power are fixed. However, before one BS determines the transmit antenna set and serving users of itself, it must know the number of transmit antennas in neighbor cells. To ensure the maximization of network energy efficiency, it is necessary to deploy a central processing unit which can select the transmit antennas and serving users of all the BSs. This problem can be resolved by brute-force complete search, but it will become very complex as the number of transmit antennas and serving users increases. Besides, users' CSI must be shared among all the BSs, which will produce lots of signaling overhead.

In this part, we will take the network energy efficiency difference as cost function. The difference is brought by the change of BS transmit antenna number and data stream number. Assuming that the BS bandwidth and transmit power are fixed, the network energy efficiency is only related to the number of BS transmit antennas and data streams. Then (18) can be expressed as

$$\begin{aligned}\mathrm{NEE}_{\mathrm{upper}}\left(N_i,M_i\right) &= \frac{\sum_{i=1}^{J}\sum_{k=1}^{M_i}\overline{C}_{k,i}\left(\alpha_{k,i},\beta_{k,j},N_i,M_i\right)}{\sum_{i=1}^{J}P_{\mathrm{total},i}\left(N_i\right)} \\ &= \frac{\sum_{k=1}^{M_i}\overline{C}_{k,i}\left(\alpha_{k,i},\beta_{k,j},N_i,M_i\right)}{\sum_{i=1}^{J}P_{\mathrm{total},i}\left(N_i\right)} \\ &\quad + \frac{\sum_{j=1,j\ne i}^{J}\sum_{\bar{k}=1}^{M_j}\overline{C}_{\bar{k},i}\left(\alpha_{\bar{k},i},\beta_{\bar{k},j},N_j,M_j\right)}{\sum_{i=1}^{J}P_{\mathrm{total},i}\left(N_i\right)}.\end{aligned} \tag{20}$$

When the number of BSi' transmit antennas changes from N_i to $N_i + n$, and the number of BSi' data streams changes from M_i to $M_i + m$, while the number of other BS's transmit antennas and data streams stays the same, the network energy efficiency can be expressed as

$$\begin{aligned}&\mathrm{NEE}_{\mathrm{upper}}\left(N_i+n,M_i+m\right) \\ &\quad= \frac{\sum_{i=1}^{J}\sum_{k=1}^{M_i}\overline{C}_{k,i}\left(\alpha_{k,i},\beta_{k,j},N_i+n,M_i+m\right)}{\sum_{i=1}^{J}P_{\mathrm{total},i}\left(N_i\right)} \\ &\quad= \frac{\sum_{k=1}^{M_i}\overline{C}_{k,i}\left(\alpha_{k,i},\beta_{k,j},N_i+n,M_i+m\right)}{\sum_{j\ne i}^{J}P_{\mathrm{total},i}\left(N_j\right)+P_{\mathrm{total},i}\left(N_i+n\right)} \\ &\quad\quad+ \frac{\sum_{j=1,j\ne i}^{J}\sum_{\bar{k}=1}^{M_j}\overline{C}_{\bar{k},i}\left(\alpha_{\bar{k},i},\beta_{\bar{k},j},N_j,M_j\right)}{\sum_{j\ne i}^{J}P_{\mathrm{total},i}\left(N_j\right)+P_{\mathrm{total},i}\left(N_i+n\right)}.\end{aligned} \tag{21}$$

In (14), the changes of the number of one BS's transmit antennas and data streams will not affect the available capacity $\sum_{\bar{k}=1}^{M_j}\overline{C}_{\bar{k},i}$ that can be gotten by its neighbor BSs. Defining $G = \sum_{j=1,j\ne i}^{J}\sum_{\bar{k}=1}^{M_j}\overline{C}_{\bar{k},i}(\alpha_{\bar{k},i},\beta_{\bar{k},j},N_j,M_j)$, then the network energy efficiency difference brought by the change of transmit antenna can be expressed as

$$\begin{aligned}&\mathrm{NEE}_{\mathrm{upper}}\left(N_i+n,M_i+m\right)-\mathrm{NEE}_{\mathrm{upper}}\left(N_i,M_i\right) \\ &\quad= \frac{\sum_{k=1}^{M_i}\overline{C}_{k,i}\left(\alpha_{k,i},\beta_{k,j},N_i+n,M_i+m\right)}{\sum_{j\ne i}^{J}P_{\mathrm{total},i}\left(N_j\right)+P_{\mathrm{total},i}\left(N_i+n\right)} \\ &\quad\quad- \frac{\sum_{k=1}^{M_i}\overline{C}_{k,i}\left(\alpha_{k,i},\beta_{k,j},N_i,M_i\right)}{\sum_{i=1}^{J}P_{\mathrm{total},i}\left(N_i\right)} \\ &\quad\quad+ G\left(\frac{1}{\sum_{j\ne i}^{J}P_{\mathrm{total},i}\left(N_j\right)+P_{\mathrm{total},i}\left(N_i+n\right)}\right. \\ &\quad\quad\left.-\frac{1}{\sum_{i=1}^{J}P_{\mathrm{total},i}\left(N_i\right)}\right) \\ &\quad= \mathrm{CEE}_i\left(N_i+n,M_i+m\right)-\mathrm{CEE}_i\left(N_i,M_i\right)+\Delta\mathrm{CEE}_j.\end{aligned} \tag{22}$$

Defining cost function $S = \mathrm{NEE}_{\mathrm{upper}}(N_i + n, M_i + m) - \mathrm{NEE}_{\mathrm{upper}}(N_i, M_i)$, we have

$$\begin{aligned}S &= \mathrm{NEE}_{\mathrm{upper}}\left(N_i+n,M_i+m\right)-\mathrm{NEE}_{\mathrm{upper}}\left(N_i,M_i\right) \\ &= \mathrm{CEE}_i\left(N_i+n,M_i+m\right)-\mathrm{CEE}_i\left(N_i,M_i\right)+\Delta\mathrm{CEE}_j\left(n\right),\end{aligned} \tag{23}$$

where, $\mathrm{CEE}_i(N_i, M_i) = \sum_{k=1}^{M_i}\overline{C}_{k,i}(\alpha_{k,i},\beta_{k,j},N_i,M_i)/\sum_{i=1}^{J}P_{\mathrm{total},i}(N_i)$

$$\begin{aligned}\Delta\mathrm{CEE}_j\left(n\right) &= G\left(\frac{1}{\sum_{j\ne i}^{J}P_{\mathrm{total},i}\left(N_j\right)+P_{\mathrm{total},i}\left(N_i+n\right)}\right. \\ &\quad\left.-\frac{1}{\sum_{i=1}^{J}P_{\mathrm{total},i}\left(N_i\right)}\right).\end{aligned} \tag{24}$$

In (23), $\mathrm{CEE}_i(N_i + n, M_i + m) - \mathrm{CEE}_i(N_i, M_i)$ and $\Delta\mathrm{CEE}_j(n)$ denote the difference on energy efficiency of target BS itself and the difference on energy efficiency of the other BSs, respectively. We assume that the number of transmit antennas and data streams of neighbor BSs remains unchanged, then G remains unchanged, and $\Delta\mathrm{CEE}_j(n)$ is only related to n.

Based on these properties of (23) mentioned previously, we develop a transmit and receive antenna selection scheme based on the maximization of BS cluster energy efficiency. In this scheme, a BS cluster consists of seven BSs, and each of them implements transmit and receive antenna selection in turn. In this case, it can ensure that the transmit antenna sets and serving user groups of the six neighbor BSs remain unchanged when each BS implements transmit and receive antenna selection, which will avoid the iteration. Each BS first determines its available number of transmit antennas and receive antenna set using a heuristic algorithm and then activates the antennas which will maximize the upper bound of capacity in the transmit antenna set. After determining the transmit and receive antennas of itself, the target BS shares its information of upper limit capacity with its neighbor BSs. Based on this information, the other BSs can calculate their cost function. The transmit and receive antenna selection scheme of a single BS can be summarized in Algorithm 1.

4. Simulation Results

In this section, we present simulation results of our proposed scheme and investigate its performance. In particular, we compare the performance of our scheme with that of single cell CAS, single cell EEAS, and centralized EEAS. For centralized EEAS, each user's complete CSI must be shared among all the BSs, and a central processing unit is needed to implement transmit and receive antenna selection for all the users in the system.

In the simulation, we adopt 7-cell downlink MU-MIMO system model. Each cell uses the same frequency resource. We assume that each BS has N transmit antennas, and each user is equipped with single antenna. Users location obey uniform distribution in the coverage of the BS. The path loss model base on distance is $37.6 \log(d) + 128.1$, and the standard deviation of shadowing is 8 dB. According to energy demands for each parts of the BS, we set $\eta = 0.38$, $P_{\mathrm{cir}} = 66.4$ W, $P_{\mathrm{ac}} = 1.82\,\mu$W/Hz, $P_{\mathrm{sp,bw}} = 3.32\,\mu$W/Hz, $P_S = 36.4$ W, and $B = 5$ MHz.

Figure 1 shows NEE's change as the user number increases. From the figure, the NEE increases with the user number per cell because more multiuser diversity gain is obtained. Since cluster EEAS considers the impact of ICI on NEE, its NEE is much higher than single cell CAS and single cell EEAS. For example, when user number per cell is 16, cluster EEAS can achieve about 13% and 28% NEE gain over the single cell CAS and single cell EEAS. In addition, compared with the centralized EEAS, the proposed scheme has only 2% NEE degradation, but it does not need complete CSI sharing and central processing unit.

Figure 2 shows the NEE versus the cell radius. The simulation keeps the BS transmit power unchanged and

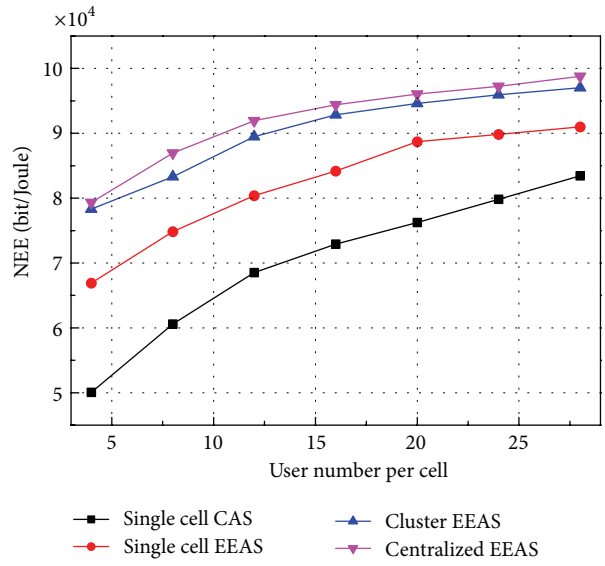

Figure 1: NEE versus User number per cell with $N_{\max} = 4$, $P = 20$ W, and cell radius of 1 Km.

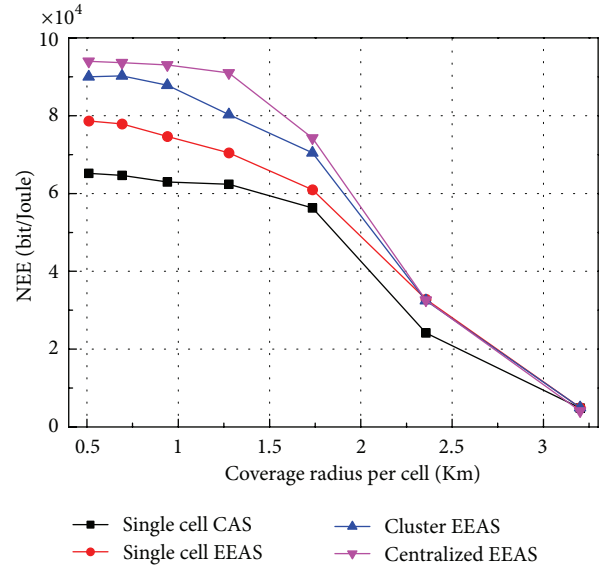

Figure 2: NEE versus Coverage radius per cell with $N_{\max} = 4$, $P = 20$ W, and 10 users per cell.

increases the cell radius from 0.5 Km to 3.5 Km. From this figure, we can see that the NEE decreases with the increase of the cell radius, and when the cell radius is greater than 1.5 Km, NEE decreases faster. While for the cell radius less than 1.5 Km, the capacity decreases less with the increase of the cell radius. This is mainly because that the impact of path loss on SNR is aggravated when the cell radius is large. Besides, when the cell radius is large enough, these four schemes almost obtain the same EEAS. This is mainly because when the cell radius increases, the ICI will recede. On this occasion, the useful signal strength becomes the major influencing factor on NEE, and the gain of cluster EEAS recedes. Thus it can be

Initialization:
The neighbor cells share their available upper limit capacity G. $\mathrm{CEE}_i(0,0) = 0$, the inactive transmit antenna set is $\Phi_{T,i} = \{1, 2, \ldots, N_{\max}\}$, the activated transmit antenna set is $\Omega_{T,i} = \emptyset$, the inactive receive antenna set is $\Phi_{R,i} = \{1, 2, \ldots, K_i\}$, and the activated transmit antenna set is $\Omega_{R,i} = \emptyset$.
Step1: **the number of transmit antenna determination and receive antenna set selection**
For $n = 1 : N_{\max}$
(a) For $m = 1 : n$
(1) $\mathrm{CEE}_i(n, 0) = 0$, $\Omega_{R,i} = \emptyset$
(2) For receive antenna k, set $\Omega_{R,i} = \Omega_{R,i} + \{k\}$, and calculate the available energy efficiency $\mathrm{CEE}_{i,k}(n, m)$.
(3) Find the k corresponding to the maximum of $\mathrm{CEE}_{i,k}(n, m)$
(4) Calculate the cost function $S = \mathrm{CEE}_i(n, m) - \mathrm{CEE}_i(n, m-1) + \Delta\mathrm{CEE}_j(n)$
(5) if $S > 0$, $\Omega_{R,i} = \Omega_{R,i} + \{k\}$, $\mathrm{CEE}_{\mathrm{temp},i} = \mathrm{CEE}_i(n, m)$, otherwise turn to (b)
End
(b) Calculate the cost function $S = \mathrm{CEE}_{\mathrm{temp},i}(n, m) - \mathrm{CEE}_{\mathrm{temp}} + \Delta\mathrm{CEE}_j(n)$
(c) if $S > 0$, set $\mathrm{CEE}_{\mathrm{temp}} = \mathrm{CEE}_{\mathrm{temp},i}(n, m)$, $N_i = N_i + 1$, otherwise stop
end
Step2: **transmit antenna set selection**
For $l = 1 : C_{N_{\max}}^{N_i}$
(a) For any transmit antenna set $\Omega_{T,i}(l)$, calculate the available energy efficiency $\mathrm{CEE}_{i,l}(N_i, M_i)$ according to the selected receive antenna set $\Omega_{R,i}$.
(b) Find the transmit antenna set $\Omega_{T,i}(l)$ corresponding to the maximum of $\mathrm{CEE}_{i,l}(N_i, M_i)$
end

Algorithm 1: Cluster energy efficiency based antenna selection (cluster EEAS).

seen that cluster performs much better in high interference scenario.

The NEE versus the transmit power of BS is shown in Figure 3. On this occasion, there are two main effect factors of NEE: the capacity which can be obtained by the cell and BS transmit power. From this figure, we can see that NEE increases with the growth of the transmit power, but when the BS transmit power is greater than 30 dBm, NEE decreases quickly. This proves that the increase of the BS transmit power cannot always bring the growth of BS NEE. Besides, when the BS transmit power is greater than 30 dBm, the scheme considering energy efficiency decreases faster than the CAS in NEE. This illustrates that in the schemes considering energy efficiency, the increase of the BS transmit power cannot always bring the increase of cell capacity.

The NEE versus the maximal transmit antenna number of BS is shown in Figure 4. For the CAS of capacity maximum, NEE decreases with the increase of the maximal transmit antenna number. This is mainly because all the transmit antennas have been activated to gain high capacity in this scheme, but more transmit antennas mean more energy consumed by BSs. If the capacity gains brought by activating more transmit antennas cannot compensate the impact of power consumption on NEE, NEE will decrease. In this simulation scenario, activating more transmit antenna goes against the improvement of network NEE obviously. However, for the schemes which consider the NEE, NEE will not decrease with the increase of the maximal transmit antenna number. That is because that the transmit antenna will not be activated when it does not increase NEE in the proposed scheme.

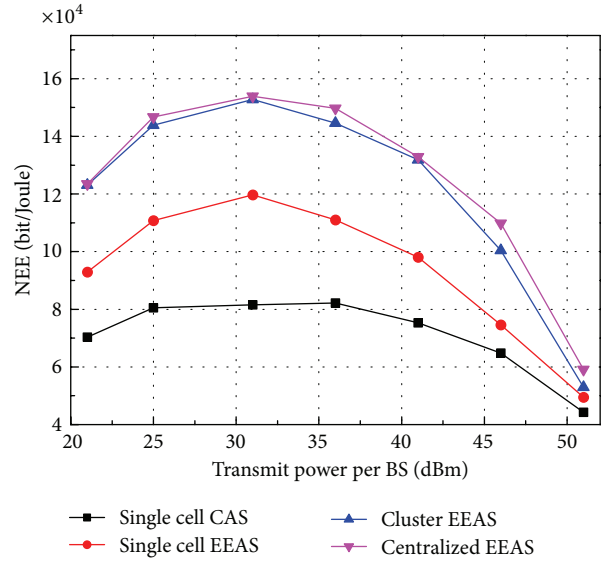

Figure 3: NEE versus transmit power per BS with $N_{\max} = 4$, 10 user per cell and cell radius of 1 Km.

Compared with single cell CAS and single cell EEAS, cluster EEAS needs the users to feedback the large scale CSI of interfering channels between users and its interfering BSs. Moreover, a centralized entity is needed to make the BSs in a cluster maximize the energy efficiency in turn. Whereas, centralized EEAS needs a centralized entity to select the

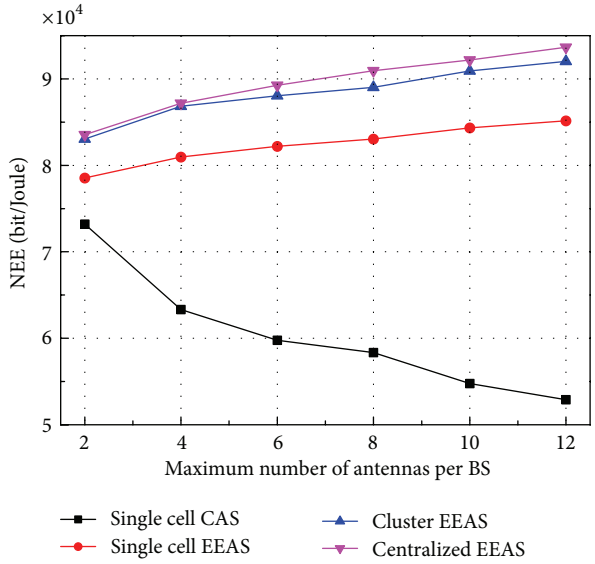

FIGURE 4: NEE versus maximum number of antennas per BS with $P = 20$ W, 10 users per cell, and cell radius of 1 Km.

transmit and receive antenna sets cooperatively. And it needs complete CSI sharing that will bring large amount of signaling overhead. Furthermore, the four algorithms have the same computation complexity.

5. Conclusion

This paper analyzes the available network energy efficiency through transmit and receive antenna selection for multicell MU-MIMO system. In this paper, we first deduce an ergodic energy efficiency based on large scale CSI. Based on this energy efficiency, we introduce a cost function of transmit and receive antenna selection and convert the transmit and receive antenna selection problem to local optimization problem based on the maximization of BS cluster energy efficiency. Then, we propose a antenna selection scheme based on cluster energy efficiency (cluster EEAS). The simulation results show that the proposed scheme performs better network energy efficiency compared to the single cell CAS and single cell EEAS and can achieve about 98% NEE of the centralized EEAS. Besides, since the proposed scheme uses large scale CSI to implement antenna selection and do not need the complete CSI of neighbor cells' users, it can effectively reduce the signaling overhead brought by the exchange of CSI.

Appendix

When $J = 3$, (12) can be expressed as

$$X_{k,i} = \frac{\alpha_{k,i} Z_{k,i}}{1 + \beta_{k,1} Y_{k,1} + \beta_{k,2} Y_{k,2} + \beta_{k,3} Y_{k,3}}. \tag{A.1}$$

In order to obtain the distribution function of $X_{k,i}$, first we need to obtain the probability density function of $\beta_{k,1} Y_{k,1} + \beta_{k,2} Y_{k,2} + \beta_{k,3} Y_{k,3}$. For the sake of convenience in writing, we omit the subscript in (A.1), then (A.1) can be rewritten as

$$X = \frac{\alpha Z}{1 + \beta_1 Y_1 + \beta_2 Y_2 + \beta_3 Y_3}. \tag{A.2}$$

The probability density function of Chi-square distribution with degree of freedom $2M$ is

$$f(x) = \frac{x^{M-1} e^{-x/r_1}}{(M-1)! r_1^M}. \tag{A.3}$$

The probability density function of Chi-square distribution with degree of freedom 2 is,

$$f(x) = \frac{e^{-x/r_1}}{r_1}. \tag{A.4}$$

Define $\overline{Y} = \beta_1 Y_1 + \beta_2 Y_2$, and Y_1 and Y_2 are mutually independent.

One has

$$\begin{aligned} f(\overline{y}) &= \int_{-\infty}^{+\infty} f(y) f(\overline{y} - y)\, dy \\ &= \int_0^{\overline{y}} \frac{e^{-y/\beta_1}}{\beta_1} \frac{e^{-(\overline{y}-y)/\beta_2}}{\beta_2} dy \\ &= \frac{1}{\beta_1 \beta_2} \int_0^{\overline{y}} e^{-y/\beta_1} e^{-(\overline{y}-y)/\beta_2} dy \\ &= \frac{1}{\beta_1 \beta_2} e^{-\overline{y}/\beta_2} \int_0^{\overline{y}} e^{-y/\beta_1} e^{y/\beta_2} dy. \end{aligned} \tag{A.5}$$

Define $y/\beta_1 - y/\beta_2 = z$, then $f(\overline{y})$ can be rewritten as

$$\begin{aligned} f(\overline{y}) &= -\frac{1}{\beta_1 - \beta_2} e^{-\overline{y}/\beta_2} \int_0^{((\beta_2-\beta_1)/\beta_1\beta_2)\overline{y}} e^{-z} dz \\ &= \frac{1}{\beta_1 - \beta_2} e^{-\overline{y}/\beta_2} e^{-z} \Bigg|_0^{\frac{\beta_2-\beta_1}{\beta_1\beta_2}\overline{y}} \\ &= \frac{1}{\beta_1 - \beta_2} \left(e^{-\overline{y}/\beta_1} - e^{-\overline{y}/\beta_2} \right). \end{aligned} \tag{A.6}$$

Define $Y = \overline{Y} + \beta_3 Y_3$, and $\overline{Y}$ and Y_3 are mutually independent.

One has

$$
\begin{aligned}
f(y) &= \int_{-\infty}^{+\infty} f(\overline{y})\, f(y-\overline{y})\, d\overline{y} \\
&= \int_0^x \frac{1}{\beta_1-\beta_2}\left(e^{-\overline{y}/\beta_1}-e^{-\overline{y}/\beta_2}\right)\frac{e^{-(x-\overline{y})/\beta_3}}{\beta_3}d\overline{y} \\
&= \frac{1}{(\beta_1-\beta_2)\beta_3}e^{-y/\beta_3} \\
&\quad\times\left[\int_0^y e^{-\overline{y}/\beta_1+\overline{y}/\beta_3}d\overline{y}-\int_0^y e^{-\overline{y}/\beta_2+\overline{y}/\beta_3}d\overline{y}\right] \\
&= \frac{1}{(\beta_1-\beta_2)\beta_3}e^{-y/\beta_3} \\
&\quad\times\left[\frac{\beta_1\beta_3}{\beta_3-\beta_1}\int_0^{((\beta_3-\beta_1)/\beta_1\beta_3)y}e^{-z}dz\right. \\
&\qquad\left.-\frac{\beta_2\beta_3}{\beta_3-\beta_2}\int_0^{((\beta_3-\beta_2)/\beta_2\beta_3)y}e^{-z}dz\right] \\
&= \frac{1}{(\beta_1-\beta_2)\beta_3}e^{-y/\beta_3} \\
&\quad\times\left[\frac{\beta_1\beta_3}{\beta_1-\beta_3}\left(e^{-((\beta_3-\beta_1)/\beta_1\beta_3)y}-1\right)\right. \\
&\qquad\left.-\frac{\beta_2\beta_3}{\beta_2-\beta_3}\left(e^{-((\beta_3-\beta_2)/\beta_2\beta_3)y}-1\right)\right] \\
&= \frac{\beta_1}{(\beta_1-\beta_2)(\beta_1-\beta_3)}\left(e^{-y/\beta_1}-e^{-y/\beta_3}\right) \\
&\quad-\frac{\beta_2}{(\beta_1-\beta_2)(\beta_2-\beta_3)}\left(e^{-y/\beta_2}-e^{-y/\beta_3}\right) \\
&= \frac{\beta_1}{(\beta_1-\beta_2)(\beta_1-\beta_3)}\left(e^{-y/\beta_1}-e^{-y/\beta_3}\right) \\
&\quad-\frac{\beta_2}{(\beta_1-\beta_2)(\beta_2-\beta_3)}\left(e^{-y/\beta_2}-e^{-y/\beta_3}\right) \\
&= \frac{\beta_1}{(\beta_1-\beta_2)(\beta_1-\beta_3)}e^{-y/\beta_1} \\
&\quad-\frac{\beta_2}{(\beta_1-\beta_2)(\beta_2-\beta_3)}e^{-y/\beta_2} \\
&\quad+\frac{\beta_3}{(\beta_1-\beta_3)(\beta_2-\beta_3)}e^{-y/\beta_3}.
\end{aligned}
\tag{A.7}
$$

Now, we have already obtained the probability density function of $\beta_{k,1}Y_{k,1}+\beta_{k,2}Y_{k,2}+\beta_{k,3}Y_{k,3}$, and then X can be expressed as

$$
X=\frac{\alpha Z}{1+Y}. \tag{A.8}
$$

From the form of the probability density function of $\beta_{k,1}Y_{k,1}+\beta_{k,2}Y_{k,2}+\beta_{k,3}Y_{k,3}$, we can see that its PDF is a linear combination of three PDFs which obey Chi-square distribution, and each part of that linear combination is a product of a Chi-square distribution and a constant; that is,

$$
\begin{aligned}
f(y) &= \frac{\beta_1^2}{(\beta_1-\beta_2)(\beta_1-\beta_3)}\frac{e^{-y/\beta_1}}{\beta_1} \\
&\quad-\frac{\beta_2^2}{(\beta_1-\beta_2)(\beta_2-\beta_3)}\frac{e^{-y/\beta_2}}{\beta_2} \\
&\quad+\frac{\beta_3^2}{(\beta_1-\beta_3)(\beta_2-\beta_3)}\frac{e^{-y/\beta_3}}{\beta_3}.
\end{aligned}
\tag{A.9}
$$

Assume that Z obeys Chi-square distribution with degree of freedom $2M$. When $J=1$, the distribution function of X is $\overline{F}_X(x)=1-\sum_{r=0}^{M-1}\sum_{l=0}^{r}(\alpha^{l+1-r}/\beta(r-l)!)(x^re^{-x/\alpha}/(x+\alpha/\beta)^{l+1})$. When $J=3$, the distribution function of X, $F_X(x)$, can be expressed as

$$
\begin{aligned}
F_X(x) &= \frac{\beta_1^2}{(\beta_1-\beta_2)(\beta_1-\beta_3)} \\
&\quad\times\left(1-\sum_{r=0}^{M-1}\sum_{l=0}^{r}\frac{\alpha^{l+1-r}}{\beta_1(r-l)!}\frac{x^re^{-x/\alpha}}{(x+\alpha/\beta_1)^{l+1}}\right) \\
&\quad-\frac{\beta_2^2}{(\beta_1-\beta_2)(\beta_2-\beta_3)} \\
&\quad\times\left(1-\sum_{r=0}^{M-1}\sum_{l=0}^{r}\frac{\alpha^{l+1-r}}{\beta_2(r-l)!}\frac{x^re^{-x/\alpha}}{(x+\alpha/\beta_2)^{l+1}}\right) \\
&\quad+\frac{\beta_3^2}{(\beta_1-\beta_3)(\beta_2-\beta_3)} \\
&\quad\times\left(1-\sum_{r=0}^{M-1}\sum_{l=0}^{r}\frac{\alpha^{l+1-r}}{\beta_3(r-l)!}\frac{x^re^{-x/\alpha}}{(x+\alpha/\beta_3)^{l+1}}\right) \\
&= 1-\frac{\beta_1}{(\beta_1-\beta_2)(\beta_1-\beta_3)} \\
&\quad\times\sum_{r=0}^{M-1}\sum_{l=0}^{r}\frac{\alpha^{l+1-r}}{(r-l)!}\frac{x^re^{-x/\alpha}}{(x+\alpha/\beta_1)^{l+1}} \\
&\quad-\frac{\beta_2}{(\beta_1-\beta_2)(\beta_2-\beta_3)} \\
&\quad\times\sum_{r=0}^{M-1}\sum_{l=0}^{r}\frac{\alpha^{l+1-r}}{(r-l)!}\frac{x^re^{-x/\alpha}}{(x+\alpha/\beta_2)^{l+1}} \\
&\quad+\frac{\beta_3}{(\beta_1-\beta_3)(\beta_2-\beta_3)} \\
&\quad\times\sum_{r=0}^{M-1}\sum_{l=0}^{r}\frac{\alpha^{l+1-r}}{(r-l)!}\frac{x^re^{-x/\alpha}}{(x+\alpha/\beta_3)^{l+1}}.
\end{aligned}
\tag{A.10}
$$

Thus, we can obtain $E[\ln(1+X)]$ for $J=3$ as follows:

$$E[\ln(1+X)] = \sum_{r=0}^{M-1}\sum_{l=0}^{r}\frac{(\alpha_{k,i})^{l+1-r}}{(r-l)!} \times \begin{bmatrix} \frac{\beta_1}{(\beta_1-\beta_2)(\beta_1-\beta_3)} I_1\left(\frac{1}{\alpha}, \frac{\alpha}{\beta_1}, r, l+1\right) \\ -\frac{\beta_2}{(\beta_1-\beta_2)(\beta_2-\beta_3)} I_1\left(\frac{1}{\alpha}, \frac{\alpha}{\beta_2}, r, l+1\right) \\ +\frac{\beta_3}{(\beta_1-\beta_3)(\beta_2-\beta_3)} I_1\left(\frac{1}{\alpha}, \frac{\alpha}{\beta_3}, r, l+1\right) \end{bmatrix}, \quad \text{(A.11)}$$

where $I_1(a,b,m,n) = \int_0^{\infty}(x^m e^{-ax}/(x+b)^n\ (x+1))dx$.

The close-form solution of this integral is in [31].

Acknowledgment

This work was supported by the National S&T Major Project (2012ZX03003-001).

References

[1] 3GPP TR 32.826, Telecommunication management; Study on Energy Savings Management (ESM), (Release 10), 2010, http://www.3gpp.org.

[2] Z. Hasan, H. Boostanimehr, and V. K. Bhargava, "Green cellular networks: a survey, some research issues and challenges," *IEEE Communications Surveys and Tutorials*, vol. 13, no. 4, pp. 524–540, 2011.

[3] G. Miao, N. Himayat, and G. Y. Li, "Energy-efficient link adaptation in frequency-selective channels," *IEEE Transactions on Communications*, vol. 58, no. 2, pp. 545–554, 2010.

[4] "Further Advancements for E-UTRA Physical Layer Aspects," Tech. Rep. TR 36.814 V9.0.0 (Release 9), 2010, http://www.3gpp.org.

[5] M. Peng and W. Wang, "Technologies and standards for TD-SCDMA evolutions to IMT-advanced," *IEEE Communications Magazine*, vol. 47, no. 12, pp. 50–58, 2009.

[6] M. Peng, W. Wang, and H. H. Chen, "TD-SCDMA evolution," *IEEE Vehicular Technology Magazine*, vol. 5, no. 2, pp. 28–41, 2010.

[7] C. Han and S. Armour, "Energy efficient radio resource management strategies for green radio," *IET Communication*, vol. 5, no. 18, pp. 2629–2639, 2011.

[8] M. Peng, X. Zhang, W. Wang, and H. Chen, "Performance of dual-polarized MIMO for TD-HSPA evolution systems," *IEEE Systems Journal*, vol. 5, no. 3, pp. 406–416, 2011.

[9] A. Molisch and M. Z. Win, "MIMO systems with antenna selection," *IEEE Microwave Magazine*, vol. 5, no. 1, pp. 46–56, 2004.

[10] A. Molisch, M. Z. Win, Y.-S. Choi, and J. H. Winters, "Capacity of MIMO systems with antenna selection," *IEEE Transactions on Wireless Communications*, vol. 4, no. 4, pp. 1759–1772, 2005.

[11] R. Chen, Z. Shen, J. G. Andrews, and R. W. Heath, "Multimode transmission for multiuser MIMO systems with block diagonalization," *IEEE Transactions on Signal Processing*, vol. 56, no. 7, pp. 3294–3302, 2008.

[12] M. Gharavi-Alkhansari and A. B. Gershman, "Fast antenna subset selection in MIMO systems," *IEEE Transactions on Signal Processing*, vol. 52, no. 2, pp. 339–347, 2004.

[13] Z. Shen, R. Chen, J. G. Andrews, R. W. Heath, and B. L. Evans, "Low complexity user selection algorithms for multiuser MIMO systems with block diagonalization," *IEEE Transactions on Signal Processing*, vol. 54, no. 9, pp. 3658–3663, 2006.

[14] Y. Liu, Y. Zhang, C. Ji, W. Q. Malik, and D. J. Edwards, "A low-complexity receive-antenna-selection algorithm for MIMO-OFDM wireless systems," *IEEE Transactions on Vehicular Technology*, vol. 58, no. 6, pp. 2793–2802, 2009.

[15] L. Sun and M. R. McKay, "Eigen-based transceivers for the MIMO broadcast channel with semi-orthogonal user selection," *IEEE Transactions on Signal Processing*, vol. 58, no. 10, pp. 5246–5261, 2010.

[16] J. K. Lain, "Joint transmit/receive antenna selection for MIMO systems: a real-valued genetic approach," *IEEE Communications Letters*, vol. 15, no. 1, pp. 58–60, 2011.

[17] T. Gucluoglu and T. M. Duman, "Performance analysis of transmit and receive antenna selection over flat fading channels," *IEEE Transactions on Wireless Communications*, vol. 7, no. 8, pp. 3056–3065, 2008.

[18] J. W. Kang, H. W. Je, C. S. Park, and K. B. Lee, "Transmit antenna subset selection for downlink MIMO systems in multicell environments," *IEEE Transactions on Wireless Communications*, vol. 9, no. 7, pp. 2113–2118, 2010.

[19] T. Zhou, M. Peng, W. Wang, and H. Chen, "Low-complexity coordinated beamforming for downlink multicell SDMA/OFDM system," *IEEE Transactions Vehicular Technology*, vol. 62, no. 1, pp. 247–255, 2013.

[20] S. Cui, A. J. Goldsmith, and A. Bahai, "Energy-efficiency of MIMO and cooperative MIMO techniques in sensor networks," *IEEE Journal on Selected Areas in Communications*, vol. 22, no. 6, pp. 1089–1098, 2004.

[21] M. T. Kakitani, G. Brante, R. D. Souza, and M. A. Imran, "Energy efficiency of transmit diversity systems under a realistic power consumption model," *IEEE Communications Letters*, vol. 17, no. 1, pp. 119–122, 2013.

[22] J. Joung, C. K. Ho, and S. Sun, "Power amplifier switching (PAS) for energy efficient systems," *IEEE Wireless Communications Letters*, vol. 2, no. 1, pp. 14–17, 2013.

[23] C. Jiang and L. J. Cimini, "Antenna selection for energy efficient MIMO transmission," *IEEE Wireless Communication Letters*, vol. 1, no. 6, pp. 577–580, 2012.

[24] J. Xu and L. Qiu, "Energy efficiency optimization for MIMO broadcast channels," *IEEE Transactions Wireless Communication*, vol. 12, no. 2, pp. 690–701, 2013.

[25] H. Li, G. P. Koudouridis, and J. Zhang, "Antenna selection schemes for energy efficiency in distributed antenna systems," in *Proceedings of the IEEE International Conference on Communications (ICC '12)*, pp. 5619–5623, 2012.

[26] D. W. K. Ng, E. S. Lo, and R. Schober, "Energy-efficient resource allocation in SDMA systems with large numbers of base station antennas," in *Proceedings of the IEEE International Conference on Communications (ICC '12)*, pp. 4027–4032, 2012.

[27] C. Jiang and L. J. Cimini, "Antenna selection for energy-efficient MIMO transmission," *IEEE Wireless Communications Letters*, vol. 1, no. 6, pp. 577–580, 2012.

[28] G. Lim and L. J. Cimini Jr., "Energy-efficient cooperative beamforming in clustered wireless networks," *IEEE Transactions on Wireless Communications*, vol. 12, no. 3, pp. 1376–1385, 2013.

[29] S. Li and L. Qiu, "Improving network energy efficiency through transmit antenna number and transmission mode selection in multicell systems," in *IEEE Vehicular Technology Conference (VTC '12)*, pp. 1–5, 2012.

[30] Q. H. Spencer, A. L. Swindlehurst, and M. Haardt, "Zero-forcing methods for downlink spatial multiplexing in multiuser MIMO channels," *IEEE Transactions on Signal Processing*, vol. 52, no. 2, pp. 461–471, 2004.

[31] J. Zhang and J. G. Andrews, "Adaptive spatial intercell interference cancellation in multicell wireless networks," *IEEE Journal on Selected Areas in Communications*, vol. 28, no. 9, pp. 1455–1468, 2010.

Hindawi Publishing Corporation
International Journal of Antennas and Propagation
Volume 2013, Article ID 167368, 7 pages
http://dx.doi.org/10.1155/2013/167368

Research Article

Interference Coordination in Multiple Antenna Based LTE-Advanced Heterogeneous Systems

Yuan Li, Li Zhang, Hua Chen, and Mugen Peng

Wireless Signal Processing and Network Lab, Key Laboratory of Universal Wireless Communications (Ministry of Education), Beijing University of Posts and Telecommunications, Beijing 100876, China

Correspondence should be addressed to Yuan Li; liyuanbupt@gmail.com

Received 9 January 2013; Accepted 19 March 2013

Academic Editor: Feifei Gao

With picocells deployed in the coverage of a macrocell in heterogeneous networks (HetNets), the macrocell evolved NodeB (MeNB) may receive interference signals from the picocell users, which results in more severe co-channel interference (CCI) problem in the uplink. In this paper, the spatial uplink interference coordination is investigated in multiple antenna systems, according to which the receiver coding matrix is generated by MeNB to mitigate the CCI from picocell users. Two interference coordination (IC) schemes are proposed based on whether the receiver coding matrix is full rank or not, named as full coding (IC-FC) and part coding (IC-PC), respectively. The application of the proposed schemes is discussed in single picocell and multiple picocell scenarios. The CCI can be totally canceled in single picocell scenario, and an algorithm is developed in multiple picocell networks to mitigate the most severely interfering picocell. Link level and system level simulations are applied, and it is shown that significant performance gain is achieved by our proposed schemes over traditional IC receivers.

1. Introduction

With more and more wireless subscribers nowadays, the data traffic demand in wireless networks is increasing exponentially, especially in hotspot areas. In order to meet this increasing demand for the unrelenting wireless data rate and enhance the hotspot and indoor coverage, third generation partnership project (3GPP) long term evolution (LTE) has been put into practice by operators [1, 2]. 3GPP has been working on LTE-Advanced (LTE-A) since Release 10 to further improve the network throughput by efficient techniques. Since the capacity of the point-to-point link has been approached to its theoretic limits, it is promising to deploy the low-cost transmission nodes, such as picos, relays, femtos, and remote radio units (RRUs) underlaying the existing conventional macrocell layout in a more compact manner, which is known as the heterogeneous network (HetNet).

The deployment of the low-cost nodes could make use of cell splitting gains and therefore improve the capacity and coverage of cellular networks. Full frequency reuse could be applied to further enhance the spectrum efficiency. Compared with homogeneous network, however, more severe cochannel interference (CCI) is caused in both downlink and uplink transmission due to the introduction of low-cost nodes [3], and it is significant to employ interference management techniques to mitigate CCI and improve the performance of HetNets.

As the interference problem in HetNet is challenging, much importance has been attached to the standardization for enhanced intercell interference coordination (eICIC) techniques in HetNets, which consists of enhanced fractional frequency reuse [4], application of almost blank subframes (ABSFs) [5], and enhanced reference signal design [6]. Conventional interference coordination techniques are generally performed in the time and frequency domain [7, 8]. Furthermore, based on the development of multiple input multiple output (MIMO) technologies in LTE-A systems [9], spatial domain interference coordination has been widely discussed [10], where the CCI could be mitigated by adjusting the transmit or receive beamforming with the exchange of channel state information (CSI) via backhaul [11]. An interference cancelation scheme was proposed in [12] based on coordinated transmit beamforming and user selection algorithm. The effect of the proposed scheme was evaluated,

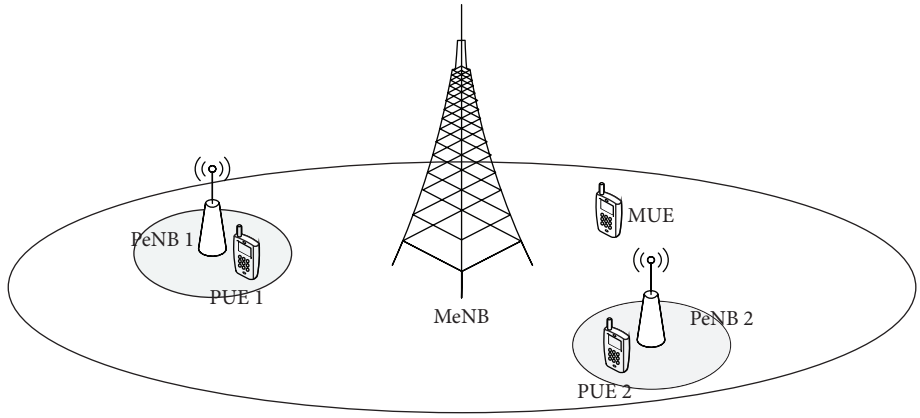

Figure 1: Uplink heterogeneous network composed of macrocell and picocells.

and the trade off between interference nulling and number of simultaneously scheduled users was revealed. Adaptive downlink spatial interference coordination was considered to mitigate CCI in cellular networks in [13], and the average throughput analysis was performed for perfect CSI and limited feedback scenarios, respectively.

However, most of the eICIC techniques mentioned above are studied for the downlink. In the uplink, the eICIC has been investigated based on the power control and range expansion (RE) [14]. The optimization of uplink power control for interference coordination was studied in [15] for relay based deployment, by which it is applicable to enhance the cell edge throughput as well as to adjust the receiver dynamic range. The authors in [16] evaluated the off-loading benefits of RE and investigated the impact of RE bias to the capacity as well as fairness in HetNets. In multiple antenna systems, it is beneficial to explore the advantage of coordinated receive beamforming in uplink transmission. In contrast with downlink coordinated beamforming, the CSI of interfering user equipments (UEs) can be directly obtained by the evolved NodeB (eNB) in uplink by the use of the training sequences instead of feedback or reciprocity [17], and is suitable in practical systems for low cost. To fully exploit the benefits of advanced multiple antenna technologies of LTE-A, the spatial interference coordination schemes should be investigated in uplink HetNets where multiple antennas are configured at both eNB and UE.

In this paper, we focus on the spatial domain interference coordination in uplink HetNets, where both eNBs and UEs are configured with multiple antennas. A receiver coding matrix is employed at the macrocell eNB (MeNB), which lies in the null space of the interference channels. Based on whether the coding matrix is full rank or not, two interference coordination schemes, named part coding (IC-PC) and full coding (IC-FC), are proposed to perform the receiver coding matrix for the MeNB. The application of the receiver coding matrix is investigated for both single picocell scenario and multiple picocells scenario, and an algorithm is developed to mitigate the most significant CCI from PUE in the multiple picocells scenario. It is shown by simulations that significant gains can be obtained by the proposed receiver coding matrix over conventional uplink receiver schemes, especially for single picocell scenario. The reason is that the CCI from picocells to the macrocell can be totally canceled in this scenario where the number of interference channels is less than that of receive antennas.

The rest of this paper is organized as follows. The system model for uplink CCI coordination in HetNets and two traditional receiver schemes are presented in Section 2. In Section 3, the single picocell scenario is analyzed, and the CCI coordination schemes are proposed. We further study the scenario of multiple picocells in Section 4, and an algorithm is presented to mitigate the most severe CCI from PUEs. In Section 5, the simulation results are given, and the conclusions are presented in Section 6.

Notations. Let bold-face letters represent matrices and vectors. Superscripts $(\cdot)^H$ and $(\cdot)^T$ denote the Hermitian transpose and transpose, respectively, and $\|\mathbf{X}\|^2$ denotes the norm of $\mathbf{X}$.

2. System Model

The uplink of a heterogeneous network is shown in Figure 1, where a high-power base station is overlaid with K low-power picocells. The MeNB is equipped with n_M receive antennas and picocell eNB (PeNB) has n_P receive antennas. Single user MIMO transmission is assumed, where one UE configured with n_{UE} transmit antennas transmits signals in a cell at each resource block. The macrocell and picocells share the same frequency resource, and K picocells are randomly located within macrocell coverage. The MUE and the kth PUE transmit with power P_M and $P_P^{(k)}$, respectively.

To be simple, we focus on the uplink CCI cancelation at MeNB side, but the results can be easily extended to the interference cancelation at the PeNB side. The received signal of MeNB can be expressed as

$$\mathbf{r}_M = \underbrace{\sqrt{P_M}\mathbf{H}_M\mathbf{W}_M\mathbf{x}_M}_{\text{Desired signal}} + \underbrace{\sum_{k=1}^{K}\sqrt{P_P^{(k)}}\mathbf{H}_P^{(k)}\mathbf{W}_P^{(k)}\mathbf{x}_P^{(k)}}_{\text{Cochannel interference}} + \underbrace{\mathbf{n}_M}_{\text{Noise}}, \quad (1)$$

where the matrix $\mathbf{H}_M \in \mathbb{C}^{n_M \times n_{\mathrm{UE}}} = \sqrt{L_M^M}\widetilde{\mathbf{H}}_M$ represents the uplink CSI from MUE to MeNB, where L_M^M denotes the pathloss from MUE to MeNB and each element of $\widetilde{\mathbf{H}}_M$ is modeled as complex Gaussian random variable $\mathcal{CN} \sim (0, 1)$. The matrix $\mathbf{H}_P^{(k)} \in \mathbb{C}^{n_M \times n_{\mathrm{UE}}} = \sqrt{L_M^k}\widetilde{\mathbf{H}}_P^{(k)}$ is the CSI from the kth PUE to MeNB. The item $\mathbf{W}_M \in \mathbb{C}^{n_{\mathrm{UE}} \times r}$ is the beamforming vector of MUE in which r is the rank of MUE, and $\mathbf{x}_M \in \mathbb{C}^{r \times 1}$ denotes the transmit data from MUE. The second part indicates the CCI from picocells. Each element of $\mathbf{n}_M$ indicates the terminal noise at MeNB side, which is modeled as additive white Gaussian noise (AWGN) vector with zero mean and variance σ^2.

Most of early works employ linear minimum mean squared error (MMSE) receiver and zero forcing (ZF) receiver to eliminate the interstream interference. The ZF receiver at MeNB can be denoted as

$$\mathbf{G}_{\mathrm{ZF}} = \left(\widehat{\mathbf{H}}_M^H \widehat{\mathbf{H}}_M\right)^{-1} \widehat{\mathbf{H}}_M^H, \tag{2}$$

where $\widehat{\mathbf{H}}_M = \mathbf{H}_M \mathbf{W}_M$ is the equivalent channel at the MeNB side. The CCI from PUEs could be suppressed by the interference rejection combining MMSE (IRC-MMSE) receiver if the interference channels could be detected by MeNB. Considering the CCI from PUEs as noise, the IRC-MMSE receiver can be expressed as

$$\mathbf{G}_{\mathrm{MMSE}} = \left(\widehat{\mathbf{H}}_M^H \widehat{\mathbf{H}}_M + \sum_{k=1}^{K} \frac{P_P^{(k)}}{P_M} \widehat{\mathbf{H}}_P^{(k)H0} \widehat{\mathbf{H}}_P^{(k)} + \frac{1}{\gamma'}\mathbf{I}\right)^{-1} \widehat{\mathbf{H}}_M^H, \tag{3}$$

where $\mathbf{I}$ is a unit matrix and γ' is the signal to noise ratio (SNR). After the receiver matrix, the signal to interference plus noise ratio (SINR) of the mth stream can be achieved as

$$\begin{aligned}\gamma_m = {} & P_M \left|\mathbf{g}_m \mathbf{H}_M \mathbf{w}_m\right|^2 \\ & \times \left(\left|\mathbf{g}_m \mathbf{n}_M\right|^2 + \sum_{\substack{n=1 \\ n \neq m}}^{r} P_M \left|\mathbf{g}_m \mathbf{H}_M \mathbf{w}_n\right|^2 \right. \\ & \left. + \sum_{k=1}^{k} \sum_{n=1}^{r} P_P^{(k)} \left|\mathbf{g}_m \mathbf{H}_P^{(k)} \mathbf{w}_n^{(k)}\right|^2 \right)^{-1},\end{aligned} \tag{4}$$

where $\mathbf{g}_m$ and $\mathbf{w}_m$ denote the corresponding vector of receiver coding matrix and transmit beamforming of the mth stream, respectively, and $\mathbf{w}_n^{(k)}$ is the nth transmit beamforming vector of the kth interfering PUE. Although the interstream interference could be well suppressed by ZF and MMSE receivers, the CCI from picocells are not taken into consideration, or simply treated as white noise, according to which the performance could not be further improved. Based on multiple antenna technologies, spatial interference coordination schemes are proposed in later sections to mitigate both interstream and intercell interference.

3. Cochannel Interference Cancelation for Single Picocell (K=1)

We first focus on CCI cancelation schemes when the number of picocells is $K = 1$ and assume that the receiver coding is performed at MeNB to eliminate CCI from transmitting PUEs. Define the coding matrix at receiver side as $\mathbf{G}$, then the signal $\mathbf{y}_M$ after detection can be written as

$$\begin{aligned}\mathbf{y}_M = \mathbf{G} \cdot \mathbf{r}_M = {} & \sqrt{P_M}\mathbf{G}\mathbf{H}_M \mathbf{W}_M \mathbf{x}_M \\ & + \sqrt{P_P^{(1)}}\mathbf{G}\mathbf{H}_P^{(1)} \mathbf{W}_P^{(1)} \mathbf{x}_P^{(1)} + \mathbf{G}\mathbf{n}_M.\end{aligned} \tag{5}$$

For the scenario where only one picocell is located in the coverage of one macrocell, the interference from picocell accounts for large amount of total interference and noise. The target of CCI cancelation is to construct a suitable receiver coding matrix $\mathbf{G}$, which should satisfy

$$\mathbf{G}\mathbf{H}_P^{(1)} \mathbf{W}_P^{(1)} = \mathbf{0}. \tag{6}$$

The CSI from interfering PUEs could be detected by the MeNB by the use of the training sequences, and the pattern of pilot as well as the scheduled PUE index have to be conveyed to the MeNB via backhaul, which could be viewed as the uplink interference coordination. Two schemes are proposed in this section based on the demand of (6).

3.1. Part Coding for Interference Cancelation. The singular value decomposition (SVD) is employed in this subsection to generate the coding matrix. Through SVD of the channel matrix $\mathbf{H}_P^{(1)} \mathbf{W}_P^{(1)}$ of PUE, the channel matrix is expressed as

$$\mathbf{H}_P^{(1)} \mathbf{W}_P^{(1)} = \mathbf{U}_P \begin{bmatrix} \Sigma_P \\ 0 \end{bmatrix} \mathbf{V}_P^H = \begin{bmatrix} \mathbf{U}_e, & \mathbf{U}_0 \end{bmatrix} \begin{bmatrix} \Sigma_P \\ 0 \end{bmatrix} \mathbf{V}_P^H, \tag{7}$$

where each diagonal element of the diagonal matrix $\Sigma_P = \mathrm{diag}\{\lambda_i\}$ is a nonnegative eigenvalue of the channel matrix $\mathbf{H}_P^{(1)} \mathbf{W}_P^{(1)}$ with a descending order. The matrix $\mathbf{U}_e$ is the left singular matrix of the channel matrix $\mathbf{H}_P^{(1)} \mathbf{W}_P^{(1)}$, and $\mathbf{U_P}$ is composed of n_M unit column vectors. $\mathbf{U}_e$ constructs the subspace of $\mathbf{H}_P^{(1)} \mathbf{W}_P^{(1)}$ and each column corresponds to an eigenvalue in Σ_P. As the dimension of $\mathbf{H}_P^{(1)} \mathbf{W}_P^{(1)}$ is $n_M \times r$, and $n_M \geq r$ for practical systems, the dimension of $\mathbf{U}_e$ is $n_M \times r$. The matrix $\mathbf{U}_0$ lies in the null space of $\mathbf{H}_P^{(1)} \mathbf{W}_P^{(1)}$ with dimension $(n_M - r) \times r$, that is, $\mathbf{U}_0 \mathbf{H}_P^{(1)} \mathbf{W}_P^{(1)} = \mathbf{0}$ so that the CCI could be mitigated. ZF operation could be applied to $\mathbf{U}_0 \mathbf{H}_M$ to further cancel the interstream interference. Therefore, the receiver coding matrix is evaluated as $\mathbf{G}_{\mathrm{PC}} = \left[(\mathbf{U}_0^H \mathbf{H}_M)^H \mathbf{U}_0^H \mathbf{H}_M\right]^{-1} (\mathbf{U}_0^H \mathbf{H}_M)^H \mathbf{U}_0^H$, and the signal after receiver coding $\mathbf{y}_M$ can be rewritten as

$$\mathbf{y}_M = \mathbf{G}_{\mathrm{PC}} \mathbf{H}_M \mathbf{W}_M \mathbf{x}_M + \mathbf{G}_{\mathrm{PC}} \mathbf{n}_M. \tag{8}$$

With the operation of coding matrix at receiver side in this way, the CCI can be totally eliminated, and the SINR of the mth stream can be represented as

$$\gamma_m = \frac{P_M \left|\mathbf{g}_{m,\mathrm{PC}} \mathbf{H}_M \mathbf{w}_m\right|^2}{\left|\mathbf{g}_{m,\mathrm{PC}} \mathbf{n}_M\right|^2}. \tag{9}$$

It should be noted that the number of MeNB receiving antennas n_M and the rank of transmitting data r should satisfy $n_M > r$, otherwise the left singular matrix $\mathbf{U}_P$ does not contain the null space of $\mathbf{H}_P^{(1)}\mathbf{W}_P^{(1)}$ and the coding matrix $\mathbf{G}$ cannot be obtained through SVD. Therefore, the coding matrix is not full rank, which reduces the multiplexing gain of the spatial channel.

3.2. Full Coding for Interference Cancelation. To take full use of the multiplexing gain by receiver coding, we propose the IC-FC scheme, which is formulated as

$$\text{maximize} \sum_{m=1}^{r} \log\left(1 + \frac{P_M\left|\mathbf{g}_{m,\mathrm{FC}}\mathbf{H}_M\mathbf{w}_m\right|^2}{\left|\mathbf{g}_{m,\mathrm{FC}}\mathbf{n}_M\right|^2}\right), \tag{10}$$

$$\text{subject to } \mathbf{G}_{\mathrm{FC}} = \begin{bmatrix}\mathbf{G}_{\mathrm{PC}}\\ \mathbf{G}_s\end{bmatrix} \in \mathbb{C}^{n_M\times n_M}, \tag{11}$$

$$\mathbf{G}_s\mathbf{H}_P^{(1)}\mathbf{W}_P^{(1)} = \mathbf{0}, \tag{12}$$

$$\left\|\mathbf{g}_m\right\|^2 = 1, \tag{13}$$

$$n_M > r, \tag{14}$$

where $\mathbf{g}_{m,\mathrm{FC}}$ is the mth row of $\mathbf{G}_{\mathrm{FC}}$, and $\mathbf{G}_s$ represents the supplement matrix composed of r rows $\mathbf{g}_i \in \mathbb{C}^{1\times n_M}$, to guarantee that $\mathbf{G}_{\mathrm{FC}}$ is full rank. The condition (12) guarantees the orthogonality between $\mathbf{G}_s$ and $\mathbf{H}_P^{(1)}\mathbf{W}_P^{(1)}$, so that the whole matrix $\mathbf{G}_{\mathrm{FC}}$ satisfy $\mathbf{G}_{\mathrm{FC}}\mathbf{H}_P^{(1)}\mathbf{W}_P^{(1)} = \mathbf{0}$ to totally eliminate the CCI from PUEs. As the rows of matrix $\mathbf{G}_{\mathrm{PC}}$ in IC-PC are unit vectors, each row vector $\mathbf{g}_m$ of $\mathbf{G}_s$ should being unit vector for keep conformity, as constrained with condition (13). It is clear that the proposed IC-FC method makes use of the supplement matrix and the matrix $\mathbf{G}_{\mathrm{PC}}$ of method IC-PC to construct a receiver coding unitary matrix with full rank, aiming at maximizing the SINR as well as eliminating CCI.

4. Cochannel Interference Coordination for Multiple Picocells ($K > 1$)

In this section, we study the CCI coordination scheme for multiple picocells scenario. Similar to the scheme for single picocell scenario, the receiver coding matrix $\mathbf{G}$ should satisfy

$$\begin{aligned}&\text{maximize} \sum_{m=1}^{r} \log\left(1 + \frac{P_M\left|\mathbf{g}_m\mathbf{H}_M\mathbf{w}_m\right|^2}{\left|\mathbf{g}_m\mathbf{n}_M\right|^2}\right),\\ &\text{subject to } \mathbf{G}\mathbf{H}_P^{(k)}\mathbf{W}_P^{(k)} = \mathbf{0} \quad (\forall k = 1, 2, \ldots, K),\\ &\left\|\mathbf{g}_k\right\|^2 = 1,\\ &\mathbf{G} \in \mathbb{C}^{n_M\times n_M},\\ &n_M > Kr.\end{aligned} \tag{15}$$

However, these four conditions usually cannot be satisfied at the same time in practical system due to the constraint of dimensions, especially for the scenario with very large K. So the CCI cannot be totally eliminated via receiver coding. We propose a suboptimal algorithm to reduce the interference through receiver coding for multiple picocells scenario.

In LTE system, power control is applied in the uplink to keep a balance between the demand to achieve the required quality-of-service (QoS), and the demand to minimize the interference to other cells as well as to save energy of mobile terminals. Various power control mechanisms have been proposed for interference coordination in heterogeneous networks. Generally, the transmitting power of each UE is configured according to the downlink pathloss and power control coefficient α, resulting in different transmitting power of each UE and also different interference power. It is obvious that the interference from the UE causing largest received power at eNB should be eliminated at the highest priority.

Our proposed interference coordination algorithm for multiple picocells scenario takes the received interference power into consideration. Detail steps are as follows.

(a) MeNB detects the interfering UEs in picocells and the received power $P_{\mathrm{inter}}^{(k)}$ of each interfering UE.

(b) Compare the received power of interfering UE, and find the UE corresponding to the maximum received power, which is denoted as

$$k^* = \arg\max_{k=1,2,\ldots,K} P_{\mathrm{inter}}^{(k)}. \tag{16}$$

(c) Calculate the receiver coding matrix by IC-FC or IC-PC with SVD proposed in Section 3, in which the corresponding channel matrix $\mathbf{H}_P^{(1)}\mathbf{W}_P^{(1)}$ of interference PUE is replaced with $\mathbf{H}_P^{(k^*)}\mathbf{W}_P^{(k^*)}$ of UE k^* in (6) and (12). Eliminate the interference from UE k^* and then the SINR after receiver coding can be expressed as

$$\gamma_m = \frac{P_M\left|\mathbf{g}_m\mathbf{H}_M\mathbf{w}_m\right|^2}{\left|\mathbf{g}_m\mathbf{n}_M\right|^2 + \sum_{\substack{j=1\\ j\neq k^*}}^{K}\sum_{n=1}^{r} P_P^{(j)}\left|\mathbf{g}_m\mathbf{H}_P^{(j)}\mathbf{w}_n^{(j)}\right|^2}. \tag{17}$$

It is obvious that the application of receiver coding matrix in single picocell scenario can be regarded as a special case of that in multiple picocells scenario, where the interfering UE with maximum received power is the only interfering UE and step of comparing the received power can be omitted.

5. Simulation Results

The link level and system level simulations are both employed to evaluate the performance of our proposed interference coordination schemes in this section. As the link level simulation does not take into consideration the effect of downlink pathloss, the performance of multiple picocells scenario is evaluated by system level simulation.

The heterogeneous deployment of LTE system is considered here for simulation, where K picocells are randomly placed over the coverage of a macrocell layout. The LTE single-carrier frequency division multiple access (SC-FDMA) uplink provides orthogonal transmission of different

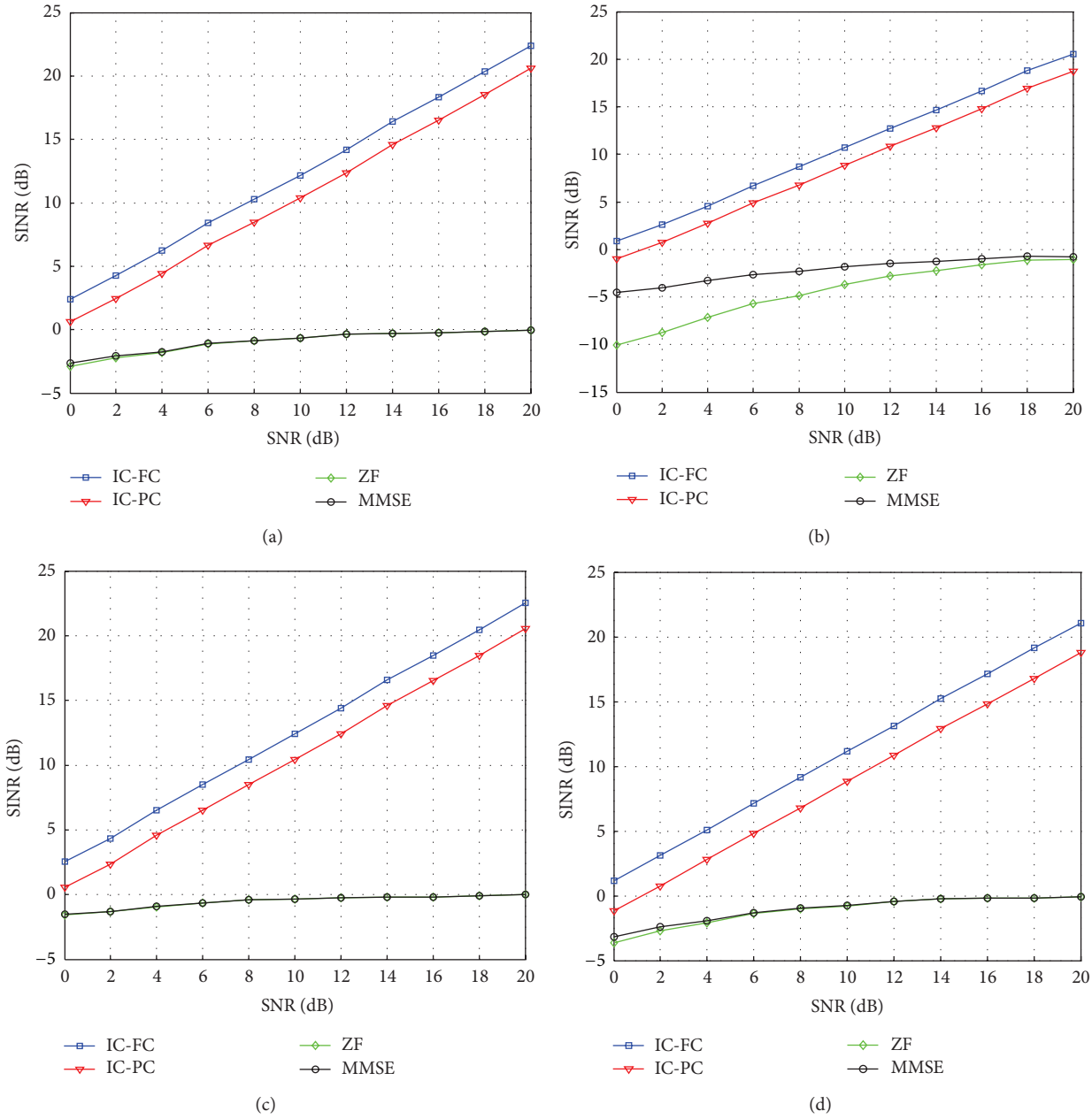

FIGURE 2: Link level results of receive SINR for single picocell scenario, for four cases: (a) $n_M = 4, r = 1$; (b) $n_M = 4, r = 2$; (c) $n_M = 8, r = 1$; (d) $n_M = 8, r = 2$.

UEs in the same cell, so intra-cell interference can be canceled. With uplink power control, the UE transmit power is given as

$$P = \min\{P_{\max}, P_0 + \alpha \cdot PL\}\,[\text{dBm}]\,, \tag{18}$$

where P_0 and α are power control parameters set on the basis of different cell types, and PL represents the downlink pathloss estimated through downlink reference signal in dB. The maximum transmit power of UE $P_{\max}$ indicates the transmit capacity of UE, which is fixed as in Table 1. The pathloss models are different for PUE and MUE, because of different transmit power of PeNB and MeNB and also different propagation environment. Detail simulation parameters are listed in Table 1.

In order to validate our proposed interference coordination schemes, IC-PC and IC-FC methods are simulated as well as traditional receiver schemes, ZF and MMSE.

Figure 2 shows the link level simulation results of the receive SINR curves for different receiver schemes as a function of the transmit SNR for single picocell scenario when $n_P = 4$, for four cases: (a) $n_M = 4, r = 1$; (b) $n_M = 4, r = 2$; (c) $n_M = 8, r = 1$; (d) $n_M = 8, r = 2$. We can see the receive SINR with IC-FC and IC-FC increases

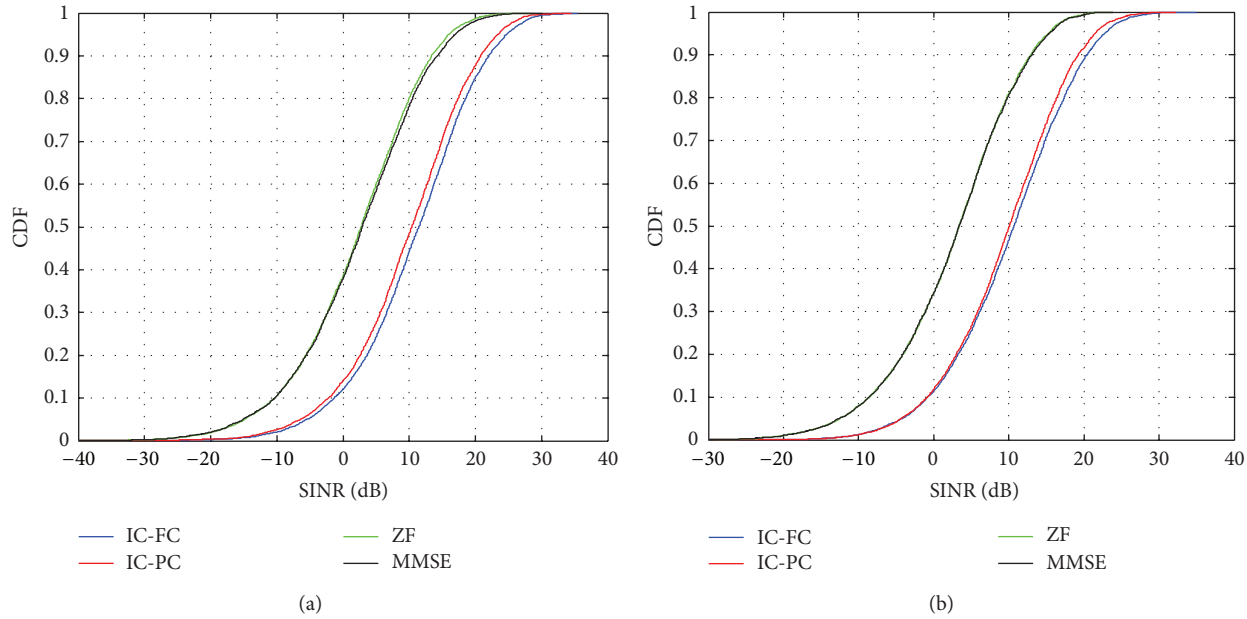

Figure 3: System level results of receive SINR CDF for multiple picocells scenario, for two cases: (a) $n_M = 4, K = 4, r = 1$; (b) $n_M = 4, K = 4, r = 2$.

Table 1: Simulation parameters.

Parameter	Assumption
Cellular layout	1 macrocell with K picocells
System bandwidth	10 MHz
Number of Picocells (K)	1, 2, 4, 8
Cell radius	
Macro	1 km
Pico	300 m
Antenna number (MeNB, PeNB, UE)	(4, 4, 2), (8, 4, 2)
UE noise figure	9 dB
Minimum distance	
Macro to Pico	>75 m
Macro to UE	>35 m
Pico to Pico	>40 m
Pico to UE	>10 m
Maximum UE Tx power ($P_{\max}$)	23 dBm
Pathloss Model (R in km)	
Macro to UE	$L = 128.1 + 37.6 \log_{10}(R)$
Pico to UE	$L = 140.7 + 36.7 \log_{10}(R)$
Power control	
Macro	$\alpha = 1.0, P_0 = -106$ dB m
Pico	$\alpha = 0.8, P_0 = -90$ dB m

almost linearly with the transmitter SNR as the CCI is totally canceled, while ZF and MMSE receiver hardly improve the MeNB performance due to the severe intercell interference. Compared with IC-PC, IC-FC scheme outperforms by about 1 dB at receive SINR for each case. It is also indicated that as the number of receiver antennas becomes larger, the receive SINR of IC-FC and IC-PC increases, which is due to the larger array gain. Another observation is that the SINR performance in cases $r = 2$ is a little beyond to the cases $r = 1$, because the transmit power of each stream decreases with respect to the limitation of total power.

The system level results of receive SINR CDF for multiple picocells scenario is shown in Figure 3 where $n_M = 4$, $K = 4$, $r = 1$ and 2. Similarly, it is demonstrated that IC-FC and IC-PC schemes outperform ZF and MMSE schemes obviously in receive SINR for the CCI from PUE can be canceled by IC-PC and IC-FC. The most severe interfering picocell can be mitigated by the interference coordination schemes of IC-FC and IC-PC, but interference from other picocells still leads to performance loss, resulting in little performance gap between IC-FC and IC-PC.

Figure 4 shows the receive SINR CDF curves of IC-PC and IC-FC when $n_M = 4$, $r = 2$, and different numbers of picocells are applied. It can be indicated that as the number of picocells increases, the receive SINR of each method decreases, because the interference from picocells increases which reduces the performance of the interference coordination schemes. It can also be observed that the performance gap between IC-FC and IC-PC turns smaller with more picocells deployed, because IC-FC and IC-PC schemes can only cancel the most severely interfering picocell, while the performance improvement may not be obvious with respect to the remaining CCI from other picocells.

6. Conclusion

The CCI coordination for uplink HetNets is took into consideration in this paper, where a receiver coding matrix is utilized to perform interference coordination at the receiver side. Two schemes, IC-PC and IC-FC, are proposed, by which

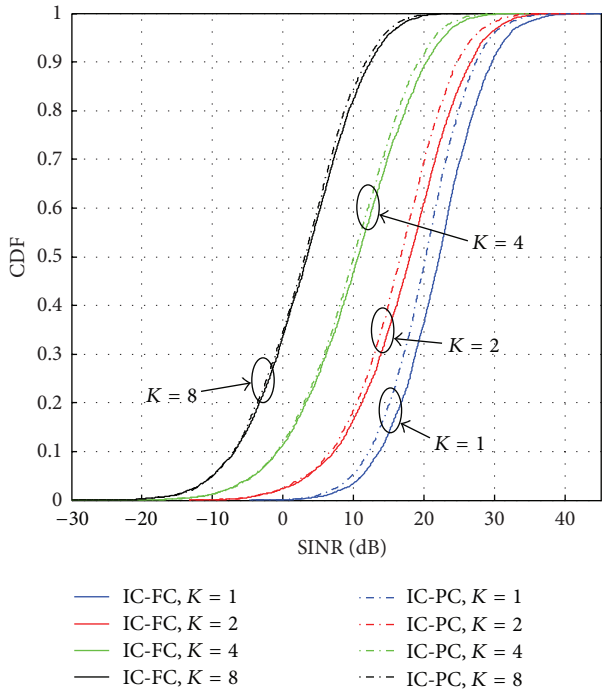

FIGURE 4: System level results of receive SINR CDF for multiple picocells scenario.

the CCI can be totally eliminated in single picocell scenario, and an algorithm is presented to mitigate the most severely interfering picocell for multiple picocells scenario. It is shown by simulations that significant improvement is achieved by our proposed schemes over the traditional ZF and MMSE schemes.

Acknowledgment

This work was supported in part by the State Major Science and Technology Special Projects (Grant no. 2011ZX03003-002-01), the National Natural Science Foundation of China (Grant no. 61222103), the National Basic Research Program of China (973 Program) (Grant no. 2013CB336600), the Beijing Natural Science Foundation (Grant no. 4131003), and the Interdiscipline cooperation projects of the New-Star of Science and Technology supported by Beijing Metropolis (Grant no. xxhz201201).

References

[1] M. Peng, W. Wang, and H. H. Chen, "TD-SCDMA evolution," *IEEE Vehicular Technology Magazine*, vol. 5, no. 2, pp. 28–41, 2010.

[2] M. Peng and W. Wang, "Technologies and standards for TD-SCDMA evolutions to IMT-advanced," *IEEE Communications Magazine*, vol. 47, no. 12, pp. 50–58, 2009.

[3] A. Damnjanovic, J. Montojo, Y. Wei et al., "A survey on 3GPP heterogeneous networks," *IEEE Wireless Communications*, vol. 18, no. 3, pp. 10–21, 2011.

[4] J. Y. Lee, S. J. Bae, Y. M. Kwon, and M. Y. Chung, "Interference analysis for femtocell deployment in OFDMA systems based on fractional frequency reuse," *IEEE Communications Letters*, vol. 15, no. 4, pp. 425–427, 2011.

[5] D. López-Pérez, I. Güvenç, G. de la Roche, M. Kountouris, T. Q. S. Quek, and J. Zhang, "Enhanced intercell interference coordination challenges in heterogeneous networks," *IEEE Wireless Communications*, vol. 18, no. 3, Article ID 5876497, pp. 22–30, 2011.

[6] D. Bai, J. Lee, H. Nguyen et al., "LTE-advanced modem design: challenges and perspectives," *IEEE Communications Magazine*, vol. 50, no. 2, Article ID 6146497, pp. 178–186, 2012.

[7] C. W. Xing, Z. S. Fei, N. Li, Y. T. Han, D. Danev, and J. M. Kuang, "Statistically robust resource allocation for distributed multi-carrier cooperative networks," *Science China Information Sciences*, vol. 56, no. 2, pp. 109–121, 2013.

[8] M. Peng, X. Zhang, and W. Wang, "Performance of orthogonal and co-channel resource assignments for femto-cells in LTE systems," *IET Communication*, vol. 7, no. 5, 2011.

[9] M. Peng, X. Zhang, W. Wang, and H. Chen, "Performance of dual-polarized MIMO for TD-HSPA evolution systems," *IEEE Systems Journal*, vol. 5, no. 3, 2011.

[10] D. Lee, H. Seo, B. Clerckx et al., "Coordinated multipoint transmission and reception in LTE-advanced: deployment scenarios and operational challenges," *IEEE Communications Magazine*, vol. 50, no. 2, Article ID 6146494, pp. 148–155, 2012.

[11] H. Droste, P. Marsch, M. Grieger et al., "Coordinated multipoint: concepts, performance, and field trial results," *IEEE Communications Magazine*, vol. 49, no. 2, pp. 102–111, 2011.

[12] U. Jang, H. Son, J. Park, and S. Lee, "CoMP-CSB for ICI nulling with user selection," *IEEE Transactions on Wireless Communications*, vol. 10, no. 9, Article ID 5967989, pp. 2982–2993, 2011.

[13] J. Zhang and J. G. Andrews, "Adaptive spatial intercell interference cancellation in multicell wireless networks," *IEEE Journal on Selected Areas in Communications*, vol. 28, no. 9, pp. 1455–1468, 2010.

[14] R. Madan, J. Borran, A. Sampath, N. Bhushan, A. Khandekar, and T. Ji, "Cell association and interference coordination in heterogeneous LTE-A cellular networks," *IEEE Journal on Selected Areas in Communications*, vol. 28, no. 9, pp. 1479–1489, 2010.

[15] Ö. Bulakci, S. Redana, B. Raaf, and J. Hämäläinen, "Impact of power control optimization on the system performance of relay based LTE-Advanced heterogeneous networks," *Journal of Communications and Networks*, vol. 13, no. 4, pp. 345–360, 2011.

[16] I. Guvenc, "Capacity and fairness analysis of heterogeneous networks with range expansion and interference coordination," *IEEE Communications Letters*, vol. 15, no. 10, Article ID 6008531, pp. 1084–1087, 2011.

[17] W. Lee, I. Lee, J. S. Kwak, B.-C. Ihm, and S. Han, "Multi-BS MIMO cooperation: challenges and practical solutions in 4G systems," *IEEE Wireless Communications*, vol. 19, no. 1, Article ID 6155881, pp. 89–96, 2012.

Hindawi Publishing Corporation
International Journal of Antennas and Propagation
Volume 2013, Article ID 181579, 9 pages
http://dx.doi.org/10.1155/2013/181579

Research Article

The Study of Indoor and Field Trials on 2×8 MIMO Architecture in TD-LTE Network

Xiang Zhang,[1] Xinyu Gu,[2] Wenyu Li,[1] Lin Zhang,[2] Jia Shen,[1] and Yi Wan[1]

[1] *Beijing Key Laboratory of New Generation Broadband Wireless Mobile Communication Technology, Standard and Verification, China Academy of Telecommunication Research, Beijing 100191, China*
[2] *Beijing University of Posts and Telecommunications (BUPT), Beijing 100876, China*

Correspondence should be addressed to Xiang Zhang; zhangxiang2468@gmail.com

Received 31 December 2012; Accepted 13 March 2013

Academic Editor: Mugen Peng

With the development of mobile internet service, long-term evolution (LTE) system was proposed in the third generation partnership project (3GPP) to provide higher data rates and frequency efficiency. Since the year of 2010, 113 LTE networks have been commercially deployed worldwide, and most of the networks are based on frequency division duplexing (FDD). In this paper, measurement methods of four MIMO transmission modes (TMs) in time division-LTE (TD-LTE) are studied and analyzed. Link level simulation is carried out to evaluate the downlink throughput for different signal-to-noise ratios and parameter settings. Furthermore, indoor and field tests are also presented in the paper to investigate how real-world propagation affects the capacity and the error performance of MIMO transmission scheme. For the indoor test, radio channel emulators are applied to generate realistic wireless fading channel, while in the field trials, a live TD-LTE experiment cellular network is built, which contains several evolved nodeBs (eNBs) and a precommercial user equipment (UE). It is shown from both simulation and tests results that MIMO deployment gives a substantial performance improvement compared with the third generation wireless networks.

1. Introduction

The deployment of long-term evolution (LTE) radio access technology, defined by the third generation partnership project (3GPP) specification [1–3], is currently ongoing on a broad scale. Based on the global mobile suppliers association's report [4], since the first LTE network was built in the year of 2009, 113 commercial networks have been deployed in 51 countries. Most of current LTE networks use paired spectrum frequency, which means that uplink and downlink transmissions are allocated in two different frequency bands. However, due to the lack of frequency resource and the characteristic of asymmetric data services, time division-LTE (TD-LTE) draws lots of attentions worldwide, especially in China. TD-LTE is an integral part in the 3GPP standards and can provide an evolutionary roadmap for TD-synchronous code division multiple access (TD-SCDMA) systems [5–7]. China Mobile, which is the biggest network operator in China, announced that the TD-SCDMA sites and other elements, for example, antenna, radio frequency, and so forth, can be reused in the TD-LTE, so the cost of building a new TD-LTE network will be reduced. In order to verify the performance of TD-LTE network, three steps were scheduled before commercial deployment. Firstly, basic architecture and transmission function were analyzed and evaluated by the simulation. Meanwhile, several indoor experiments were accomplished. Secondly, in the large scale trials (Phase I) during 2011, China Mobile built 850 base stations in 6 cities to verify the performance of key techniques in TD-LTE system, involving network equipments, mobile devices, and chipsets. In addition, the following Phase II trials extend the number of experiment cities to 13 and 7 system manufactures participate in the project. The indoor and field test environments discussed in this paper belong to these trials.

Indoor and outdoor trials are a promising way to evaluate the performance of a new system. Extensive literatures have been published to discuss LTE experimental methods and

results [8–11]. In [8], dual-antenna design was investigated in lower carrier frequencies, for example, band 13 (746 MHz–756 MHz). Field trials in that paper are based on the 2 × 2 multiple-input multiple-output (MIMO) precommercial LTE network, that is, two receive branches at the user equipment (UE) and two transmit branches at the base station. In addition, the authors in [9] extended the number of transmission antennae to four and the carrier frequency was set in band 38 (2570 MHz–2620 MHz). The trial results show that the close-spaced copolarized configuration provides the best performance for the users with poor channel condition, while dual-polarized and large-spaced antenna configuration is suitable for the users at the cell center. Recently, with the development of wireless techniques, LTE-advanced (LTE-A) has been widely discussed [10, 11]. The closed-loop single user-MIMO (SU-MIMO) transmission was evaluated under adaptive modulation coding (AMC) combined with carrier aggregation in the LTE-A uplink [10]. Cross-polarized antenna configuration and the influence of slanted angles for the UE were considered. By employing uplink 2 × 2 SU-MIMO, the average throughput is increased by 60% compared to the 2 × 1 antenna architecture. Downlink performance of LTE-A was discussed in [11], which clarified the relationship between modulation schemes and antenna polarization. According to the trial results, copolarized antenna is suitable for 16QAM while 64QAM can achieve better throughput with dual-polarized antennas. However, all the field trials mentioned perviously are based on the frequency division duplexing (FDD) LTE network. To the best our knowledge, there is no previous work referring to the TD-LTE test methods and results in both indoor and outdoor scenarios.

In this paper, we focus on the performance comparison of different transmission modes (TMs) in TD-LTE downlink, where 2 × 8 antenna configuration is verified by link level simulation, indoor emulation, and field tests. Firstly, average throughput versus different signal-to-noise ratio (SNR) is given in two typical channel models, that is, spatial channel model extended (SCME) [12–14] and international mobile telecommunication-advanced (IMT-A) models [15, 16]. Then, in our indoor lab, base station and UE are connected via the radio channel emulation equipment to analyze TD-LTE MIMO performance in the fading environment. By utilizing channel emulators, instant fast fading channel impulse responses are built for both uplink and downlink, and noise is added according to the input setting parameters. After the stages of simulation and indoor experiments, field trials are performed in a TD-LTE precommercial network. The test results show that the spectrum efficiency and the cell coverage of TD-LTE system are similar to that of FDD-LTE system.

The paper is organized as follows. In Section 2, the MIMO transmission modes utilized in TD-LTE are described, and the link level simulation assumptions and results are given. Then, indoor experiment is presented, and two channel models, that is, SCME and IMT-A, are discussed in Section 3. In Section 4, field trial methods and results are provided. Finally, we conclude the paper in the Section 5.

2. Analysis and Simulation for MIMO Transmission Modes

In LTE system, independent data steams (codewords) are mapped onto one or two layers, and then the layer mapping is performed based on the precoding scheme [2, 3]. There are 8 transmission modes defined in 3GPP release 9 for LTE downlink [1], (1) single transmit antenna, (2) transmission diversity, (3) open loop spatial multiplexing with cyclic delay diversity (CDD), (4) closed loop spatial multiplexing, (5) multiuser MIMO, (6) closed loop spatial multiplexing using a single transmission layer, (7) beamforming, and (8) dual layer beamforming.

Transmission modes 1 and 7 are identical from the UE perspective, where single layer transmission is adopted. TM1 only uses one antenna for downlink transmission, while beamforming technique is adopted in TM7 to make full use of multiple antennas at the base station. Therefore, diversity gain and array gain can be achieved. Meanwhile the computational complexity at UE does not increase, because the mobile device appears to receive only one transmit antenna and the actual number of antennas cannot be seen at the UE side. Transmit diversity is observed as a fallback option for some transmission modes due to its robustness. TM2 is suitable to be deployed at the access procedure and data transmission when channel condition is not satisfied. If the base station has two antennas, space frequency block code (SFBC) is adopted, while for four antennas scenario, a combination of SFBC and frequency switched transmit diversity (FSTD) is applied. In the TM6, downlink channel quality is fed back to the base station and the transmission layer is still restricted to one. In order to increase the capacity, two codewords can be supported for transmission modes 3, 4, 5, and 8. In the TM3, if the rank is greater than one, the signal is supplied to each antenna with a specific delay. No feedback is required before precoding, except for the rank indicator (RI). Transmission modse 4 and 8 can be observed as the enhancement of transmission modes 6 and 7, respectively. Based on the UE feedback precoding matrix indicator and RI, two data stream transmission is achieved in the closed loop multiplexing. Two layers are configured at the base station in the TM8 so that the beamforming and multiplexing can be combined for one or two UEs. MU-MIMO implement is defined in mode 5 where two users can be scheduled in the same resource block. In TD-LTE network, we mainly focus on the transmission modes 2, 3, 7, and 8. Moreover, mode adaptation is considered in the practical deployment. When the channel condition is good enough, two data streams, that is, transmission mode 3 or 8, are adopted to improve system throughput, while for the users at the cell edge or experiencing long-term deep fading, transmit diversity and beamforming are selected to provide diversity gain.

In order to evaluate the performance of the previous MIMO transmission modes, reliable measurement-based channel models are needed, which have to be accurate because the wireless propagation environment has a significant impact on the network throughput. In this paper, SCME none LOS (NLOS) [12–14] and IMT-A urban macro (UMa) line-of-sight (LOS) [15, 16] channel models are exploited

for MIMO performance evaluation and comparison. There are twelve clusters in the IMT-A UMa LOS channel model, and each cluster contains twenty rays. For the two strongest clusters, rays are divided into three subclusters with fix delay offsets. For SCME channel model, there is no LOS cluster, because the blocking impact caused by the buildings is assumed in between the base station and UE. There are six clusters in the channel model. Each cluster can be divided into three subgroups. Twenty rays are allocated in these subgroups based on the specific order, which is clarified by [15]. It is noted that doppler frequency shift, multipath, and the correlation between multiple antennas are all considered in these small-scale fading models.

In this session, the downlink performance of TD-LTE network is evaluated by the link level simulation. The base stations are equipped with eight antennas, and UE has two antennas for downlink receiving because of the size limitation and the cost. However, only one primary antenna at the UE is allowed for uplink transmission. The same antenna architecture is assumed in [17]. Average throughput of transmission modes 2, 3, 7, and 8 is presented and compared versus different SNR region. Three bands have already been allocated to China mobile for TD-LTE application, which can be classified by band 38, band 39, and Band 40. band 38 and band 39 will be utilized for outdoor deployment, while band 40 is suitable for the indoor hotspot coverage. During the simulation, band 38, where the center frequency is 2.6 GHz, is adopted with 20 MHz bandwidth. The special subframe configuration 7 is applied, while uplink-downlink configuration type 1 is supported. For simplicity, normal cyclic prefix is assumed. In order to meet the requirement of fast fading channel, adaptive modulation and coding (AMC) and hybrid automatic repeat request (HARQ) are introduced in the simulation platform. Turbo coding is utilized to combat the long-term deep fading, and the max-log-map decoding algorithm is accomplished. Interstream interference and noise are eliminated by minimum mean square error (MMSE) detection at the receiver [16]. Due to the fact that the channel reciprocity is obtained in the TD-LTE, the downlink beamforming is based on the uplink channel estimation. We assumed that the ideal reciprocity is applied in the simulation, where the beamforming matrix is perfectly matched to the downlink channel propagation characteristic. Detailed assumptions and parameters are listed in Table 1.

The average downlink throughput for IMT-A and SCME channel models is given by Figures 1 and 2, respectively. As can be seen from the link level simulation results, at the low SNR region, the average throughput is nearly the same for all transmission modes. Since the transmission modes 3, 7, and 8 can fall back to SFBC if the channel condition is unsatisfied, diversity gain is provided to eliminate the impact of the noise. As the SNR increases, the performance gap for different velocity is enlarged due to the doppler frequency shift. When SNR is equal to 28 dB, the average downlink throughput is approximate to the peak rate for transmission mode 2 and 7. Due to the interference between two data streams, downlink throughput of transmission modes 3 and 8 is significantly decreased with high speed. Particularly for the TM7 and TM8, the downlink precoding is based on the uplink channel estimation in the previous frame. Therefore, if the channel impulse response rapidly changes in the time domain, the advantages of beamforming technique will be vanished. The throughput with low speed for TM8 outperforms TM3 in most SNR regions, but the peak rate is slightly lower because of the signaling cost. Since the multiplexing gain is obtained, the throughput of transmission modes 3 and 8 is increased by 60% compared with that of transmission modes 2 and 7 at the high SNR region.

Table 1: Simulation parameters.

Parameters	Assumptions
No. of eNB antennas	8
No. of UE antennas	2
Transmission mode	2, 3, 7, and 8
Bandwidth	20 MHz
Channel reciprocity	Ideal
Uplink and downlink configuration	1
Special subframe configuration	7
MCS selection scheme	10% initial BLER
Fast HARQ scheme	Chase combining
Traffic model	Full buffer
Channel estimation	Ideal
Detection algorithm	MMSE
Scenario	Urban macro
Channel model	SCME and IMT-A
UE speed	3 km/h, 30 km/h and 120 km/h

3. Indoor Experiment of Downlink Performance

After the stage of simulation, where key techniques of MIMO architecture have been verified, indoor experiment needs to be addressed to examine the TD-LTE function and performance before the field trials. Some interoperability test (IOT) items are also included in this stage. However, we mainly focus on the downlink average throughput of transmission modes 2, 3, 7, and 8 in this section. In our indoor laboratory, a single precommercial network system is employed, which contains core network, a building base band unit (BBU), and a radio remote unit (RRU). The maximum of transmission power in each antenna port is 0 dBm, and other detailed parameter settings are listed in Table 1. A TD-LTE release 9 based universal serial bus (USB) dongle performs as the receiver. The RRU and USB dongles are connected via radio channel emulators, which are applied to generate accurate and realistic channel fading. In order to compare the results between the simulation and indoor test, SCME and IMT-A channel models are adopted by the channel emulator.

As depicted in Figure 3, eight cross-polarized antenna ports at the RRU are connected to the downlink channel emulator by the cable lines, and 2×8 MIMO channel fading is added, where multipath fast fading, doppler frequency

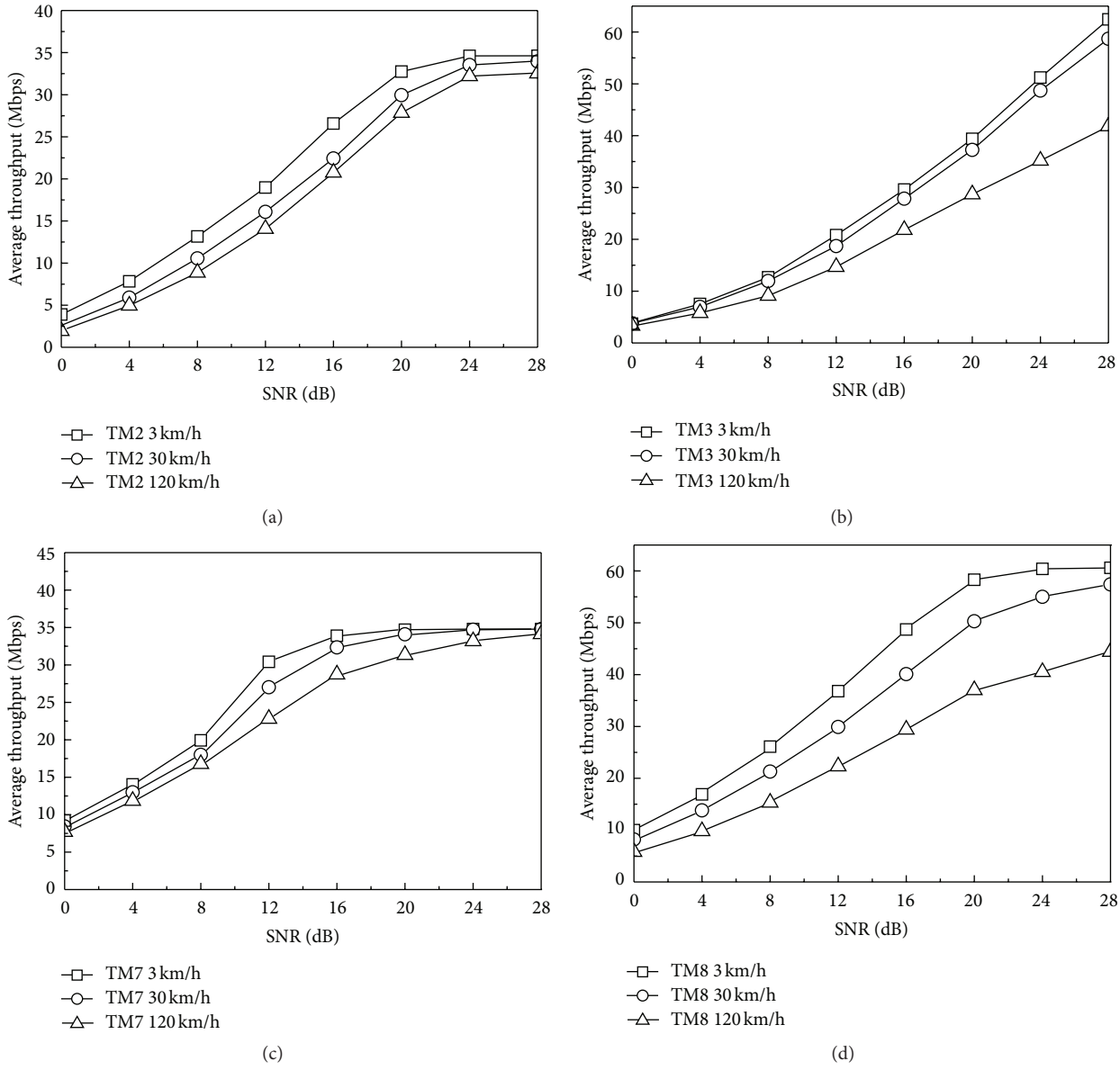

Figure 1: The downlink average throughput for IMT-A NLOS.

shift, and the spatial correlation between multiple antennas are considered. Additive white Gaussian noise (AWGN) is combined in the output signals at the emulator, and the noise power is based on the SNR settings. The USB dongle detects the desired downlink information and feeds back the acknowledgements (ACKs) or negative acknowledgements (NACKs). It is noted that although two antennas are deployed at the UE, only one main antenna is allowed for uplink transmission. Due to the fact that TDD mode is applied, the signals for both uplink and downlink should experience the same channel fading. A single channel emulator can be utilized to evaluate the performance of open-loop MIMO scheme, for example, SFBC and CDD, but for the TM7 and TM8, where downlink beamforming vector is based on the uplink channel estimation, two channel emulators are needed to separately emulate the uplink and downlink channel fading. Moreover, in order to obtain the channel reciprocity of TDD mode, the uplink and downlink channel emulators should be synchronized and can simultaneously play the same channel models. After the random access procedure, a file transfer protocol (FTP) client is used to download several large files. The average throughput for each selected SNR value is calculated during 5 min. The downlink average throughput of transmission modes 2, 3, 7, and 8 for SCME and IMT-A channel model is given in Figures 4 and 5, respectively.

As depicted in Figures 4 and 5, the throughput for TM2 is almost the same for the three types of velocity, since the diversity gain is obtained to decrease the impact of doppler frequency shift. At the high SNR region, the three curves

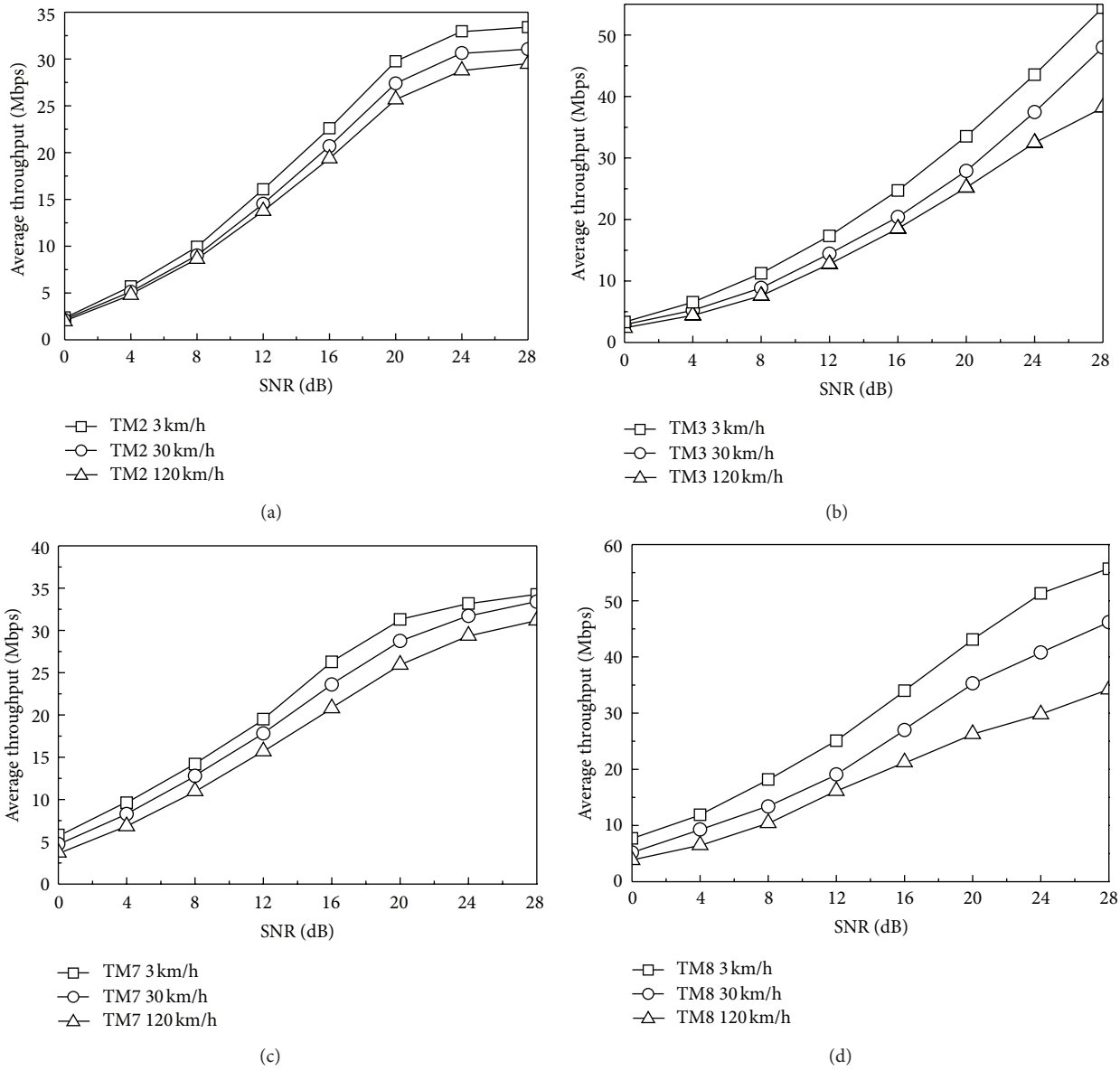

Figure 2: The downlink average throughput for SCME LOS.

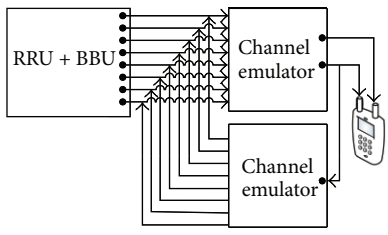

Figure 3: The indoor test scenario.

of TM2 overlap, because the peak rate can be achieved. The throughput of TM3 outperforms TM2 significantly, if the channel condition is qualified to support two data streams. However, the performance enhancement of TM3 in the indoor test is lower than that in the simulation, because the channel emulator is employed to formulate the complex wireless channel propagation. Both the interference between the multiple antennas and the noise are introduced by the channel emulator. TM7 and TM8, where the beamforming scheme is applied, are more sensitive to the velocity. The reason for this is that the downlink beamforming precoding matrix is based on the uplink channel estimation. If the channel experiences rapidly time varying, the beamforming gain will vanish. As the velocity increases, the throughput of TM8 is lower than that of TM3. Moreover, the performance improvement of TM8 is vanished when the velocity is equal to

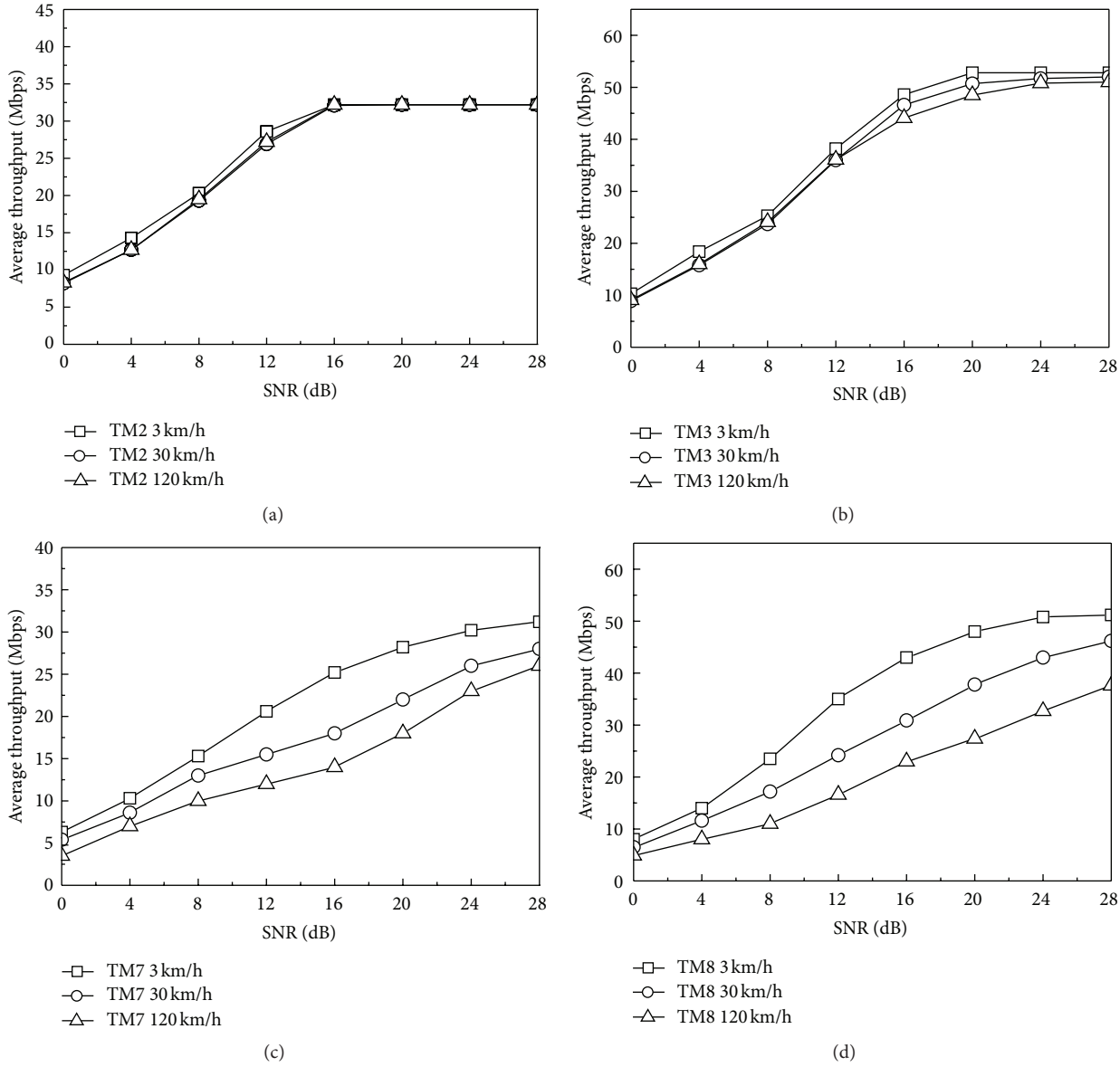

Figure 4: The average throughput for IMT-A based on the indoor experiment.

120 km/h. Because of the diversity gain provided by the SFBC and the well optimization at the UE, the throughput of TM2 and TM3 for different speed is almost the same.

4. Field Trial Setup and Measurement Results

In this section, field trials are performed to further investigate the performance of different MIMO transmission modes in TD-LTE system. In the experiment network, band 38 is implemented with 20 MHz bandwidth to evaluate the downlink average throughput for the transmission modes 2, 3, 7, and 8. The radio environment is selected as similar as possible to what UEs will experience in a commercial network. For this purpose, the field trial was conducted in Huai Rou district, a typical urban macroscenario near Beijing, China. This area contains several blocks, where almost all of the buildings have five or six floors. There are five base stations deployed in this area, and about ten sectors are located in the trial route. The base station antenna radomes are installed on the roofs near the trial streets. Each antenna radome has four linearly ordered columns with a horizontal spacing of 0.7 λ (λ represents the wavelength). In each column, a colocated antenna pair is adopted, which is cross-polarized by $\pm 45^{\circ}$ from the vertical. USB dongle employs two antennas for downlink reception and only uses a single main antenna to transmit uplink messages. The maximum of downlink common reference signal (CRS) power and total uplink transmission power is set to 15 dBm and 23 dBm, respectively. Moreover, closed-loop power control algorithm

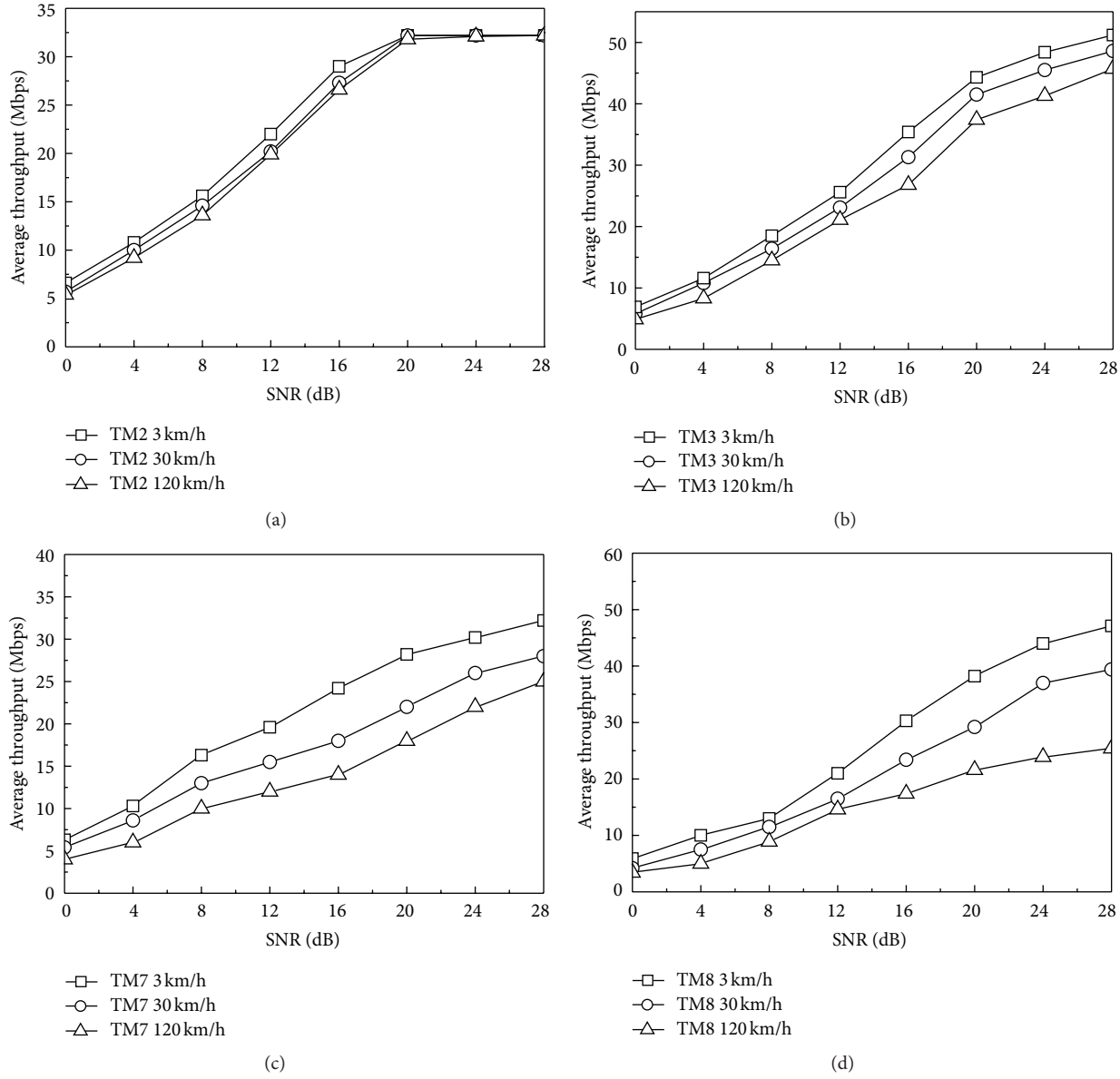

Figure 5: The average throughput for SCME based on the indoor experiment.

is introduced in the uplink to overcome the impact of pathloss and shadow fading. AMC and HARQ are also applied in the network to improve downlink throughput. The UE capability is restricted to the category 3.

Field trials presented in the paper include two items, that is, stationary testing and mobility testing. In the stationary test case, the post-SNR (SINR) is reported by the UE after joint detection. Nigh fixed locations, where the SINR is approximate to the SNR settings in the simulation and indoor experiments, are selected in a single sector. Because the target SINR points are ranging from 0 to 25 dB, the distance between the serving base station and USB dongle is approximately from 50 m to 400 m. In the high SINR region, a direct LOS radio propagation is selected, while in order to measure the UE capacity in low SINR region, NLOS channel condition is adopted, which is generated by the surrounding office buildings which are five or six floors high between the transmitter and receiver. In each selected SINR location, USB dongle is attached in the network and downloads FTP files during five minutes. Average throughput is calculated and compared for different transmission modes (Table 2).

As depicted in Figure 6, the downlink throughput for different transmission modes is evaluated under nigh fixed locations. In the low SINR region, that is, 0 dB, the four transmission modes have similar performance. As the SINR increases, the TM3 and TM8 outperform TM2 and TM7 due to the multiplexing gain. The beamforming technique, which is adopted by the TM7 and TM8, can improve the throughput significantly if the SINR is lower than 12 dB. However, the peak rate of TM3 is slightly higher than that

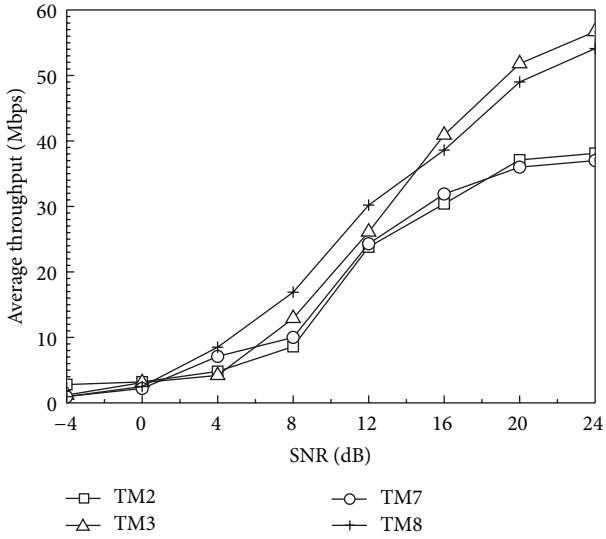

Figure 6: The downlink average throughput in the field trail.

of TM8 owing to the less signalling cost. Although complex radio propagation is provided by the field trail, the data rate of TM3 is approximate to 60 Mbps when SINR is equal to 24 dB. If the SINR is higher than 20 dB, the peak rate of TM2 and TM7 is achieved. It is noted that in each selected location, the test vehicle will not move while the test UE downloads the files. Hence, the doppler frequency shift is small and the beamforming performance enhancement is more remarkable.

For the mobility testing, a drive route is carefully designed to go cross all the ten sectors, and the maximum distance between the base station and UE is approximately 500 m. The terrain is generally flat and dominated by the five or six floored buildings. In the experiment route, both high and low SINR regions are included, and the reference signal receiving power (RSRP) levels are ranging from −65 dBm to −110 dBm. Due to the varying radio environments, a wide range of channel characteristics appear, which contain both LOS and NLOS channel models. The USB dongle was placed in the vehicle and the drive speed was mostly under 30 km/h. If the UE is moved to the edge of serving cell, handover or cell reestablishment is executed depending on the network coverage. The measurement route takes 20 minutes for one lap. It is noted that the style of the testing vehicle and the traffic in the street are probably important aspects for the performance evaluation. Hence for each experiment item, we take 2 hours to obtain average downlink throughput meanwhile at least 5 laps driving along the route are needed. Two MIMO architectures are included in the mobility test, that is, (1) transmission modes 2, 3, and 7 adaptation as well as (b) transmission modes 2 and 8 adaptation. Base station selects the specific transmission mode to meet the varying channel quality in the route. For the trial case (1), CDD is configured by the serving cell to support two data streams transmission. As the SINR and RSRP decrease, SFBC or beamforming is adopted to provide diversity gain. For the trial case (2), if the channel condition is qualified, transmission 8 is used to achieve both beamforming gain and multiplexing gain in case (2).

Table 2: Average throughput in the test route.

Transmission mode	2/3/7 adaptation	2/8 adaptation
Average throughput	9.87 Mbps	9.72 Mbps

In the mobility testing, the downlink throughput of TM2/3/7 adaptation and TM2/8 adaptation is almost the same. Mode adaptation is applied here to allow the base station to switch the transmission mode based on the channel condition. Since the poor coverage at the cell edge and the doppler frequency shift decrease the performance, the average throughput in the field trail is about 10 Mbps, which outperforms the third generation wireless system significantly [18, 19]. It is noted that the field trail route and the algorithm adopted in the base station and the UE may impact the performance; our test conclusion shows high reproducibility.

5. Conclusion

In this paper, we firstly give a brief introduction of different transmission modes, especially focusing on the those utilized in the TD-LTE network. Link level simulation is carried out to evaluate average downlink throughput. Then, indoor experiments are applied by employing the channel emulator. Two channel models, that is, SCME and IMT-A, are adopted in both simulations and indoor tests. In order to verify the performance enhancement of MIMO architectures in a live TD-LTE network, field trials are conducted in Huairou district, Beijing, China, which is a typical urban macroscenario containing ten sectors in the whole area. Stationary testing and mobility testing are included in the field trials. Downlink throughput for each transmission mode is obtained in the fixed location according to the UE received SINR. Furthermore, a drive route is carefully designed to go across the whole TD-LTE coverage area. Two MIMO adaptation schemes are analyzed and compared in the mobility testing. Because the vehicle type and the traffic in the street may impact the experiment results, we take two hours to obtain the average throughput. It is shown from the experiment results that TD-LTE system can provide similar performance compared with FDD-LTE and outperforms the third generation wireless networks significantly.

Acknowledgments

This work was supported by the State Major Science and Technology Special Projects (Grant no. 2010ZX03002-006) and NSFC Project (Grant no. 61201149).

References

[1] The 3rd Generation Partnership Project(3GPP) TS 36.211, "Technical specification group radio access network, evolved universal terrestrial radio access(E-UTRA); physical channels and modulation," March 2011, ftp://ftp.3gpp.org/Specs/.

[2] The 3rd Generation Partnership Project (3GPP) TS 36.212, "Technical specification group radio access network, mltiplexing and channel coding," March 2011, ftp://ftp.3gpp.org/Specs/.

[3] The 3rd Generation Partnership Project(3GPP) TS 36.213, "Technical specification group radio access network, physical layer procedures," March 2011, ftp://ftp.3gpp.org/Specs/.

[4] Evolution to LTE report, "GSM/3G market/technology update," November 2012, http://www.gsacom.com/.

[5] M. Peng, W. Wang, and H. Chen, "TD-SCDMA evolution," *IEEE Transactions on Vehicular Technology*, vol. 5, no. 2, pp. 28–41, 2010.

[6] M. Peng and W. Wang, "Technologies and standards for TD-SCDMA evolutions to IMT-advanced," *IEEE Communications Magazine*, vol. 47, no. 12, pp. 50–58, 2009.

[7] M. Peng and W. Wang, "A framework for investigating radio resource management algorithms in TD-SCDMA systems," *IEEE Communications Magazine*, vol. 43, no. 6, pp. S12–S18, 2005.

[8] B. Hagerman, K. Werner, and J. Yang, "MIMO performance at 700 MHz field trials of LTE with handheld UE," in *Proceedings of the IEEE Vehicular Technology Conference (VTC '11)*, pp. 1–5, September 2011.

[9] K. Werner, J. Furuskog, M. Riback, and B. Hagerman, "Antenna configurations for 4×4 MIMO in LTE—field measurements," in *Proceedings of the IEEE Vehicular Technology Conference (VTC '10)*, pp. 1–5, May 2010.

[10] S. Yasukawa, T. Kawamura, Y. Kishiyama, H. Taoka, and H. Andoh, "Field experiments on closed-loop SU-MIMO transmission considering effect of antenna configurations in LTE-advanced uplink," in *Proceedings of the IEEE Vehicular Technology Conference (VTC '12)*, pp. 1–5, May 2012.

[11] N. Miyazaki, S. Nanba, and S. Konishi, "MIMO-OFDM throughput performances on MIMO antenna configurations using LTE-based testbed with 100 MHz bandwidth," in *Proceedings of the IEEE 72nd Vehicular Technology Conference (VTC '10)*, pp. 1–5, September 2010.

[12] ITU-R M.2135, "Guidelines for evaluation of radio interface technologies for IMT-Advanced," November 2008.

[13] The 3rd Generation Partnership Project(3GPP) TS 25. 996, "Spatial channel model for multiple input multiple output (MIMO) simulations," September 2012, ftp://ftp.3gpp.org/Specs/.

[14] M. Narandzic, C. Schneider, R. Thoma, T. Jamsa, P. Kyosti, and X. Zhao, "Comparison of SCM, SCME, and WINNER Channel Models," in *Proceedings of the IEEE Vehicular Technology Conference (VTC '05)*, pp. 413–4417, June 2005.

[15] The 3rd Generation Partnership Project(3GPP) TSG-RAN WG1 meeting 44bis R1-061001, "LTE channel models and link simulations," March 2006, http://www.3gpp.org/ftp/tsg_ran/WG1_RL1/TSGR1_44bis/Docs/.

[16] M. Peng, X. Zhang, W. Wang, and H. Chen, "Performance of dual-polarized MIMO for TD-HSPA evolution systems," *IEEE Systems Journal*, vol. 5, no. 3, pp. 406–416, 2011.

[17] K. Nishimori, Y. Makise, M. Ida, R. Kudo, and K. Tsunekawa, "Channel capacity measurement of 8 × 2 MIMO transmission by antenna configurations in an actual cellular environment," *IEEE Transactions on Antennas and Propagation*, vol. 54, no. 11, pp. 3285–3291, 2006.

[18] X. Zhang, W. Wang, Y. Li, M. Peng, and S. Chen, "Performance analysis for dual polarization antenna schemes in TD-HSPA+system," in *Proceedings of the IEEE 21st International Symposium on Personal Indoor and Mobile Radio Communications (PIMRC '13)*, pp. 2052–2056, September 2010.

[19] M. Peng, H. Liu, W. Wang, and H. Chen, "Cooperative network coding with MIMO transmission in wireless decodeand- forward relay networks," *IEEE Transactions on Vehicular Technology*, vol. 59, no. 7, pp. 3577–3588, 2010.